STUDIES OF SURFACE PLSMONS AND

LOCALIZED SURFACE PLASMONS AT

TERAHERTZ FREQUENCIES

By

XINCHAO LU

Bachelor of Science in Optoelectronics
Tianjin University
Tianjin, China
2000

Master of Science in Physical electronics
Tianjin University
Tianjin, China
2003

Submitted to the Faculty of the
Graduate College of the
Oklahoma State University
in partial fulfillment of
the requirements for
the Degree of
DOCTOR OF PHILOSOPHY
December, 2009

STUDIES OF SURFACE PLSMONS AND

LOCALIZED SURFACE PLASMONS AT

TERAHERTZ FREQUENCIES

Dissertation Approved:

Dr. Weili Zhang
_____
Dissertation Adviser
Dr. Daniel Grischkowsky
_____

Dr. Alan Cheville
_____

Dr. Albert T. Rosenberger
_____

Dr. A. Gordon Emslie
_____
Dean of the Graduate College

ACKNOWLEDGMENTS

First of all, I would like to express my sincere appreciation to my advisor, Dr. Weili Zhang, who has supported me throughout my research with his patience, encouragement and knowledge. Dr. Zhang allowed me to be a part of the THz group at Oklahoma State University and instructed me toward becoming a scientifically precise investigator. Words are not adequate to express my gratitude for his guidance.

It is also my pleasure to thank Dr. Daniel Grischkowsky for continuously supporting and encouraging me. Our frequent discussions resulted in my receiving valuable advice. My appreciation is extended to Dr. Alan Cheville, Dr. Xincheng Xie, and Dr. Albert T. Rosenberger for serving on my advisory committee---for their time, patience and suggestions. I also would like to thank Dr. Aihua Xie and Dr. James West for sharing their scientific knowledge.

I would like to express my gratitude to Dr. Shuang Zhang. His beneficial teaching, assistance, and suggestions on my numerical simulations have extensively improved my research and my dissertation.

Very special thanks to Dr. Mufei Gong who has helped me from the day I entered the THz group, not only with academic research, but with daily activities. I am indebted to

TABLE OF CONTENTS

LIST OF FIGURES

Figure   Page

LIST OF TABLES

LIST OF SYMBOLS

λ	Subwavelength in free space
n	Conduction electron density
e	Elementary charge
m	Electron mass
ε_0	Dielectric constant of vacuum
ω_p	Plasma frequency
ω	Angular frequency, rad/s
γ	Collision frequency
τ	Average collision time of free electrons
ε_m	Complex dielectric constant of metal
ε_R, ε_{mR}	Real dielectric constant of metal
ε_I, ε_{mI}	Imaginary dielectric constant of metal
n_R	Real refractive index of metal
n_I	Imaginary refractive index of metal
ε_d	Dielectric constant of a dielectric medium
σ_s	Surface charge density
μ_0	Permeability of vacuum
μ_d	Permeability of dielectric medium
μ_m	Permeability of metal
δ	Skin depth
L_x	Propagation length
$\mathbf{H}$	Magnetic field
$\mathbf{E}$	Electric field
E_x	Electric field amplitude in x-direction
E_z	Electric field amplitude in z-direction
H_y	Magnetic field amplitude in y-direction
k_x	Wavevector along x-direction
k_z	Wavevector along z-direction
k_{SP}	Wavevector of surface plasmons
m, n	Order of mode
G_x, G_y	Lattice vector

f_{SP}	Resonance frequency of surface plasmons
P	Grating periodicity
c	Velocity of light in free space, 3×10^3 m/s
L	Particle size
x	Size parameter
I_{sca}	Intensity of light scattering
$t(\omega)$	Frequency-dependent amplitude transmission
$T(\omega)$	Frequency-dependent absolute transmittance
$\phi(\omega)$	Frequency-dependent phase change
E_{out}	Amplitude of THz pulse through sample
E_{in}	Amplitude of THz pulse through reference
q	Breit-Wigner-Fano coupling coefficient
Γ	Linewidth
$\hat{H}$	Hamiltonian
$\hat{V}$	Coupling term
κ	Coupling coefficient
θ	Incidence angle
TE	Transverse electric
TM	Transverse magnetic
$r(\omega)$	Frequency-dependent amplitude reflection
$R(\omega)$	Frequency-dependent absolute reflectance
Φ	Diameter of circular structure

CHAPTER I

INTRODUCTION

It is well known that light is not easy to "squeeze" through a single hole with dimension smaller than the wavelength. The transmission efficiency of such experiment predicted by Bethe is as low as $(r/\lambda)^4$, where r is the hole radius, λ is the incident wavelength [1]. For a subwavelength hole array made from metal, however, extraordinary transmission of orders of magnitude higher than the Bethe prediction was reported by Ebbesen et al. in 1998 [2]. It has been very interesting to explore what was happening to the transmission when light pass through the array of subwavelength holes that result in such a large discrepancy in transmission. Researchers have attributed such enhanced transmission to the presence of a collection of electrons oscillating along the metal surface, known as surface plasmons (SPs). Enhanced transmission through subwavelength holes promises a wide range of applications in many important areas, such as biological sensors, near-field microscopy, subwavelength photolithography, solar cells, and information display devices [3-7].

Another type of fundamental excitation of plasmons is localized surface plasmons (LSPs). Being associated with charge density oscillations contained around metallic

nanoparticles and resulted in strong light scattering and enhancement of the local electromagnetic field, LSPs have also attracted extensive attention recently. Although this effect has been applied in the staining of glass for many hundreds of years, a number of novel applications, such as optical sensing and enhanced Raman Scattering is under development based on the same principle [8,9].

Compared to numerous experimental and theoretical studies at visible frequencies, little work on SPs, especially LSPs with subwavelength micro-particles, has been carried out in the terahertz regime [10-14]. This dissertation focuses on the properties of SPs and LSPs resonating at terahertz frequencies. Such plasmonic resonances would have potential impacts on terahertz imaging, terahertz sensing, terahertz near field microscopy, and terahertz photonic devices [15,16].

1.1 Introduction: Surface Plasmons

Plasmon is a collection of electrons that collectively oscillate in a piece of conducting material. When electrons are displaced, the positive charge exerts an attractive force on the electrons and tries to pull them back to their original positions. Such Coulomb interactions make the plasmons oscillate once they are excited [17]. The oscillation frequency of collective electrons in a volume metal is called plasma frequency, $\omega_p = \sqrt{\dfrac{ne^2}{\varepsilon_0 m}}$, where n is conduction electron density, e is elementary charge, m is electron mass [17]. Compared to volume plasmons, which oscillate through the metal volume, SPs are confined to surface and interact strongly with light, resulting in

polaritons, also called SP polaritons. Since Ritchie demonstrated theoretically the existence of SPs at a metal surface in 1957 [18], it began to be widely recognized.

1.1.1 Drude model

SPs can be excited only along the interface between a dielectric and a metal, which is correlated to the response of metal interacting with the incident electromagnetic wave. Over a wide frequency range, the dielectric properties of metal can be depicted by Drude model, which assumes metal as free electron gas [17],

$$\varepsilon(\omega) = 1 - \frac{\omega_p^2}{\omega^2 + i\omega\gamma}. \tag{1-1}$$

Typical plasma frequencies, ω_p are comparable to the frequencies of visible light (i.e., $\sim$ 10^{15} - 10^{16} Hz). In the Drude model, interactions between electrons are not taken into account. The electrons oscillating in response to applied electromagnetic field are damped via collisions with nucleus at a collision frequency $\gamma = 1/\tau$, τ is known as the average collision time of free electrons. At room temperature, the typical value of τ is on the order of 10^{-14} s, corresponding to $\gamma \sim 10^{14}$ Hz. The real and imaginary parts of $\varepsilon(\omega)$ can be expressed as [17]

$$\varepsilon_R = 1 - \omega_p^2 \big/ \left(\omega^2 + \gamma^2\right),$$

$$\varepsilon_I = \omega_p^2 \gamma \big/ \left[\omega\left(\omega^2 + \gamma^2\right)\right]. \tag{1-2}$$

3

We will limit our discussion to frequencies $\omega < \omega_p$, where metals retain their metallic characteristics. For high frequencies $\omega >> \gamma$, which correspond to optical frequencies, damping can be ignored, ε_R can be approximated as $1 - \omega_p^2 / \omega^2$. Consequently, ε_R is negative and $\varepsilon_I \approx \gamma \omega_p^2 / \omega^3 << |\varepsilon_R|$. For low frequencies $\omega << \gamma$, such as in the terahertz regime, ε_R is still negative, whereas, $\varepsilon_I >> |\varepsilon_R|$.

The complex refractive index of metal can be defined as $n = \sqrt{\varepsilon} = n_R + in_I$ [17], where

$$n_R = \left[\frac{1}{2} \left(\sqrt{\varepsilon_R^2 + \varepsilon_I^2} + \varepsilon_R \right) \right]^{1/2},$$

$$n_I = \left[\frac{1}{2} \left(\sqrt{\varepsilon_R^2 + \varepsilon_I^2} - \varepsilon_R \right) \right]^{1/2}.$$

(1-3)

For $\omega < \omega_p$, n_I is larger than n_R, the propagation of electromagnetic wave in metal is dominated by absorption, leading to rapidly exponential decay of electric field that could not penetrate through the metal. The distance through which the amplitude of a electromagnetic wave decreases by a factor e^{-1} is defined as skin depth δ, which is changed according to the frequency of applied electromagnetic waves.

1.1.2 Dispersion relation of SPs on smooth metal surface

The simple geometry (shown in Figure 1-1) that sustains SPs is a single, flat interface in xy-plane between two half-infinite spaces 1 and 2, which are composed of a dielectric, non-absorbing half space ($z > 0$) with positive real dielectric constant ε_d and an adjacent

conducting half space ($z < 0$) described via a dielectric function $\varepsilon_m(\omega)$, which can be depicted by the Drude model [19]. The magnetic response is ignored and taken as $\mu_d = \mu_m = \mu_0$. When an electromagnetic wave incidents from the dielectric space to the metal space, the electric field with a component normal to the interface is the primary condition of SP excitation, which induces surface charge density σ_s along interface as $\sigma_s \propto (\varepsilon_d E_{1z} - \varepsilon_m E_{2z})$. As a result, SPs have p-wave-like characteristics on the flat interface and only TM polarized wave can excite it, no surface modes exist for the TE polarization.
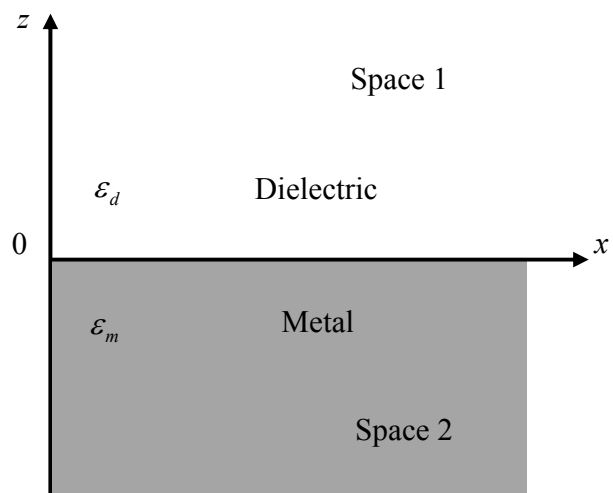
Figure 1-1 Schematic of SPs propagating at a single interface between a metal and a
dielectric.

Considering a TM wave incident from dielectric space to metal space, the fields in two media have the following expressions [19]:

For the dielectric medium where $(z > 0)$,

$$\vec{H}_1 = (0, H_{y1}, 0)e^{ik_{z1}z}e^{i(k_x x - \omega t)},$$

$$\vec{E}_1 = (E_{x1}, 0, E_{z1})e^{ik_{z1}z}e^{i(k_x x - \omega t)}. \tag{1-4}$$

For the metal medium where $(z < 0)$,

$$\vec{H}_2 = (0, H_{y2}, 0)e^{ik_{z2}z}e^{i(k_x x - \omega t)},$$

$$\vec{E}_2 = (E_{x2}, 0, E_{z2})e^{ik_{z2}z}e^{i(k_x x - \omega t)}. \tag{1-5}$$

Fulfill the fields to Maxwell's equations

$$\nabla \times \vec{H} = \frac{\varepsilon}{c} \frac{\partial}{\partial t}\vec{E},$$

$$\nabla \times \vec{E} = -\frac{1}{c} \frac{\partial}{\partial t}\vec{H},$$

$$\nabla \cdot \varepsilon \vec{E} = 0, \tag{1-6}$$

$$\nabla \cdot \vec{H} = 0.$$

Together with the continuity relations

$$E_{x1} = E_{x2},$$

$$H_{y1} = H_{y2},$$

$$\varepsilon_d E_{z1} = \varepsilon_m E_{z2}, \tag{1-7}$$

$$k_{x1} = k_{x2} = k_x.$$

the dispersion relation of SPs in the system can be obtained:

$$\frac{k_{z1}}{\varepsilon_d} + \frac{k_{z2}}{\varepsilon_m} = 0. \tag{1-8}$$

This expression indicates that SPs can only be excited at the two-media-composed interface of opposite signs in dielectric constant.

Finally, the total wavenumber of SPs in the two media can be shown as:

$$k_x = \frac{\omega}{c}[\varepsilon_d\varepsilon_m/(\varepsilon_d + \varepsilon_m)]^{1/2},$$

$$k_{z1} = \frac{\omega}{c}[\varepsilon_d{}^2/(\varepsilon_d + \varepsilon_m)]^{1/2}, \tag{1-9}$$

$$k_{z2} = \frac{\omega}{c}[\varepsilon_m{}^2/(\varepsilon_d + \varepsilon_m)]^{1/2}.$$

The properties of SPs with electric field propagating along x direction (parallel to the surface) and decaying along z direction (perpendicular to the surface) determine the complex value of k_x, as well as the purely imaginary values of k_{z1} and k_{z2}. As a result, the condition of $\varepsilon_d > 0$, $\varepsilon_m < 0$, and $\varepsilon_d < |\varepsilon_m|$ should be satisfied for SPP propagating. Also, the wavenumber of SPs indicates that SPs possess both transverse and longitudinal electromagnetic field waves components.

Figure 1-2 shows the dispersion relation of SPs along the interface between the dielectric medium ε_d and metal ε_m [19]. As $\omega < \omega_p/\sqrt{1 + \varepsilon_d}$, the propagation of SPs bound to the

surface, corresponding to non-radiative evanescent surface waves. As $\omega > \omega_p$, both k_x

and k_z transform to real values, with SPs radiate out of surface, which is called radiative

SPs.
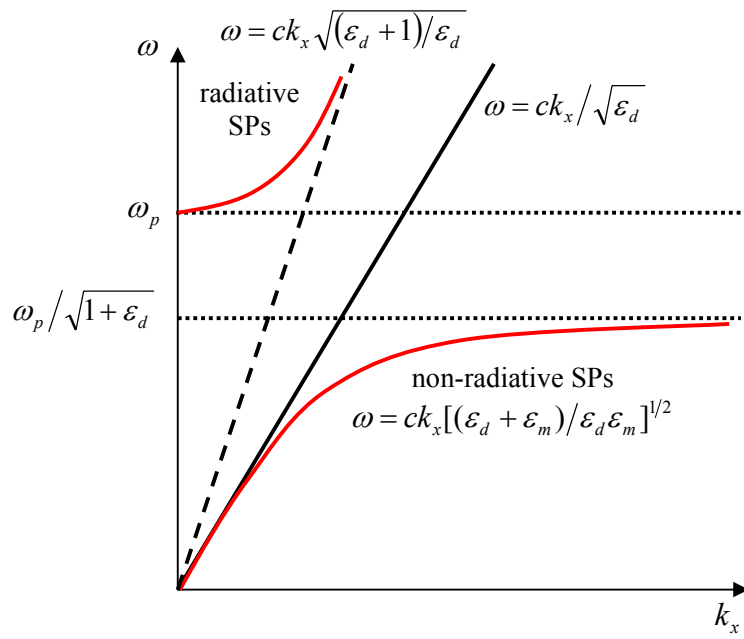
Figure 1-2 Dispersion relation of SPs at interface between the dielectric ε_d and metal

ε_m [19].

1.1.3 Propagation length and skin-depth of SPs on smooth surface

Since the dielectric constant of metal is complex, $\varepsilon_m = \varepsilon_{mR} + i\varepsilon_{mI}$, k_x is also complex, i.e. $k_x = k_{xR} + ik_{xI}$. As a consequence, SPs propagating along a dielectric/metal interface exhibit a finite propagation length, L_x, given by [19]

$$L_x = 1\Big/ 2k_{xI} = \frac{c}{\omega}\left(\frac{\varepsilon_{mR} + \varepsilon_d}{\varepsilon_{mR}\varepsilon_d}\right)^{\frac{2}{3}}\frac{\varepsilon_{mR}^2}{\varepsilon_{mI}}. \qquad (1\text{-}10)$$

Also, as k_z is purely imaginary, the depths of SPs penetrate into dielectric δ_1 and metal δ_2 can be expressed respectively as [19]:

$$\delta_1 = \frac{1}{k_{z1}} = \frac{c}{\omega}\left(\frac{\varepsilon_d + \varepsilon_{mR}}{\varepsilon_d^2}\right)^{\frac{1}{2}},$$

$$\qquad (1\text{-}11)$$

$$\delta_2 = \frac{1}{k_{z2}} = \frac{c}{\omega}\left(\frac{\varepsilon_d + \varepsilon_{mR}}{\varepsilon_{mR}^2}\right)^{\frac{1}{2}}.$$

In the terahertz regime, $\varepsilon_m \gg \varepsilon_d$, and $\varepsilon_{mI} \gg |\varepsilon_{mR}|$, propagation length $L_{x\,THz}$ and skin depth δ_{THz} of SPs can be approximated as [33]:

$$L_{x\,THz} = \frac{c}{\omega}\frac{\varepsilon_{mI}}{\varepsilon_d^{3/2}},$$

$$\delta_{1\,THz} = \frac{c}{\omega}\left(\frac{\sqrt{2\varepsilon_{mI}}}{\varepsilon_d}\right), \qquad (1\text{-}12)$$

$$\delta_{2\,THz} = \frac{c}{\omega}\left(\sqrt{\frac{2}{\varepsilon_{mI}}}\right).$$

Both the propagation length and skin depth show a strong dependence on frequency. As shown in Figure 1-3, in the visible regime, SPs exhibit large field confinement to the interface and a subsequent small propagation length due to increased damping. In the terahertz regime, however, SPs fields extend more into dielectric space, which reveals small localization and larger propagation length. In the terahertz and microwave regimes, SPP waves, which distribute to the surface loosely, are also known as Zenneck waves [20]. At 0.54 THz, the skin depths of SPs in the air and silicon are 0.14 and 0.012 m, respectively, while, the skin depth of SPs in the Aluminum is 110 nm.
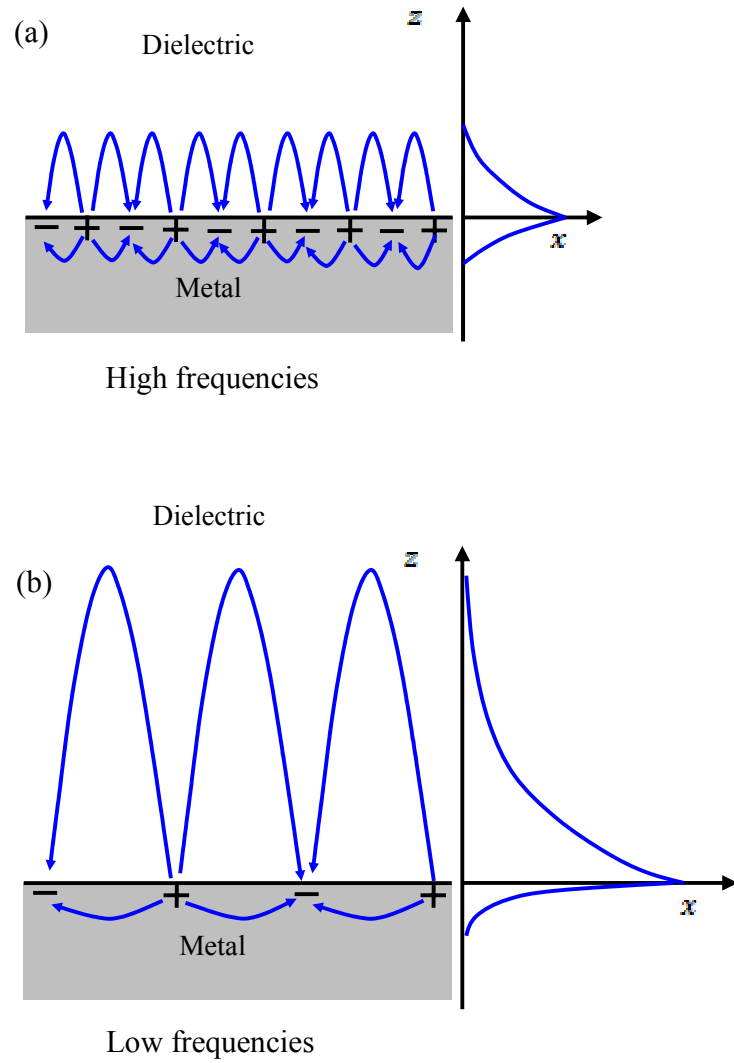
Figure 1-3 Schematic diagram of SPs propagating on a surface defined by *x-y* plane at *z* = 0 along *x* direction at (a) high and (b) low frequencies. Exponentially decayed field E_z as a function of *z* shown in *x-z* coordinate for both low and high frequencies, where $z > 0$ is inside dielectric and $z < 0$ is inside metal.

1.1.4 Resonant excitation of SPs

As seen from the dispersive relation of SPs shown in Figure 1-2, the wave vector of the SP mode is always sitting on the right of the wave vector of incident electromagnetic waves. This indicates that with the same frequency, the momentum of the SP mode is always greater than that of the incident electromagnetic waves. With a mismatch momentum, there are no SPs can be excited when electromagnetic wave is incident from dielectric to a smooth metal surface. Therefore, several experimental approaches have been developed to provide the necessary wave vector conservation, including attenuated total internal reflection (ATIR) prisms, gratings, and waveguides. Here, we focus on the coupling method by use of periodic array of subwavelength holes.

Subwavelength metallic hole array is a unique way to tailor the wave vector mismatch between the incident photon and SPs by introducing a two-dimensional lattice wave vector, as shown in Figure 1-4. The compensated wave vector can be expressed as [22]:

$$k_{SP} = \frac{\omega}{c}\sqrt{\varepsilon_0}\sin\theta \pm mG_x \pm nG_y,$$ (1-13)

where θ is incident angle, m, n are integers, and G_x and G_y are the lattice vector. For a hole array of square lattice, $G_x = G_y = 2\pi/P$, where P is two-dimensional periodicity. When the electromagnetic waves impinge on the metallic hole array, SPs can be excited along the air/metal interface, tunnel through the subwavelength holes, couple with direct transmission of incident photons, and propagate along the exit side (substrate/metal interface), subsequently. Afterwards, the freely propagating photons will be reemitted by reverse process of SP excitation at the substrate/metal interface with enhanced

transmission. The microscopic theory of the enhanced transmission is explained in Ref. [21]. As subwavelength holes can accumulate electrons and generate surface charge density oscillations to introduce longitudinal electron wave of SPs, both TM and TE-polarization wave can excite SPs by using the subwavelength metallic hole array [22].
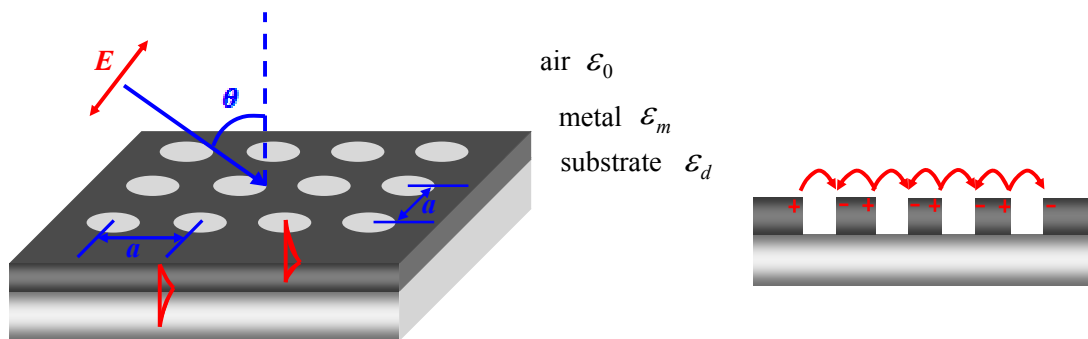
Figure 1-4 Schematic of SP coupling by two-dimensional hole array

air ε_0

metal ε_m

substrate ε_d

By Combining Equation 1-9 with Equation 1-13, resonant frequency of SPs with normal incident at air/metal interface (input side) can be approximately by [17]:

$$f_{SP\,air-metal} = \frac{c\sqrt{m^2 + n^2}}{P}\sqrt{\frac{\varepsilon_0 + \varepsilon_m}{\varepsilon_0 \varepsilon_m}}. \qquad (1\text{-}14)$$

Also, SP resonance frequency at the substrate/metal interface (output side) can be obtained as:

$$f_{SP\,substrate-metal} = \frac{c\sqrt{m^2 + n^2}}{P}\sqrt{\frac{\varepsilon_d + \varepsilon_m}{\varepsilon_d \varepsilon_m}}. \qquad (1\text{-}15)$$

As $|\varepsilon_m| \gg \varepsilon_0$ and ε_d in the terahertz regime, resonance frequencies reside in the input and exit sides can be approximate as [17]:

$$f_{SP\,air-metal} = \frac{c\sqrt{m^2 + n^2}}{P\sqrt{\varepsilon_0}}, \qquad (1\text{-}16)$$

and

$$f_{SP\,air-metal} = \frac{c\sqrt{m^2 + n^2}}{P\sqrt{\varepsilon_d}}. \qquad (1\text{-}17)$$

It is well known that in the low-frequency domain, i.e. terahertz and microwave regimes, localization of surface waves bound to flat interface breaks down. The transverse component is dominant in the electric field of SPs at low frequencies due to significance decrease of k_{SP}, which is almost equal to the wave vector of incident photons. As a result, SPs vanish in the limit of prefect electrical conductor. However, subwavelength metallic hole array will introduce artificial plasmons, i.e. spoof plasmons, along the interface, resulting in better confinement of surface waves in the terahertz regime [23].

Such design could have a number of applications in highly sensitive biological sensing and near-field imaging using terahertz waves.

1.2 Introduction: localized surface plasmons

In addition to the propagating SPs at the metal-dielectric interface, the geometries on the metal film, such as particles or holes, will involve the LSPs, which are confined to the boundary of the metal structures of subwavelength dimensions. LSPs, also called shape resonance, are non-propagating excitations and characterized by discrete, complex frequencies depending on the size and the shape of the objects and the dielectric constant of the constituent materials. Different from the propagating SPs, LSPs only possess longitudinal component. The transverse component, however, vanishes due to localization of the electrons around the edge of particles.

1.2.1 Localized surface plasmons of metallic particles

For subwavelength metallic particles, the incident electromagnetic waves induce the conduction electrons to oscillate coherently when the electrons resonant with the frequency of incident wave, which is equivalent to a dipole resonance [41]. As a result, LSPs induced by the metallic particles are also named as Dipole localized surface plasmons (DLSPs).

When incident electromagnetic waves interact with subwavelength metallic particles, conduction electrons absorb energy from the incident wave to oscillate and transfer to radiative photons subsequently. Therefore, the resonance of metallic particles can be

characterized by scattering properties. The analyses of particle scattering can be classified in terms of particle size L compared with incident wavelength λ, as denoted by a size parameter $x = 2\pi L/\lambda$, and dielectric properties of metallic particles ε_m, as shown in Figure 1-5(a) [24]. With a relatively small ε_m at optical frequencies, when the particle size is much smaller than the incident wavelength, i.e. $0 < x \ll 1$, the phase of the harmonically oscillating electromagnetic field is constant over the particle volume, and the interaction of a particle with the electromagnetic field can be analyzed using the quasi-static approximation. The scattering of particles can be approximated by Rayleigh scattering, in which the intensity of scattering is reversely proportional to incident wavelength, i. e. $I_{sca} \propto \lambda^{-4}$ [24]. When $x \sim 1$, the particle size is comparable with the incident wavelength, the special retardation effects that due to phase-changes of the driving field over the particle volume could not be neglected. Consequently, the Mie's scattering should be employed in such situation by accounting into the influence of particle size. In the terahertz regime, however, ε_m is so large that metal can be approximated as perfect conductor, leading to negligible influence of particle size to resonance. The incident electric field will not penetrate into the particle at all, and can be treated as totally reflecting particles as shown in Figure 1-5(b).
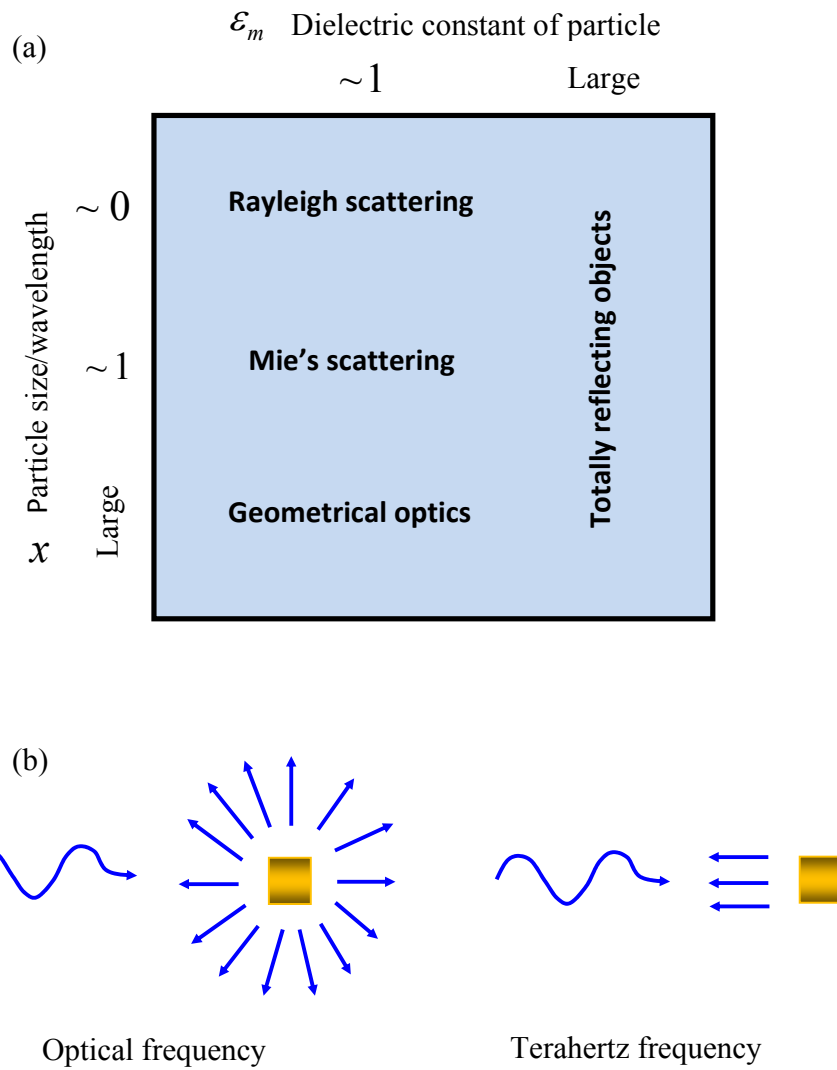
Figure 1-5 (a) Light scattering regimes [24]. (b) Light scattering at optical frequencies and total reflection in the terahertz regime in which edge effect is neglected.

When the particles are in an aggregation, the interactions between the particles could not be neglected and introduce an extra frequency-shift compared to the single particle resonance. The particle array in the terahertz regime is similar to the frequency selective surface at microwave frequencies, which introduces surface current for the resonance analysis.

The metallic particle arrays resonating at terahertz frequencies studied in the dissertation may be potentially used in the phased array receivers and transmitters. The phased arrays used in communications and military radars are group of radiating antennas each with a phase shifter. The effective radiation of the arrays is constructive in desired direction and suppressed in undesired directions [25]. The radiation of the phased array is also steered by varying the phase of each antenna for both transmission and detection.

1.2.2 Localized surface plasmons of metallic holes

When electromagnetic waves impinge on subwavelength holes, electrons accumulating around the edge of the holes enable excitation of LSPs. In order to distinguish the LSPs resulted from particles and holes, we named the particle LSPs as DLSPs, and those in holes as LSPs during the following Sections. Recently, theoretical and experimental studies show that LSPs, which is dependent on the dimensions and geometry of the holes, also contribute to the enhanced transmission through subwavelength metallic hole array in addition to SPs [26,27].

In order to exclude the effect of SPs excited in the periodic hole arrays, single hole and random hole array were used to study the transmission properties of LSPs [28,29]. In Figure 1-6(a), plane wave normally incidents to a single subwavelength rectangular hole with $E \parallel y$ (long axis) and $H \parallel x$ (short axis). Surface current I_s is induced along the surface of the metal. In the vicinity of the hole, I_s distorts the current distribution to avoid the hole. Also, the induced charges accumulated at the opposite of hole length along y axis. In Figure 1-6(b), the magnetic field above the hole, without the support of underlying surface current, drop into the hole on one side and raise from the other side. The hole can be regarded as an equivalent magnetic dipole that oscillate along x axis. Equivalent electric dipole of hole is shown in Figure 1-6(c), which is induced by the accumulated charges confining at the edges of the hole. As parallel component of electric field cannot exist on conducting surface, the E fields in the vicinity of the hole originate and terminate at the edge of the hole. In the far field of the hole, the E fields along z axis play an important role and can be regarded as equivalent electric dipole along z axis. With incident plane waves impinge to the hole, the incident magnetic field along x axis excites the magnetic dipole resonance. The electric dipole resonance, however, cannot be occurred due to the perpendicular incident electric field. As a result, the single subwavelength hole can be regarded as magnetic dipole resonance normal to the incident electric field direction [28,30].
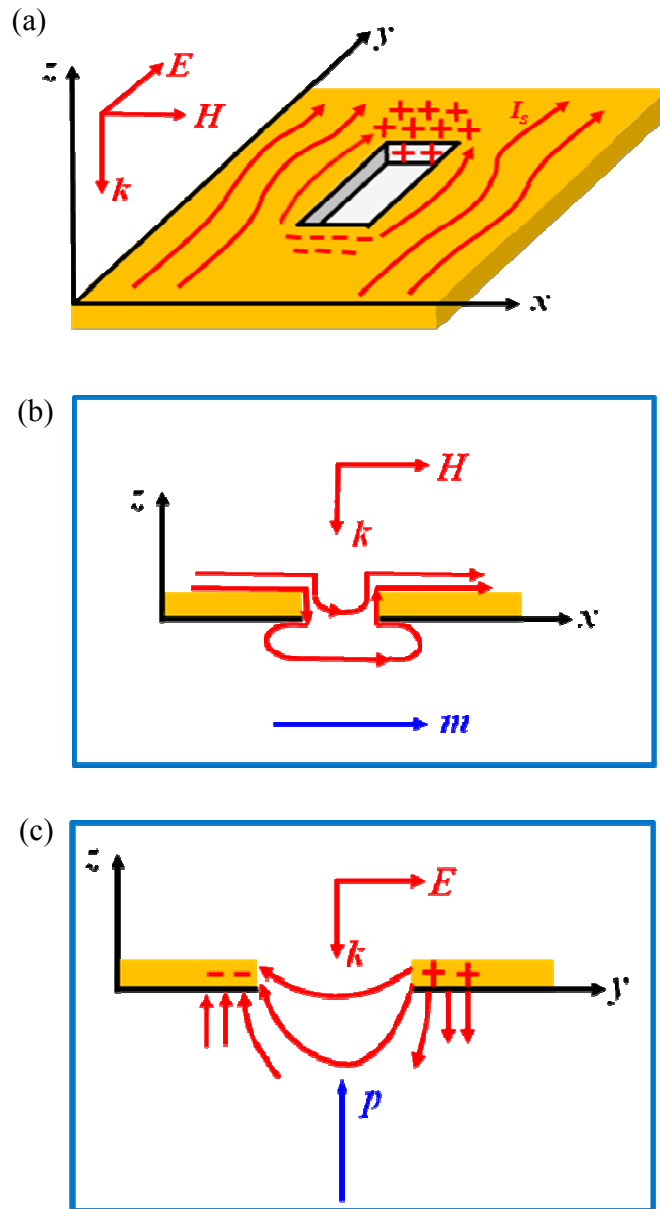
Figure 1-6 (a) Schematic of the surface current I_s and accumulated charges along edge of the hole induced by normally incident plane wave. (b) The equivalent magnetic dipole of the hole. (c) The equivalent electric dipole of the hole.

The transmission through the subwavelength hole is dependent on its dimension; the transmission can further decreased with an exponential dependence by larger hole depth. Such tunneling transmission would be increased and exhibit a transmission peak at the wavelength where LSPs is excited [30,31]. As for the periodic hole array, the excitation of SPs can provide an additional coupling between the LSPs of adjacent holes, leading to a spectral shift in the LSP response [32]. In the terahertz domain, as excitation of SPs is insignificant, LSPs induced around subwavelength holes can produce mimic SPs to approach the enhanced transmission. Compared to SPs and DLSPs discussed above, the characteristics of LSPs still need further investigation.

1.3 Dissertation Outline

The objective of this work is to explore the physical origin of extraordinary transmission through subwavelength metallic hole array, as well as the resonant properties of the complementary structure, subwavelength metallic particle array at terahertz frequencies. The outline of this report is as follows.

Chapter 1 generalized the introduction of SPs and LSPs.

Chapter 2 presents experimental demonstrations of extraordinary transmission through subwavelength random and periodic hole arrays. By varying the hole width and orientation, the coupling effect between LSPs and direct transmission is proven to induce the extraordinary transmission through the random hole array. The hole width, orientation, incident polarization, and angle-dependent transmission measurements of

periodic hole array indicate a more complicated coupling mechanism, involving SPs, LSP, and direct transmission. The Fano line shape fitting, coupling coefficient calculation, and electric field simulations provide a good fit to the experimental results.

Chapter 3 illuminates the resonance of subwavelength metallic particle arrays, the DLSPs in the terahertz regime. The measured frequency-dependent reflection/transmission by THz-TDS demonstrates various factors that influence the DLSP resonance, such as particle shape, surrounding substrate, and periodicity. Detailed study of resonance of ring and coaxial particle arrays, which deliver larger electromagnetic field enhancement, narrower linewidth, and improved tunability is carried out theoretically and experimentally to understand the physics origins.

Chapter 4 demonstrates the extraordinary transmission through subwavelength rectangular hole arrays, hybridized with either solid or ring particles, that possess a stronger enhanced transmission compared to the hole-only array conterpart. By changing the inner particle dimension, hole orientation and incident angle, the measured frequency-dependent transmission reveals that such strengthened resonance is characterized by the coupling between DLSPs, LSPs, and SPs. This is further confirmed by numerical analysis using the Fano model and electric field simulations.

Chapter 5 investigates the terahertz resonance through multilayer plasmonic crystals. Enhanced transmission can be obtained in multilayer complementary structures through

the out-plane coupling between DLSPs, LSPs, and SPs. Numerical simulation provides

further verification.

CHAPTER II

ENHANCED TERAHERTZ TRANSMISSION IN SUBWAVELENGTH HOLE
ARRAY

Recent studies have shown that the enhanced transmission in the array of subwavelength holes primarily introduced by SPs also related to the shape of the holes, as referred to as LSPs or shape resonance. How the coupling between LSPs and SPs leads to the enhanced transmission remains interesting for the plasmonics community. In this Chapter, the physical mechanism of the enhanced transmission through metallic subwavelength hole arrays is investigated in the terahertz regime. By varying the geometrical parameters, such as hole width and orientation, and the incident angle of terahertz radiation on to the random hole array, LSPs are demonstrated to clearly affect the enhanced transmission behaviors. Based on the results on LSPs of holes, enhanced transmission through periodic hole arrays is studied by changing the hole width, hole orientation, as well as the incident polarization and angle. The measured spectra are fit by the Fano model, and it manifests that the resonant properties of periodic hole arrays can be attributed to the a combined contribution of SPs, LSPs and the direct transmission of terahertz pulses. The coupling coefficient between these effects is calculated by using Hamiltonian Matrices.

2.1 Sample fabrication

All metallic subwavelength hole arrays are processed by conventional photolithography and thermal metallization on silicon substrate (0.64-mm-thick, *P*-type silicon, resistivity $\rho = 20\ \Omega$ cm) [33]. First, HMDS, a photoresist-adhesive primer, was spin-coated on the wafer at 3000 rpm for 30 seconds. Then a positive photoresist S-1813 from Shipley Inc. was spun with speed of 3000 rpm for another 30 seconds. The thickness of the photoresist layer at this speed was approximately 1.5 μm. After softbake in thermal oven at 115 °C for 15 minutes, the wafer was exposed with a contact mode mask aligner using the G line blue light for 30 seconds. The subsequent development for 30 seconds will leave a structured photoresist layer on the wafer. In the metallization process, a 190-nm-thick Allunimum film was thermal evaporated on the patterned photoresist using a thermal evaporator (BOC Edward 306) at vacuum pressure of 2.5×10^{-5} mB and a deposition rate of ~10 nm/s [33]. After the lift-off process in acetone, a pattern of rectangular metal hole array is formed on the silicon substrate. A microscopy image of the Al arrays are shown in Figure 2-1.
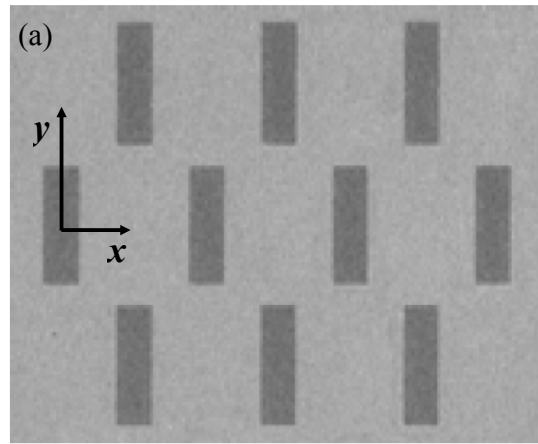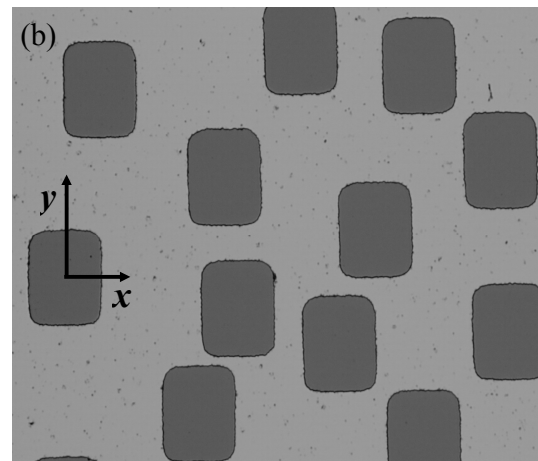
Figure 2-1 Microscopy images of (a) $120 \times 40~\mu m^2$ hole array with 160 μm period and (b) $125 \times 155~\mu m^2$ random hole array.

2.2 Experimental method

We employed a terahertz time-domain spectroscopy (THz-TDS) transmission system (shown in Figure 2-2) [33] to characterize the resonant properties of the metallic subwavelength hole arrays. The parabolic mirrors are arranged in a confocal geometry with a distance between the transmitter and receiver equal to twice of the summation of the focal length of all the parabolic mirrors. It therefore delivers excellent beam coupling between the transmitter and receiver modules. The Gaussian-type beam of the terahertz pulses is focused to a frequency-independent beam waist of 3.5 mm at the center between M_2 and M_3 mirrors, which are identical with a focal length of 50 mm. With femtosecond pulses of average power 10 mW and repetition rate 88 MHz incident onto both transmitter and receiver, the system is capable of generating terahertz radiation of 4.5 THz useful bandwidth. Such 8-F system thus enables spectroscopy characterization of samples with comparatively small dimension [33].
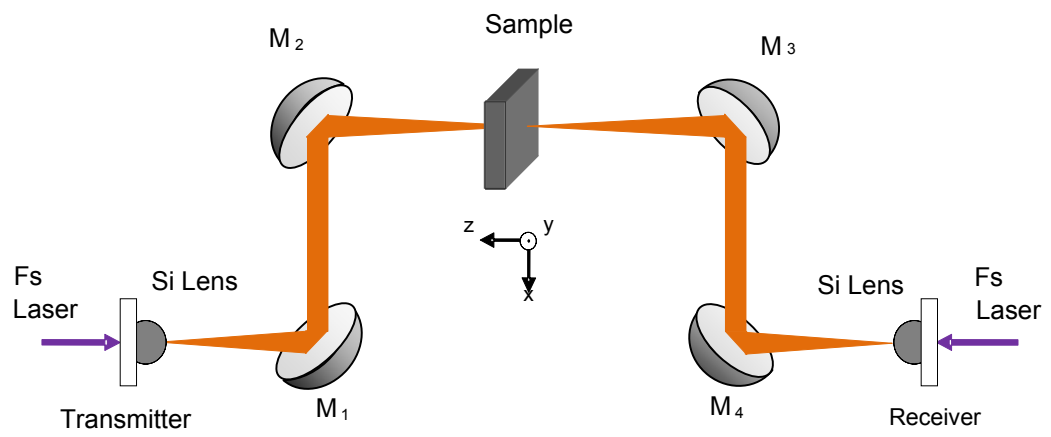
Figure 2-2 Experimental diagram of the 8-F THz-TDS setup [33].

2.3 Data acquisition

A blank silicon slab identical to the array substrate is used to obtain the reference terahertz pulses. The arrays are characterized by the broadband THz-TDS system depicted above, in which the sample is placed midway between the photoconductive transmitter and receiver (in the far field) [11,34]. The polarization of the terahertz electric field is parallel to the x axis shown in Figure 2-1. The absolute transmittance is defined as $T(\omega) = |t(\omega)|^2 = |E_{out} / E_{in}|^2$, where $|t(\omega)|$ is the amplitude transmission, $E_{out}(\omega)$ and $E_{in}(\omega)$ are the amplitudes of the terahertz pulses through the sample and reference, respectively. Figure 2-3(a) illustrates the measured transmitted terahertz pulses through the reference and an triangular lattice array with hole dimensions of $120 \times 40 \ \mu m^2$ and a periodicity of 160 μm. The extracted frequency-dependent amplitude transmission $|t(\omega)|$ and phase $\phi(\omega) = \arg(\widetilde{t}(\omega))$ are illustrated in Figure 2-3(b) [35].
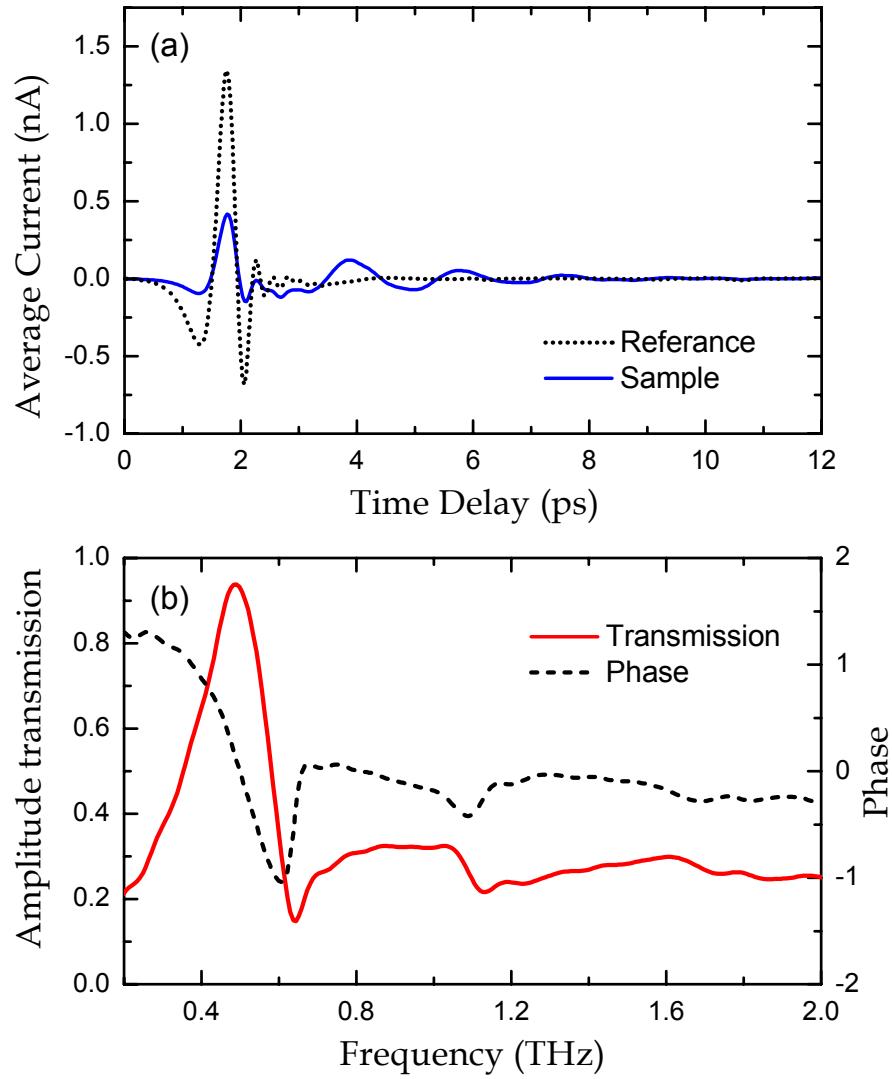
Figure 2-3 (a) Measured transmitted terahertz pulse through the reference and a 120×40 μm^2 hole array with periodicity 160 μm. (b) Corresponding frequency-dependent amplitude transmission and the phase change.

2.4 Enhanced transmission through random array of subwavelength holes

It is well known that the momentum introduced by periodicity in the hole array contributes substantially to the excitation of SPs [2]. If the holes were not organized in periodicity, however, the SPs may not be excited and only the LSPs exist [29]. In order to study the contribution of the LSPs, random hole arrays on the Si substrate are fabricated by conventional photolithography and metallization processes described in Section 2.1. A microscopy image of the random hole array is shown in Figure 2-1(b).

2.4.1 Dependence of transmission on hole width in random arrays

The characterized random hole array has the same filling factor as the periodic array of a 260 μm periodicity. The hole length is fixed as 155 μm and the width varies from 65 to 165 μm with a 20 μm interval. As shown in Figure 2-4(a), when terahertz radiation is normally incident onto the sample at $E \parallel x$, with increasing hole width, the amplitude transmission is enhanced from 0.38 to 0.57. This can be understood as the increase of the contributions of direct terahertz transmission with increasing hole areas. The normalized amplitude transmission to the area of the holes is shown in Figure 2-4(b). For resonance frequency located at 0.32 THz, however, no frequency shift is observed with increasing hole width along x axis. As mentioned in Section 1.2.2, LSPs of a single hole can be regarded as a magnetic dipole which resonates along the axis perpendicular to the E-field [30]. The resonance frequency of the single holes in all the random hole arrays is calculated to be 0.28 THz. As a result, varying the hole width only along the direction perpendicular to the E-field, which related to the LSP resonance, will modify the

resonance frequency. The discrepancy between experiment and calculated resonance frequency is caused by the interactions between LSPs and the incident waves, which will be discussed in Section 2.5.2. Also, the broadened linewidth can be observed from Figure 2-4(a), due to increased damping with increasing hole width.
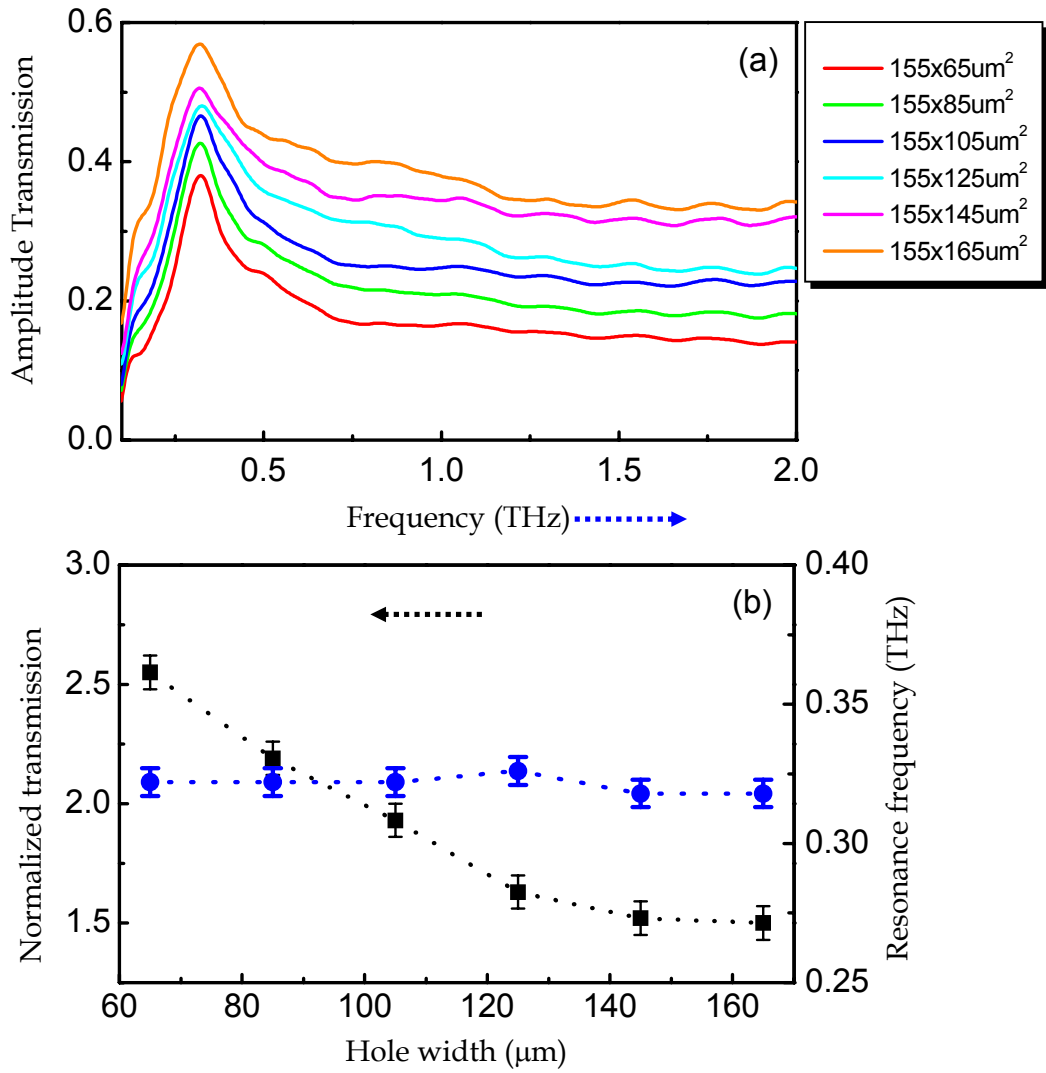
Figure 2-4 (a) Measured frequency dependent amplitude transmission of the random hole arrays with fixed hole length of 155 μm, various hole widths from 65 to 165 μm with an interval of 20 μm, and an effective periodicity 260 μm, $E \parallel x$. (b) Normalized peak transmission (black squares) and resonance frequency (blue circles) as a function of hole width. The dotted line is to guide the eye.

2.4.2 Dependence of transmission on hole orientation in random arrays

In Figure 2-5(a), by changing the hole orientation from $E \parallel x$ to $E \parallel y$, different resonant properties of the random hole array are revealed. When $E \parallel y$ with normal incidence, the hole width along x axis increased with an interval of 20 μm, which induces different level of magnetic dipole resonance along x axis that results in resonance frequency blue-shift. According to the duality principle, the magnetic dipole of hole along x axis is equivalent to the electric dipole of the complementary particle resonant at the same direction. The resonance frequencies of different hole widths along x axis are calculated by electric dipole resonance along x axis in Figure 2-5(b), which show agreement with the experiment. Also, the increased amplitude transmission with increasing hole width along x is observed in Figure 2-5(a). When the hole width along x is 65 μm, both LSPs resonance and direct transmission are too small to induce a obvious resonance. With increasing hole width along x, the coupling between LSPs and the direct transmission is strong enough to sustain a resonance.
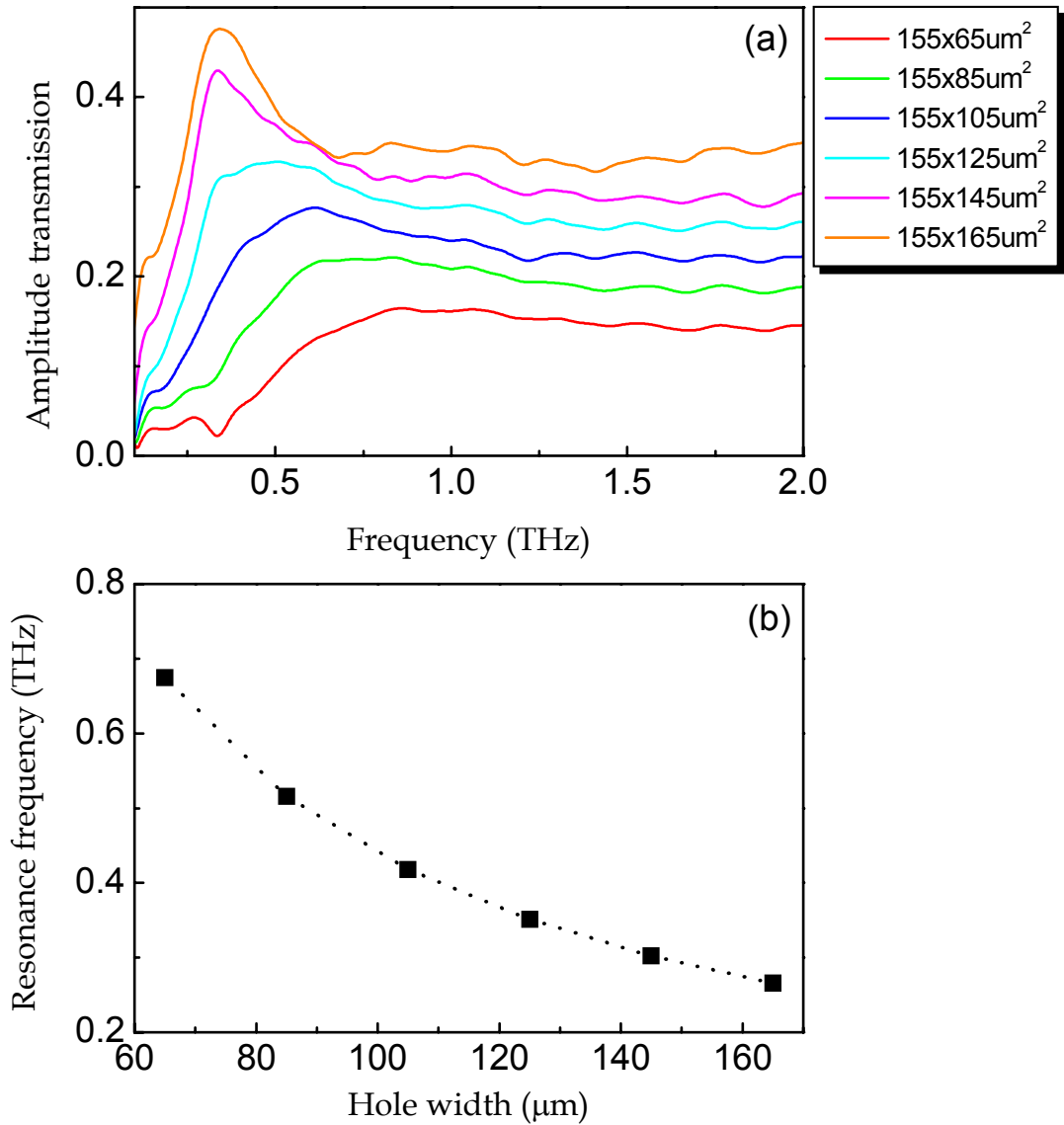
Figure 2-5 (a) Measured frequency dependent amplitude transmission of the random hole arrays with fixed hole length of 155 μm and various hole widths from 65 to 165 μm with an interval of 20 μm, an effective periodicity 260 μm, $E \parallel y$. (b) Calculated resonance frequency (black squares) as a function of hole width. The dotted line is to guide the eye.

2.4.3 Dependence of transmission on incident angle in random arrays

The effect of transmission of the random hole array on the incident angle of terahertz pulses is characterized. The effective periodicity of the random hole array is 260 μm, and the hole dimension is 155×125 μm². As shown in Figure 2-6, by changing the incident angle from 0º to 40º with interval of 10º, both the amplitude transmission and the resonance frequency, which is almost fixed at 0.355 THz has shown no obvious change. This indicates that the LSP resonance is independent of the incident angle, which is consistent with shape resonance.
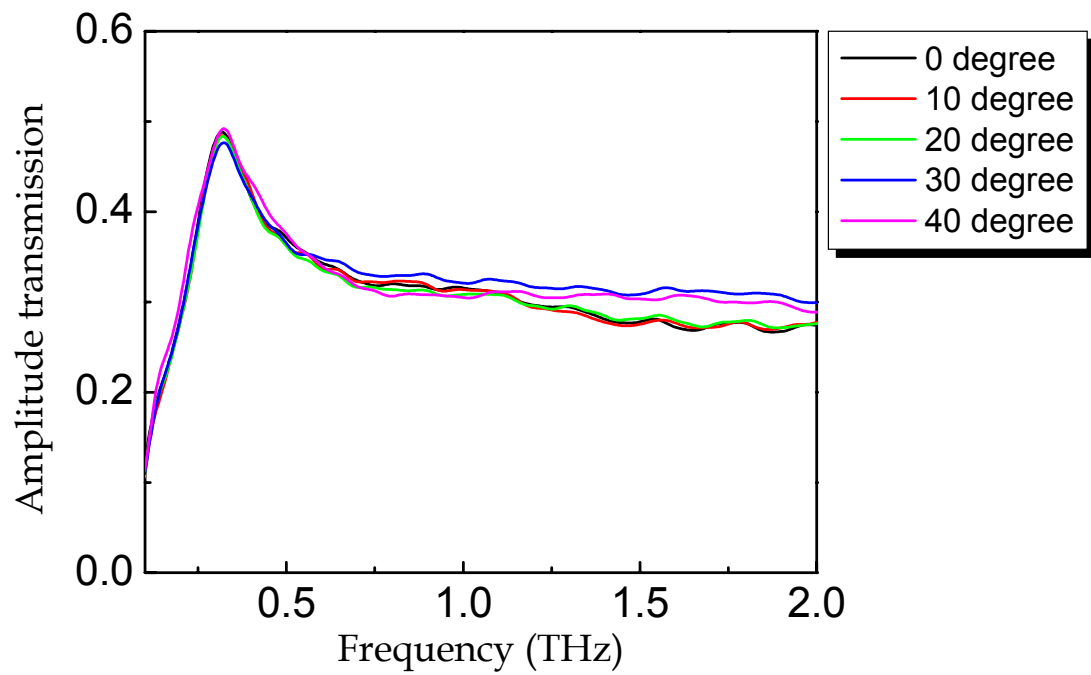
Figure 2-6 Angle-independent amplitude transmission of random hole array with hole dimension of 155×125 μm², and an effective periodicity of 260 μm, $E \parallel x$, TM-polarization.

2.5 Enhanced transmission through periodic subwavelength hole array

Based on the results of LSPs in the random hole array, enhanced transmission resulted from the SPs introduced by periodic hole array is studied. By changing the hole width, hole orientation, incident polarization, and incident angle of terahertz radiation to the hole array, properties of enhanced transmission due to coupling between resonance of SPs and LSPs are investigated. Also, by using Fano model and Hamiltonian Matrices, the coupling strength between SPs and LSPs is demonstrated.

2.5.1 Dependence of transmission on hole width of periodic arrays

The measured amplitude transmission of triangle lattice arrays with a fixed length 120 μm and various widths from 40 to 140 μm with a 20 μm interval, periodicity of 160 μm is shown in Figure 2-7 [13]. The transmission reveals an interesting characteristic evolution with increasing hole width. The amplitude transmission (squares) is enhanced with increasing hole width of up to 80 μm, however, the further increase in hole width beyond 80 μm gives rise to a monotonic decay in amplitude transmission, as depicted in Figure 2-8(a). At hole width of 40 μm, amplitude transmission has a value of 0.95, whereafter it is enhanced to ~1.0 at 80 μm, and then is reduced to 0.91 at 140 μm. This suggests that there exists an optimal hole width, at which amplitude transmission approaches a maximum value. When the amplitude transmission is normalized by the area of the holes to normalized amplitude transmission, as shown by the circles in Figure 2-8(a), normalized amplitude transmission exhibits monotonic decrease with increasing hole width. Meanwhile, the resonance frequency and the corresponding linewidth exhibit monotonic changes. As the hole width increases from 40 to 140 μm, the resonance

frequency is shifted from 0.49 to 0.62 THz, as shown in Figure 2-8(b), while the corresponding linewidth is broadened from 0.20 to 0.66 THz. As mentioned in Section 2.4.1, the LSP resonance of single hole will not change by increasing the hole width along x axis with $E \parallel x$. Also, the SP resonance will not alter as well because of the same periodicity of all hole arrays. What causes the frequency shift of periodic hole array with increasing the holes width? When the holes width increases, the coupling strength between the resonances of SPs and LSPs will decrease, which will be illustrated in Section 2.5.3, leading to the resonance frequency shift. Meanwhile, the competition between coupling of SPs and LSPs as well as direct transmission generates the maximum transmission value at 80 μm hole width. Although the contribution of direct transmission will decrease as the hole width enlarges, the normalized amplitude transmission will diminish.
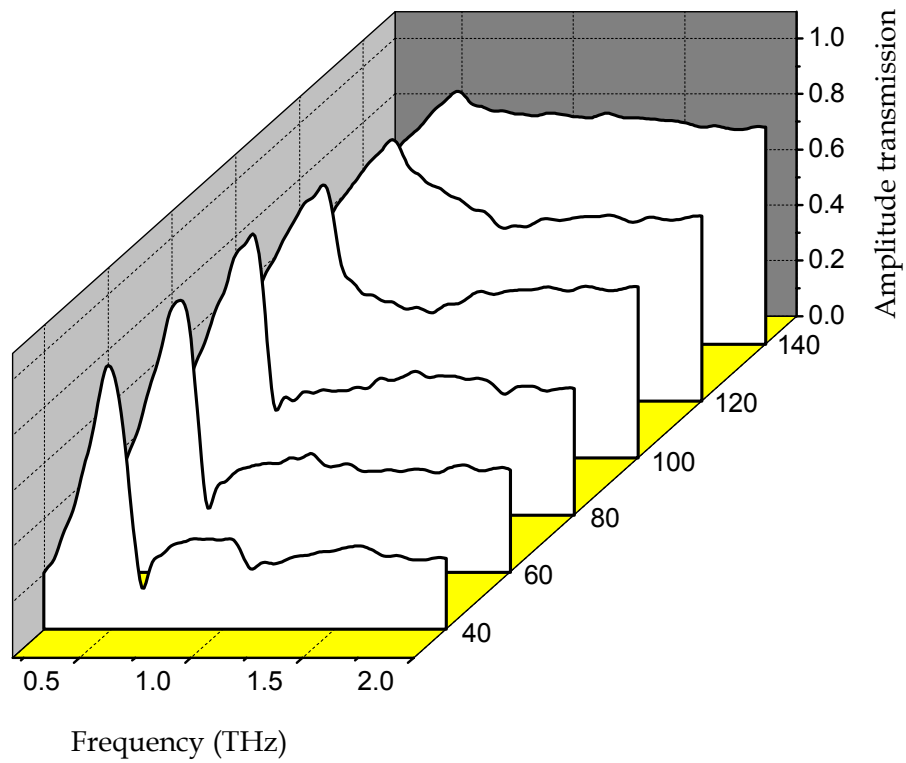
Figure 2-7 Measured frequency dependent amplitude transmission of the triangle lattice hole arrays with fixed hole length of 120 μm and various hole widths from 40 to 140 μm with an interval of 20 μm, and periodicity 160 μm, $E \parallel x$.
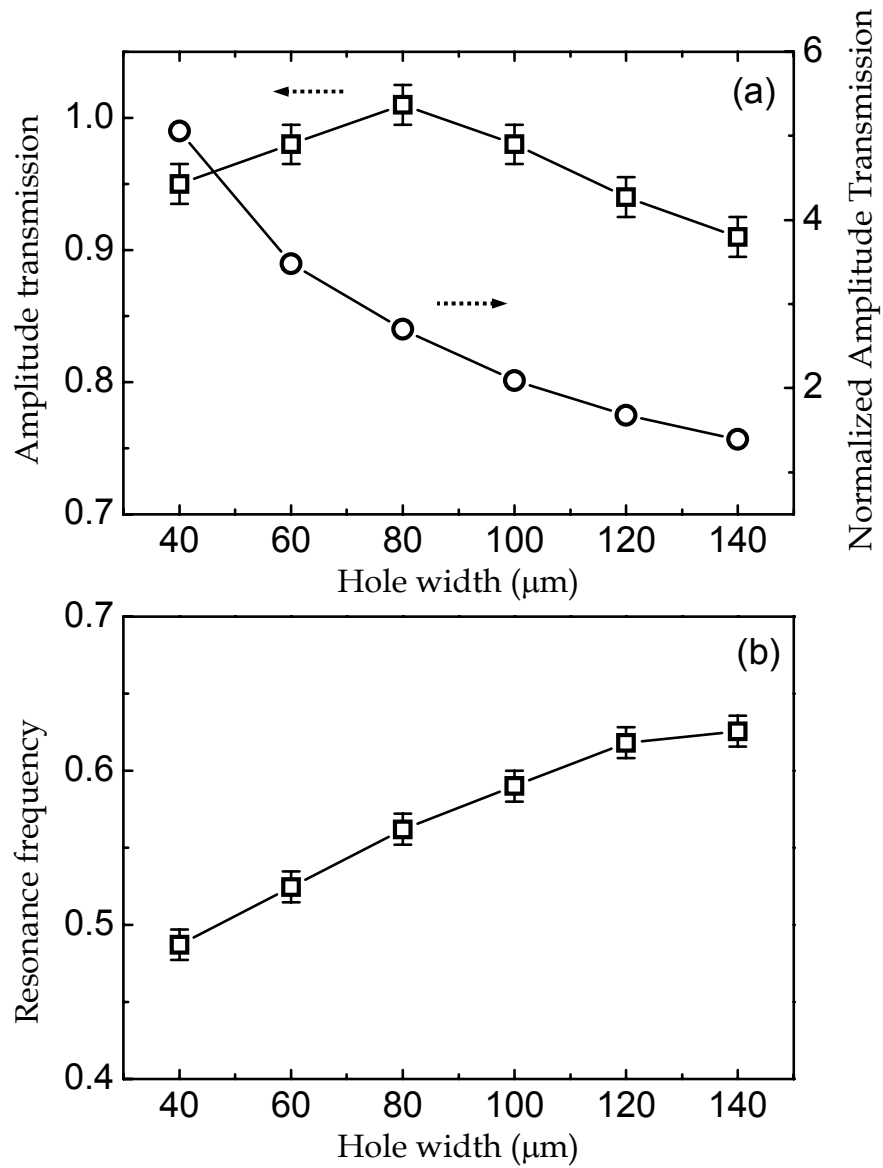
Figure 2-8 (a) Absolute peak transmission and (b) resonance frequency as a function of hole width. The solid lines are the guide to the eye.

44

2.5.2 Fano model

In 1961, U. Fano addressed that when a discrete state interacts with a continuum state, an asymmetric peak in the excitation spectrum will occur [36]. In this case, the Fano line shape instead of Lorentzian can be applied. As shown in Figure 2-9, the Fano model involves two types of scattering states: one refers to the continuum state Ψ_1, which is also called non-resonant state, and the other is the discrete resonant state Ψ_2 [37]. The total transition probability from the input state to the output state is calculated by solving the Haniltonian [37],

$$\hat{H} = \hat{H}_1 + \hat{H}_2 + \hat{V}. \qquad (2\text{-}1)$$

The eigenmodes of $\hat{H}_1$ are ψ_1, which corresponds to the state Ψ_1, as $\hat{H}_1\psi_1 = E\psi_1$; and $\hat{H}_2$ has the eigenmofrs of state Ψ_2, corresponding to the state ψ_2, $\hat{H}_1\psi_2 = E\psi_2$. The two states are coupled via term $\hat{V}$, which corresponds to the eigenmodes $V \cdot \psi$, the eigenmodes of $\hat{H}$ as $\hat{H}\psi = E\psi$ can derive the transition probability. The coupling between the continuum state ψ_1 and resonant state ψ_2 is assumed as Hamiltonian ,

$$\left\langle \psi_1 \middle| \hat{V} \middle| \psi_2 \right\rangle = V, \qquad (2\text{-}2)$$

which introduces resonance shift Δ and modified the linewidth δ. The transmission amplitude is defined as:

$$t = \left\langle \psi \middle| T \middle| i \right\rangle, \qquad (2\text{-}3)$$
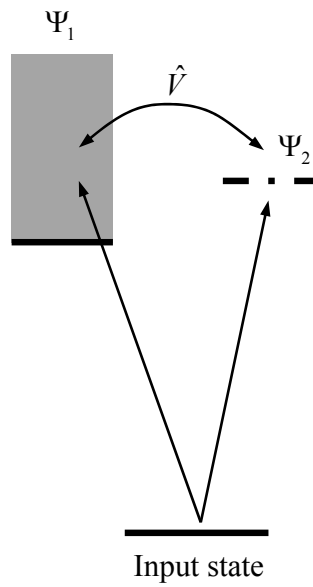
Figure 2-9 Schematic of coupled states in the Fano model [37], where Ψ_1 corresponds to the continuum state, Ψ_2 corresponds to the discrete state, $\hat{V}$ is the coupling term between Ψ_1 and Ψ_2.

with $|i\rangle$ being the input state, T is a suitable transition operator between initial state i

and the state ψ . Then the transition probability follows [37]

$$T = |t|^2 = T_b \frac{[E - (E_2 + \hbar\Delta) + \hbar\delta]^2}{[E - (E_2 + \hbar\Delta)]^2 + (\hbar\Gamma/2)^2} , \qquad (2\text{-}4)$$

where $E = \hbar\omega$, δ defines the ratio between the resonant transition amplitude and the

background transition amplitude, and T_b is the contribution of a continuum state that

couples with the discrete resonant state.

With $\varepsilon = \dfrac{E - (E_2 + \hbar\Delta)}{\hbar\Gamma/2}$, and $q = \dfrac{2\delta}{\Gamma}$, Equation (2-1) is simplified as

$$T = T_b (\varepsilon + q)^2 / (1 + \varepsilon^2) . \qquad (2\text{-}5)$$

The dimensionless parameter q determines the asymmetry of the lineshape. Fano model

provides physical understanding to the coupling between the continuum state and discrete

resonant states.

2.5.3 Fano fitting to the measured transmittance

The process of transmission through metallic hole array can be described by the Fano

model to address the characteristics of the spectrum line shape [36-38]. The Fano model

can be understood physically as illustrated in Figure 2-10. When an electromagnetic

wave propagate through hole array, the incident wave divides into two parts. One part

transmitted directly without any interactions is called direct transmitted continuum; this is

presented as T_a in Equation (2-3). T_a is not mentioned in Fano model in Section 2.5.2

because it is due to the direct transmission through the hole. The other incidence part is called non-resonant continuum, it couples with the discrete resonant state, which is characterize as resonance of SPs and LSP of holes, and then integrate with the direct transmission part, subsequently. Thereby, the transmitted waves through the system possess asymmetric line shape. For an isolated resonance, the Fano model can be written as

$$T_{fano} = |t(\omega)|^2 = T_a + T_b \, (\varepsilon_v + q_v)^2 / (1 + \varepsilon_v^{\,2}), \qquad (2\text{-}3)$$

where $\varepsilon_v = (\omega - \omega_v)/(\Gamma_v/2)$, T_a is a slowly varying transmittance which corresponds to the background transmittance, and $|T_b|$ is the contribution of a zero-order continuum state that couples with the discrete resonance state. The resonance state is characterized by the resonance frequency $\omega_v/2\pi$, the linewidth $\Gamma_v/2\pi$, and the Breit-Wigner-Fano coupling coefficient q_v [36-38]. During the fitting process, T_a, $\omega_v/2\pi$, and $\Gamma_v/2\pi$ can be figured out from the measurement, only $|T_b|$ and q_v are floats.
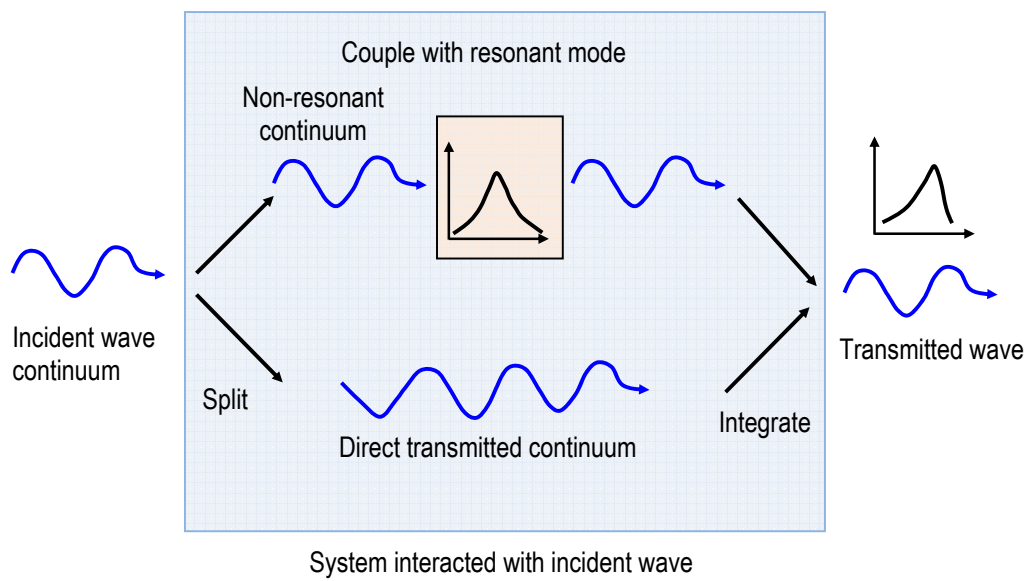
Figure 2-10 Physical understanding of Fano model

The measured transmittance of the random hole array with dimension 155×65 μm^2, $E \| x$, is fitted by the Fano model. Figure 2-11(a) shows the fano fitting (solid curve) to the transmittance of the random hole array. The fitting parameters are $\omega_v / 2\pi = 0.317$ THz, linewidth $\Gamma_v / 2\pi = 0.127$ THz, $T_a = 0.025$, $|T_b| = 1.18 \times 10^{-3}$ and $q_v = 9.95$. The resonance of the random hole array can be regarded as a result of coupling between the continuum incidence state and the discrete resonance state, i.e. the resonance of LSPs.

The measured transmittance of the 120×40 μm^2, periodicity 160 μm hole array is also analyzed by the Fano model that involves the coupled resonance of Al-Si SP [±1,0] modes and LSPs as the discrete resonant state [13]. The Fano model provides a consistent fit (solid curve) to the measured transmittance, as shown in Figure 2-11(b), with a single resonance at $\omega_v / 2\pi = 0.49$ THz, linewidth $\Gamma_v / 2\pi = 0.16$ THz, $T_a = 0$, $|T_b| = 1.28 \times 10^{-3}$ and $q_v = 26.5$. The contributions of direct transmission of terahertz pulses could vary with various hole width (or aspect ratio) and filling factor of metal.
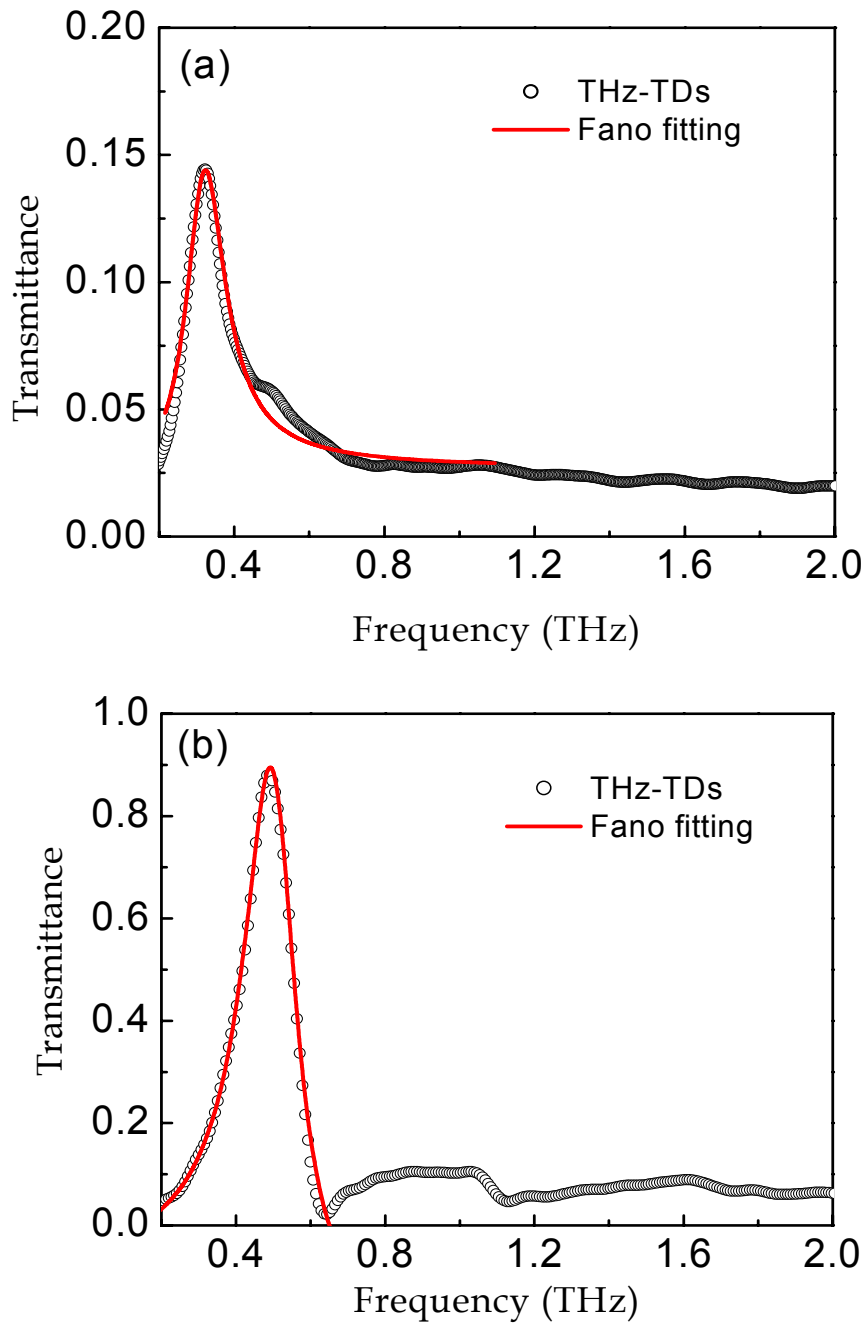
Figure 2-11 Measured (open circles) and theoretical fit by the Fano model (solid curve) of the frequency-dependent transmittance with (a) $155 \times 65 \ \mu m^2$, random hole array and (b) $120 \times 40 \ \mu m^2$, periodic triangle lattice hole array with periodicity 160 μm.

2.5.4 Coupling coefficient

Although the Fano model provides a good physical understanding of the characteristics of enhanced transmission in the hole arrays, the resonance coupling strength between SPs, LSPs and coupled continuum will be evaluated in this chapter by use of the Hamiltonian Matrices. In order to simplify the problem, the coupled continuum state is included in the LSP resonance, and will be used in the following Sections. In Figure 2-12, considering the uncoupled SPs and LSPs as two unperturbed states with corresponding eigenmodes, E_{SP} and E_{LSP}, respectively, the Hamiltonian can be defined as $\hat{H}_{SP}$ and $\hat{H}_{LSP}$. For the coupled resonances with two eigenmodes E_a and E_b, the Hamiltonian can be written as $\hat{H} = \hat{H}_{SP} + \hat{H}_{LSP} + \hat{V}$, where $\hat{V}$ stands for the coupling term. Thus [13,38]

$$\hat{H} = \begin{pmatrix} E_a & 0 \\ 0 & E_b \end{pmatrix} = \begin{pmatrix} E_{SP} & \kappa \\ \kappa^* & E_{LSP} \end{pmatrix} \qquad (2\text{-}4)$$

where κ and κ^* are the coupling coefficients between E_{SP} and E_{LSP} and conjugate with each other.
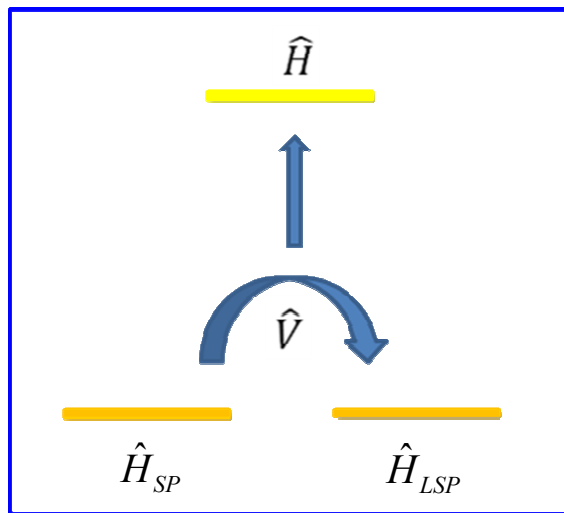
Figure 2-12 Schematic of coupling between SP and LSP in Hamiltonian

When the hole width increase from 40 to 140 μm, for each hole width, we have

$$\left(E_a - E_{SP}\right)\left(E_a - E_{LSP}\right) - |\kappa|^2 = 0 \qquad (2\text{-}5)$$

$$\left(E_b - E_{SP}\right)\left(E_b - E_{LSP}\right) - |\kappa|^2 = 0 \qquad (2\text{-}6)$$

The uncoupled state E_{SP} can be obtained from $\omega_{SP} = \dfrac{2\pi c\sqrt{m^2 + n^2}}{P\sqrt{\varepsilon_d}}$ for square lattice and

$\omega_{SP} = \dfrac{2\pi c\sqrt{m^2 + mn + n^2}}{P\sqrt{\varepsilon_d}}$ for triangle lattice. E_a and E_b can be retrieved from angle-

dependent transmission measurement (Table 2-1). Thus, we have two unknowns E_{LSP}

and $|\kappa|$. The calculated coupling coefficients $|\kappa|^2$ based on the experimental data by

changing hole width with $E \parallel x$ are shown in Figure 2-13. By increasing the hole width

from 40 to 140 μm, $\log(|\kappa|^2)$ decreases from -2.3 to -7.4. Let us recur to Section 2.5.1,

where an optimum hole width approached the maximum transmission at 80 μm. When

the hole width increases from 40 to 140 μm, coupling between SPs and LSPs decreases.

Although the direct transmitted continuum increases, the transmission achieves maximum

at 80 μm, and decreases with further increasing hole width.

	E_a (0°) (meV)	E_b (10°) (meV)	E_{SP} (0°) (meV)	E_{SP} (10°) (meV)
120 × 40 μm	2.017	2.030	2.592	2.711
120 × 60 μm	2.172	2.182	2.592	2.711
120 × 80 μm	2.327	2.333	2.592	2.711
120 × 100 μm	2.444	2.500	2.592	2.711
120 × 120 μm	2.560	2.576	2.592	2.711
120 × 140 μm	2.591	2.591	2.592	2.711

Table 2-1 SP modes of triangle lattice arrays at the Al-Si interface with 0° (E_a) and 10° (E_b) TM polarization incidence, respectively.
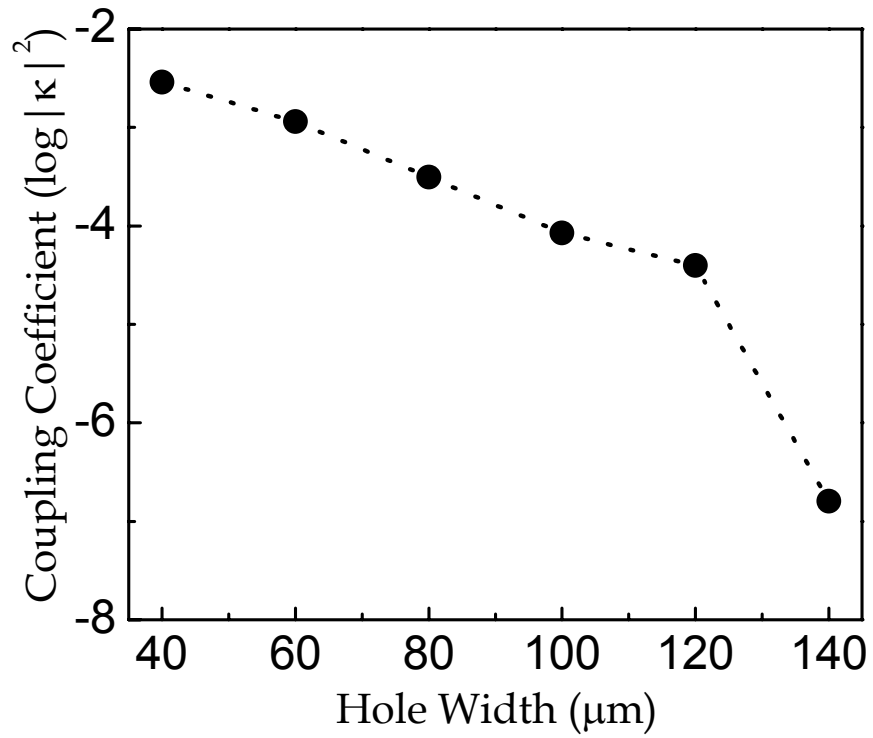
Figure 2-13 Calculated coupling coefficient of the resonant excitation of Al-Si SP [±1,0] modes with LSPs for different hole widths at normal incidence with hole length fixed to 120 μm and periodicity 160 μm. The dotted line is a guide to the eye.

2.5.5 Dependence of transmission on hole orientation

The orientations of asymmetric holes such as rectangular holes also influence the enhanced transmission properties, due to the alteration of the LSP resonance [10]. The amplitude transmission of different hole orientations of $100 \times 80 \ \mu m^2$, periodicity 160 μm square lattice hole array is shown in Figure 2-14, which manifests significant difference. When the hole orientation changes from $E \parallel x$ to $E \parallel y$, the amplitude transmission of the Al-Si SP [±1,0] mode decreases from 0.86 to 0.47, with a resonance frequency shifting from 0.51 THz to 0.55 THz. The LSP resonance experiences a weakened strength and blue-shift resonance frequency with hole orientation varying from $E \parallel x$ to $E \parallel y$, leading to decreased coupling between LSPs and the Al-Si SP [±1,0] modes, subsequently. By using Hamiltonian Matrix in Section 2.5.3, the coupling coefficient of the Al-Si SP [±1,0] modes and LSP resonance is calculated as $|\kappa|^2 = 0.9 \times 10^{-3}$ with $E \parallel x$, and $|\kappa|^2 = 0.37 \times 10^{-3}$ with $E \parallel y$, which agrees well with the experimental results.
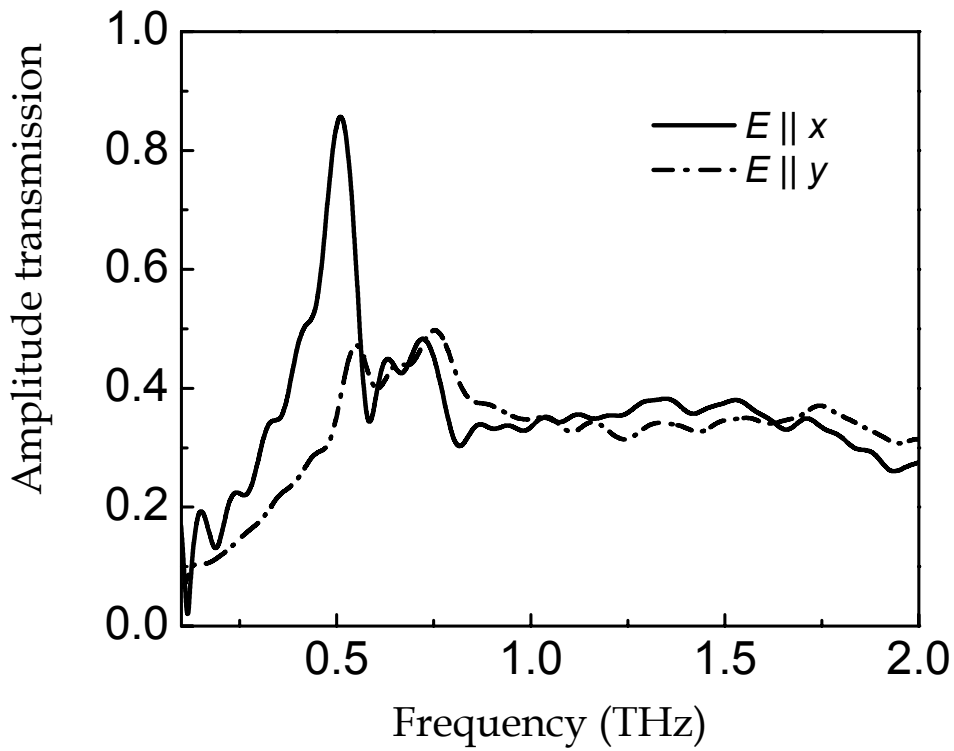
Figure 2-14 Measured amplitude transmission of the hole array with 100×80 μm^2, periodicity 160 μm, with different holes orientation $E \parallel x$ (solid curve) and $E \parallel y$ (dash-dotted curve).

Also, the electric field of different hole orientations is simulated by using CST Microwave Studio. This simulation tool is based on the finite integration technique (FIT), which represents a consistent transformation of the analytical Maxwell equations into a set of matrix equations. Within the frame of FIT, advanced meshing techniques such as the Perfect Boundary Approximation (PBA) and Thin Sheet Techniques (TST) can be implemented in both time and frequency domain solver. Also, FIT can be extended to consider the frequency dependence for permeability, permittivity and conductivity in one broadband simulation [38]. The simulated electric field of different hole orientations is shown in Figure 2-15, with $E \parallel x$, enhanced electric field is shown along the edge of holes compared to that of $E \parallel y$, which indicates strengthened coupling between LSPs and SPs.
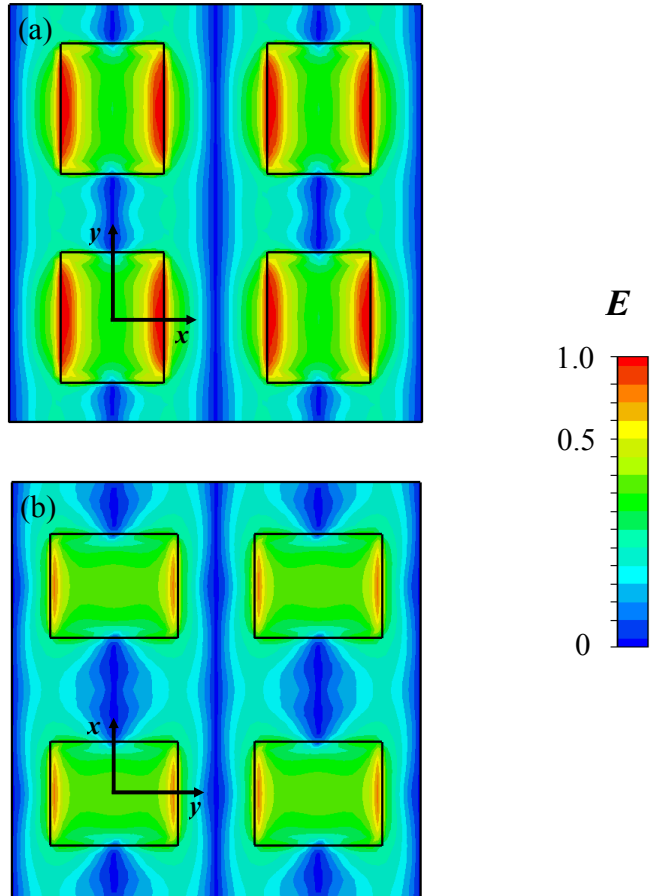
Figure 2-15 Simulated electric field distributions of hole array (a) $E \parallel x$, Al-Si SPP [±1,0] mode resonating at 0.51 THz, (b) $E \parallel y$, Al-Si SPP [±1,0] mode resonating at 0.55 THz. Dimension of holes is fixed as $100 \times 80 \ \mu m^2$, with periodicity 160 μm.

2.5.6 Dependence of transmission on incident polarization and angle of terahertz waves

As most enhanced transmission is observed at $E \parallel x$, our study on the dependence of transmission on different incident polarizations and angles is carried out at this particular orientation as well. Figure 2-16 shows the angle-dependent measurements on the array of hole dimensions 100×180 μm², periodicity 160 μm, with TM-polarization incidence. It clearly reveals both the Al-Si SP [±1,0] mode located at 0.51 THz and Al-Si SP [±1,±1] mode at 0.72 THz, experiencing split in the spectra with increasing incident angles. As introduced in Section 1.1.4:

$$k_{SP} = \frac{\omega}{c}\sqrt{\varepsilon_0}\sin\theta \pm mG_x \pm nG_y. \qquad (1\text{-}13)$$

Taking the contribution of in-plane wave vector $k_x = (\omega/c)\sin\theta$ into account, the resonance frequency of SPs is dependent on the incidence angle θ. The degenerated Al-Si SP [±1,0] mode at 0.51 THz splits into Al-Si SP [+1,0] and [−1,0] modes, and the Al-Si SP [±1,±1] mode at 0.72 THz is divided into Al-Si SP [+1,±1] and [−1,±1] modes.
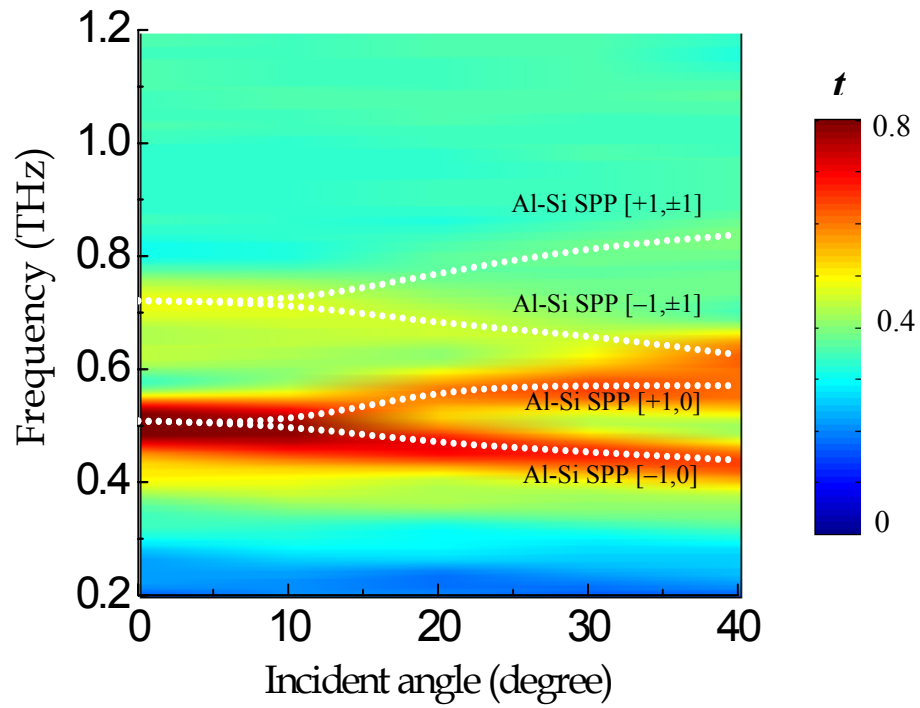
Figure 2-16 Measured angle-resolved transmission for hole array 100 × 80 μm², periodicity 160 μm, TM polarization, and $E \parallel x$. The dotted lines manifest the resonance modes.

When terahertz waves incident onto the same array under TE-polarization with different angles, different mode splitting is observed, as shown in Figure 2-17. Although the degenerated Al-Si SP [±1,±1] mode splits into Al-Si SP [±1,+1] and [±1,−1] modes, the Al-Si SP [±1,0] mode remains unchanged. This is because under TE-polarization, $k_y = (\omega/c)\sin\theta$, has no projection along [±1,0] direction, so the Al-Si SP [±1,0] mode remains degenerate and experiences no split. However, for the Al-Si SP [±1,±1] mode propagating along [±1,±1] direction, k_y has a 45° angle with respect to the SP propagating direction, which will be added or subtracted from reciprocal vectors, thus splitting is observed in the measured angle dependent spectra. The schematic of SP scattering on perforated metal film is shown in Figure 2-18.
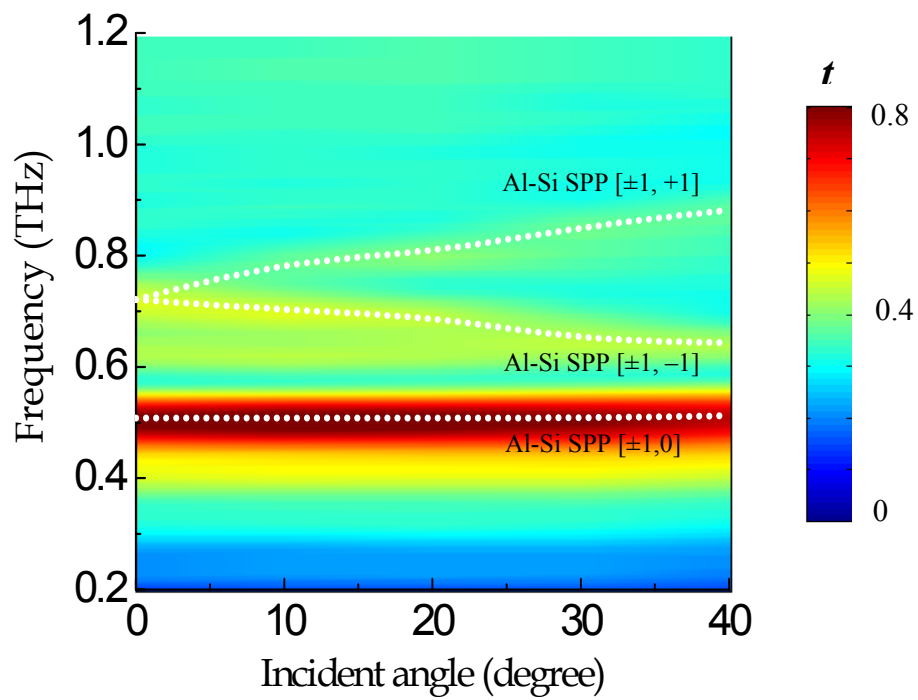
Figure 2-17 Measured angle-resolved transmission for hole array $100 \times 80\ \mu m^2$, periodicity 160 μm, TE polarization, and $E \parallel x$. The dotted lines manifest the resonance modes.
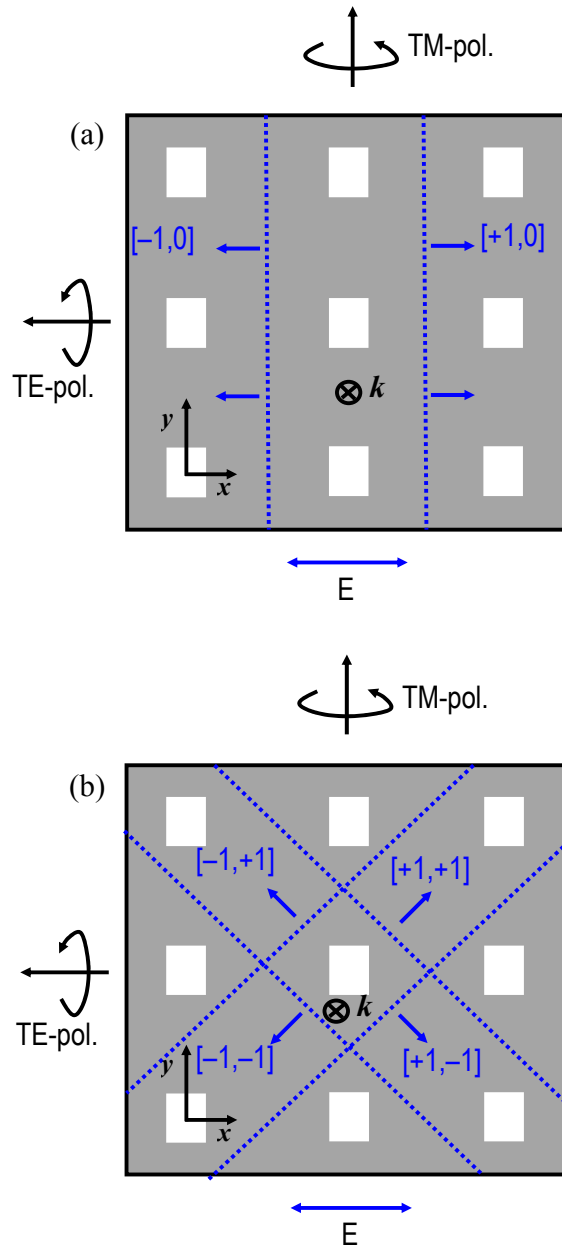
Figure 2-18 Schematic of the SP scattering on the metal film perforated with hole array, which corresponds to different SP modes. (a) SP [±1,0] mode, (b) SP [±1,±1] mode. The dotted lines and arrows manifest the propagation direction of SPs on the metal surface. *k* is the incident wave vector.

2.6 Conclusion

Resonant transmission of periodic and random subwavelength metal hole arrays is studied by THz-TDS. Enhanced transmission through random hole array indicates that the LSP resonance primarily contributes to enhanced transmission. Based on the results on LSPs, investigation of periodic hole array indicates that the enhanced transmission is due to the combination of SPs, LSPs and direct transmission. Coupling between SPs and LSPs is the key to obtain further enhanced transmission. Theoretical analysis by using the Fano model, Hamiltonian Matrix, and CST software simulation agrees well with the experiment results.

CHAPTER III

RESONANT PROPERTIES OF SUBWAVELENGTH METALLIC PARTICLES

When an electromagnetic wave impinges upon the surface of isolated subwavelength metallic particles, resonant reflection can be established due to excitation of DLSPs [40]. Under the influence of electric field, free electrons in metallic particles can be polarized and dipoles are induced consequently, thus leading to DLSPs. When the metallic particles are organized in a periodic array, the interaction between the DLSPs of adjacent particles becomes essential and makes a substantial contribution to the resonant reflection.

3.1 Experimental method

Square arrays of subwavelength metal structures are made from 190 nm-thick Al film by conventional photolithography, metallization, and lift-off processes on substrates of either silicon (0.64 mm thick, n-type resistivity $\rho = 12\ \Omega$ cm) or fused quartz (1.03 mm thick). Microscopy images of the metallic particle arrays are shown in Figure 3-1.
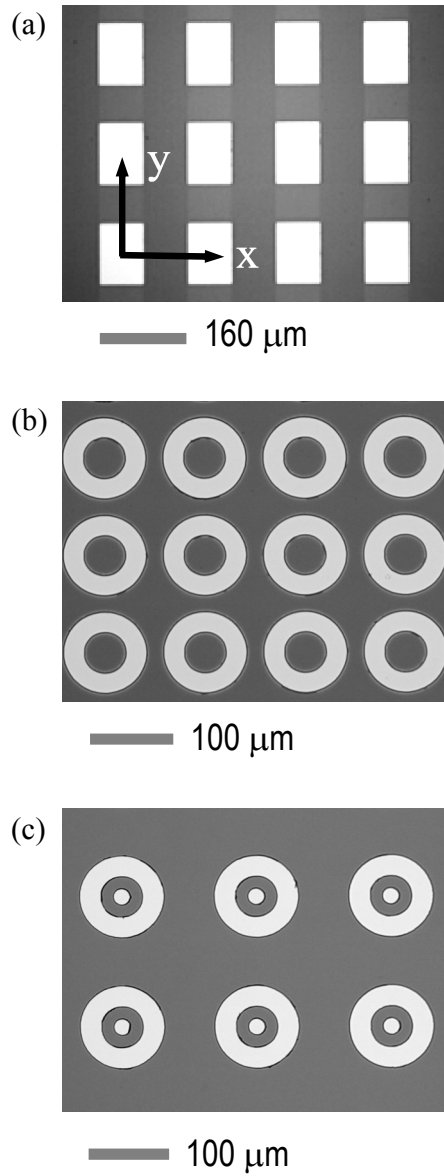
Figure 3-1 Microscopy images of the metallic (a) rectangle, (b) ring, and (c) coaxial particle array.

Resonant properties of the arrays are measured by use of photoconductive switch-based THz-TDS configured in a reflection geometry, as shown in Figure 3-2, where M_1, M_2 are parabolic mirrors that collimate the terahertz beam to be approximately parallel between M_1 and M_2. A beam-splitter (BS) is used together with M_3, M_4 and M_5 to guide the reflected terahertz beam from the sample to the receiver. The array sample, with dimensions of 25×25 mm^2, is positioned at the $1/e$ amplitude terahertz beam waist with radius of 8 mm at 0.5 THz [11]. An unpatterned 190 nm-thick Al film processed on an identical substrate is used as the reference in the THz-TDS characterization.
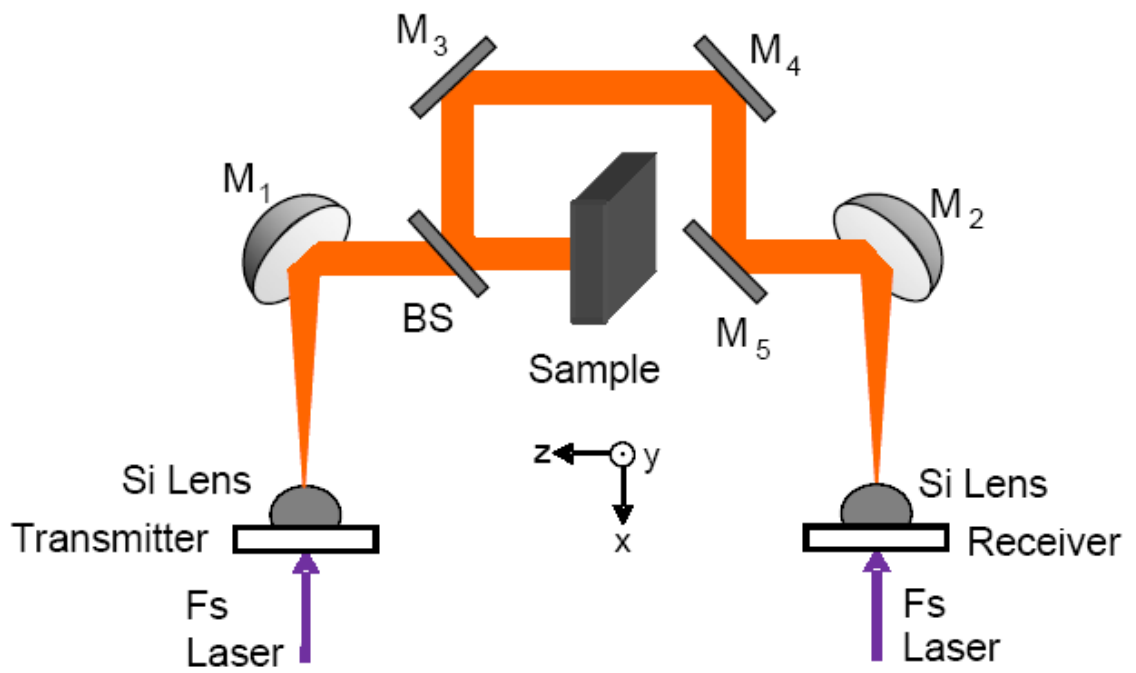
Figure 3-2 Experiment setup of the reflection THz-TDS system.

3.2 Data acquisition

The measured time-domain terahertz pulses reflected by an array of 80 μm (x axis) × 100 μm (y axis) Al rectangles patterned on silicon and the reference are illustrated in Figure 3-3(a) [14]. An unpatterned 190 nm-thick Al film processed on identical substrates is used as the reference in the THz-TDS characterization. The linearly polarized terahertz electric field is parallel to the long axis (y) of the rectangles, $E \parallel y$. The periodicity of the array is 160 μm along both x and y directions, giving the filling fraction of metal 31.25%. The absolute amplitude reflection is defined as $|r(\omega)| = |E_{out}(\omega)/E_{in}(\omega)|$, where $E_{out}(\omega)$ and $E_{in}(\omega)$ are the Fourier-transformed frequency dependent amplitudes of the measured terahertz pulses reflected by the array and the reference, respectively. The frequency-dependent reflectance can be extracted with the relation $R(\omega) = |r(\omega)|^2$. Figure 3-3(b) shows the frequency-dependent reflection $|r(\omega)|$ and the phase from the Fourier-transformed terahertz pulses.
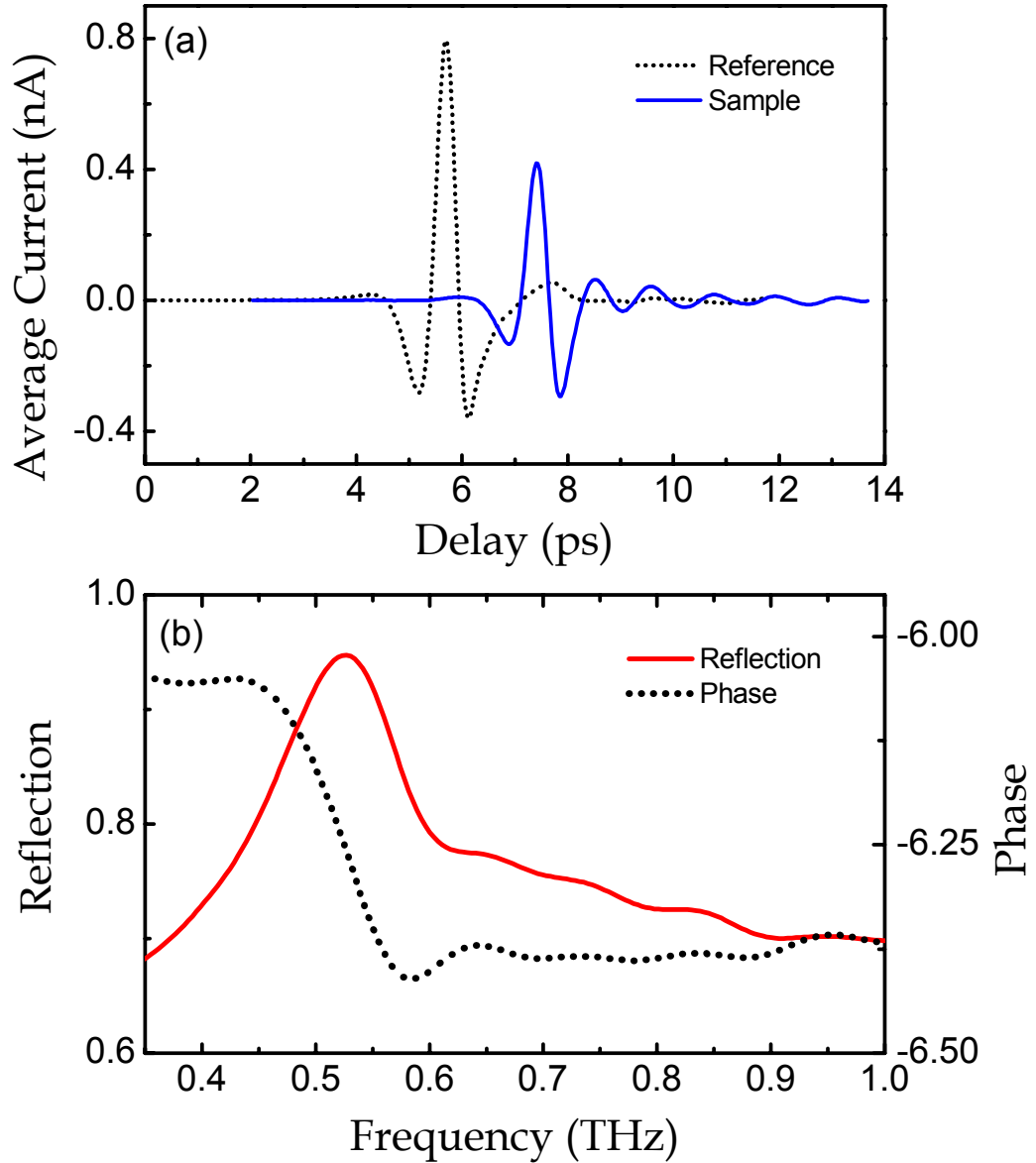
Figure 3-3 (a) Measured terahertz pulses reflected by the $80 \times 100 \ \mu m^2$ rectangle array patterned on silicon (periodicity 160 μm and $E \parallel y$, solid curve) and the reference (dotted curve), respectively. For clarity, the sample terahertz pulse is moved 2 ps horizontally. (b) Frequency-dependent reflection and the corresponding phase change.

3.3 Resonant properties of rectangular particle arrays

Under the condition of DLSPs induced by incident electromagnetic field, the single metallic subwavelength rectangle can be considered as a dipole antenna. The resonance frequency due to DLSPs excited at the rectangle can be approximately described by [41]

$$\omega_r / 2\pi = (c/2L)\varepsilon_d^{-1/2},$$
(3-1)

where L is the length of the rectangle parallel to the polarization of the incident electric field, ε_d is the dielectric constant of the substrate.

3.3.1 Dependence of reflection properties on the substrate media

Reflection properties of the array patterned on both silicon and quartz substrates are compared. As shown in Figure 3-4(a), a giant frequency shift of 0.30 THz is observed in the measured reflection for rectangles of dimensions 40×80 μm^2 as the boarding medium is changed from silicon to quartz. This result is considerably consistent with the dependence of resonance frequency on the dielectric function of substrates, $\omega_r / 2\pi \propto \varepsilon_d^{-1/2}$ [41], here $\varepsilon_d = 3.82$ for the fused quartz. There is no clear difference in peak reflection; however, the background reflection shown at the non-resonant frequencies with the quartz substrate is significantly reduced. This is mainly due to the lower dielectric constant of quartz than that of silicon, giving rise to a reduced background reflection by the non-metal sites of the array.
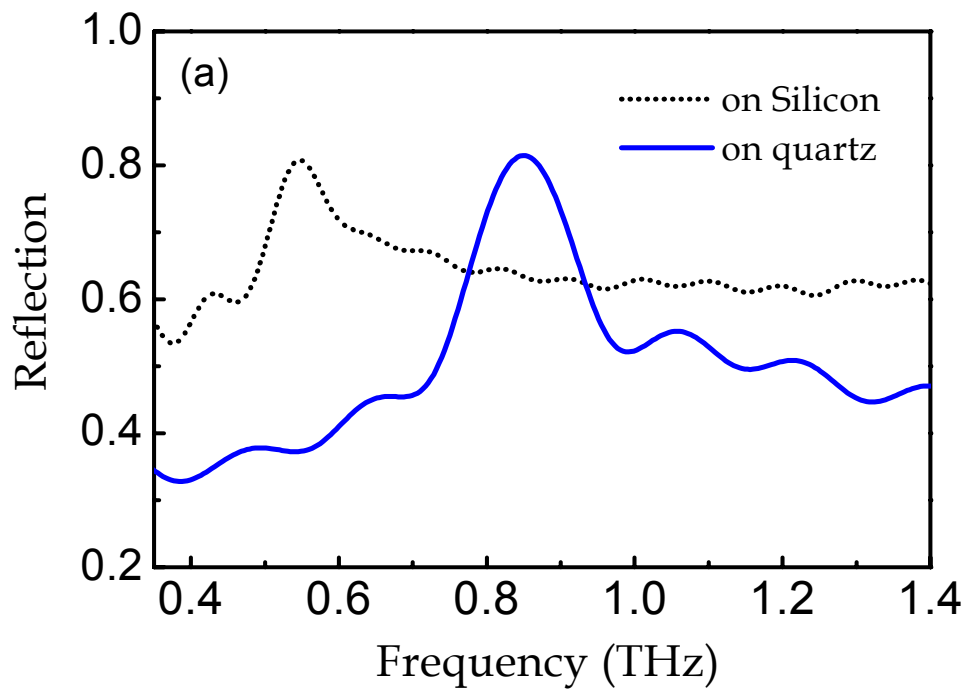
Figure 3-4 Measured frequency-dependent reflection of the Al rectangles with dimensions of 40 μm (*x* axis) × 80 μm (*y* axis) and periodicity 160 μm on silicon and quartz substrates with terahertz electric field $E \parallel y$.

3.3.2 Effect of particle orientation and shape

In Figure 3-5 we show the dependence of resonant reflection on particle orientation. With the 80 μm (x axis) × 100 μm (y axis) rectangles arranged in a square lattice of periodicity 160 μm, both the resonance frequency and the reflection exhibit particle orientation dependent behavior. The resonance frequency shifts from 0.55 to 0.52 THz as the particle orientation rotates from $E \parallel x$ to $E \parallel y$, while the peak reflection is enhanced from 0.85 to 0.95. This can be explained when the terahertz pulses are incident upon the array, the polarized electric field induces opposite signs of charges at the edge of the isolated rectangle along the polarization of electric field. As such, particles can be treated as electric dipoles, which resonant along the direction of applied electric field, thus giving rise to DLSPs [42]. When the particle orientation rotates from $E \parallel x$ to $E \parallel y$, the particle length along the electric field increases, resulting in strengthened dipole resonance and red-shift frequency, as shown in Figure 3-5.

To explore the shape dependent reflection properties, a square array of circular structures with a diameter of 100 μm is patterned on silicon, while the other parameters remain the same as those of the 80×100 μm^2 rectangles. As shown in Figure 3-5, the peak reflection of the circular structures approaches 0.89, which sits right between that of the rectangle with two different orientations. This result indicates that the resonant reflection of subwavelength metallic particles with similar filling fractions indeed exhibits shape dependent behavior.
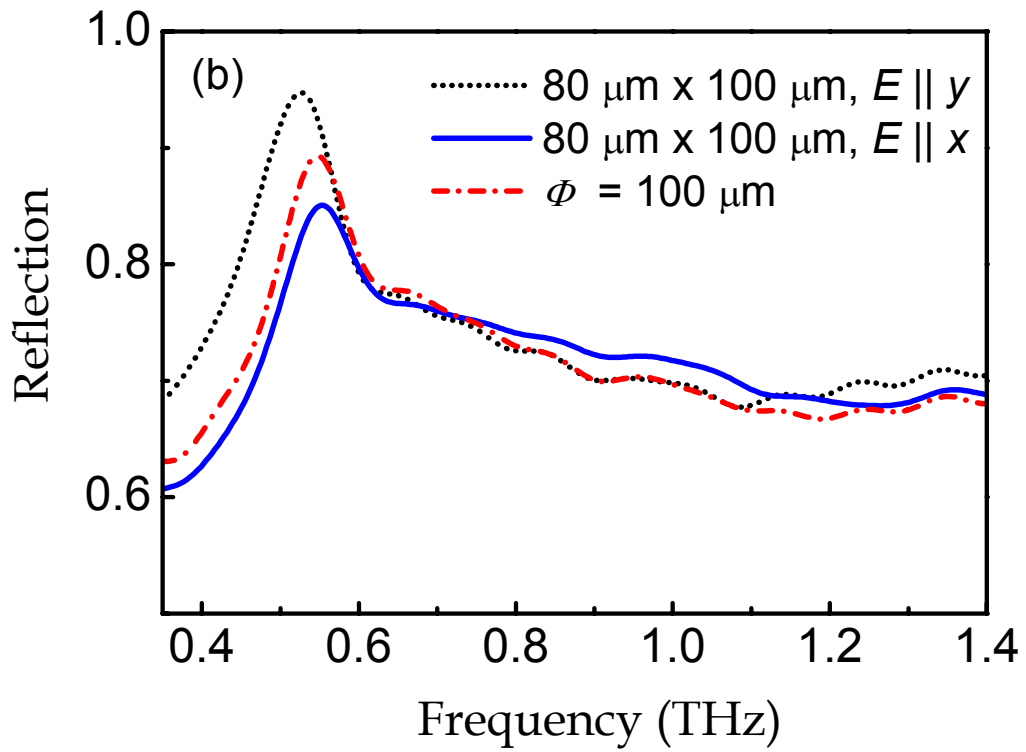
Figure 3-5 Comparison of measured reflection of the $80 \times 100 \ \mu m^2$ rectangles with different polarizations of incident terahertz field and the circular structures of a diameter $\Phi = 100 \ \mu m$. These metal structures are patterned on silicon with the same periodicity 160 μm.

3.3.3 Dependence of reflection on periodicity of the particle array

When the single particles are organized in an array, coupling between the particles also influence the DLSP resonance. The effect of periodicity of metal rectangles on resonant reflection is also characterized. A set of square arrays of $80 \times 100 \ \mu m^2$ rectangles with various periodicities are processed on silicon substrates. When the periodicity varies from 160 to 280 μm, as shown in Figure 3-6, both the measured peak reflection and resonance frequency exhibit a characteristic evolution. The peak reflection decreases with increasing periodicity due to reduced density of rectangles, as well as the degraded interaction between DLSPs of the adjacent rectangles. This periodicity dependent resonance shift is primarily due to the interaction between DLSPs of the adjacent rectangles and can be explained in terms of effective circuits, i.e. RC resonance, which treats the Al rectangles as resistors and the gaps between rectangles as capacitors. When the periodicity increases, the attraction of the charges distributed along the gap decreases. As a result, much less charges are accumulated at the opposite ends of rectangles, and the capacitance in the gap diminishes, resulting in red-shift of resonance frequency. However, when the periodicity is beyond 240 μm, the resonance frequency does not show further shift because the interaction between the DLSPs of adjacent rectangles becomes negligible.
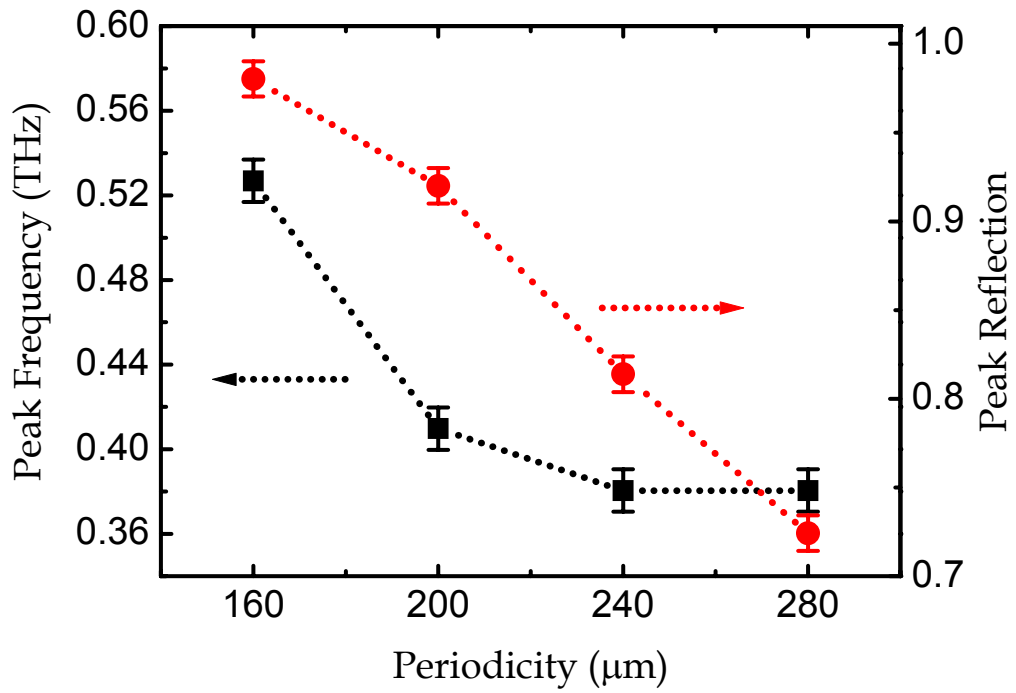
Figure 3-6 Measured dependence of resonance frequency and peak reflection on periodicity of the rectangle array on n-type silicon. The periodicities are 280, 240, 200, and 160 μm, respectively. The dimensions of the rectangles are 80×100 μm^2, $E \parallel y$.

3.3.4 Numerical simulations

The resonant reflection of the rectangle particle arrays is simulated using CST Microwave Studio. The solid curve in Figure 3-7 shows a simulated resonant reflection of the $100 \times 80 \ \mu m^2$ rectangles with a 160 μm periodicity and $E \parallel y$. It shows a good agreement with the experimental data and captures most of the observed behavior, such as the resonance frequency, amplitude, and line shape. The simulated reflection linewidth, however, appears slightly broader due to possible experimental variations in the Al thin-film conductivity and patterned structures. The conductivity of metal thin films may vary remarkably from the bulk conductivity used in the simulation due to complex deposition process [43,44].
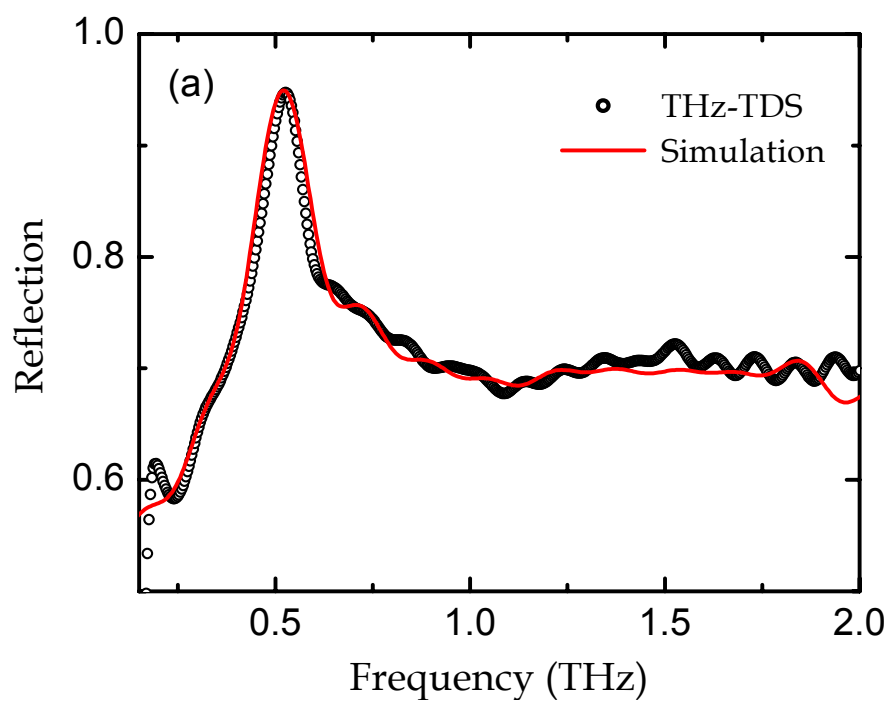
Figure 3-7 Measured (open circles) and CST Microwave Studio simulated (solid curve) frequency-dependent reflection of the 80 μm (*x* axis) × 100 μm (*y* axis) Al rectangles patterned on silicon with a period of 160 μm and $E \parallel y$.

Figures 3-8(a) and (b) illustrate the simulated electric field distributions of the arrays with two different periodicities, 160 and 240 μm, respectively. In Figure 3-8(a), electric field coupling is clearly revealed at the gaps along the incident terahertz electric filed due to interactions of DLSPs between the adjacent rectangles. When the periodicity is increased from 160 to 240 μm, however, this interaction is extensively degraded, as shown in Figure 3-8(b), confirming the contributions of DLSP interactions to the observed periodicity dependent characteristic reflection [31].

In order to clarify the shape dependent behavior of DLSPs, we simulated the electric field distributions in the arrays of the circular disk of 100 μm diameter, periodicity of 160 μm. As shown in Figure 3-8(c), with different particle shapes, the edge profile leads to different coupling status between the DLSPs. As a result, the electric field distributions and the DLSP resonant properties become different, consequently.
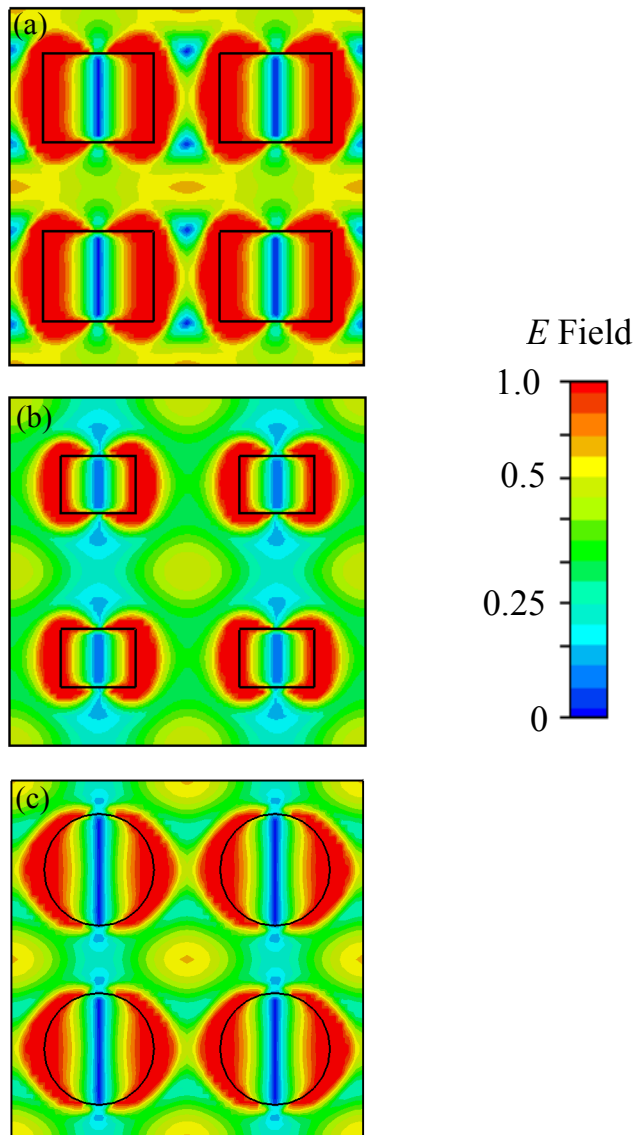
Figure 3-8 Comparison between the simulated electric field distributions of (a) rectangle (100 $\times$ 80 μm^2, periodicity 160 μm), (b) rectangle (100 $\times$ 80 μm^2, periodicity 240 μm), and (c) circular disk (D = 100 μm, periodicity 160 μm) metallic particle arrays.

3.3.5 Comparison between reflection and transmission properties of the rectangular particle array

When metallic particle is irradiated by incident electromagnetic wave, the conduction electrons in metal absorb the energy from incident wave to make oscillation and radiate back to electromagnetic wave, which is called scattering. In the terahertz domain, the metal dielectric constant is so large that the scattering can be treated as total reflection. The resonance of metallic particles in the terahertz domain can be characterized by either reflection maximum or transmission minimum. The measured reflection and transmission of a rectangle array are shown in Figure 3-9(a). The reflection maximum corresponds well to the transmission minimum, the larger reflection maximum, which manifests the stronger resonance intensity, is consistent with the smaller transmission minimum.

Compared to reflection measured with the same sample, the transmission possesses narrower linewidth, and experiences a slight frequency shift. For subwavelength particles, the incident wave may creep around the particle edge and approach un-illuminated region of the particle, which is called "edge effect" [24]. The incident wave caused by the "edge effect", which makes conduction electrons resonate at the un-illuminated side of particles, will not influence reflection spectrum but will bring sharper resonance and frequency-shift in transmission, as shown in Figure 3-9(b). As sharper line shape in the transmission spectrum is more sensitive to the resonance, transmission spectrum is characterized for DLSP resonances in the following Sections.

0
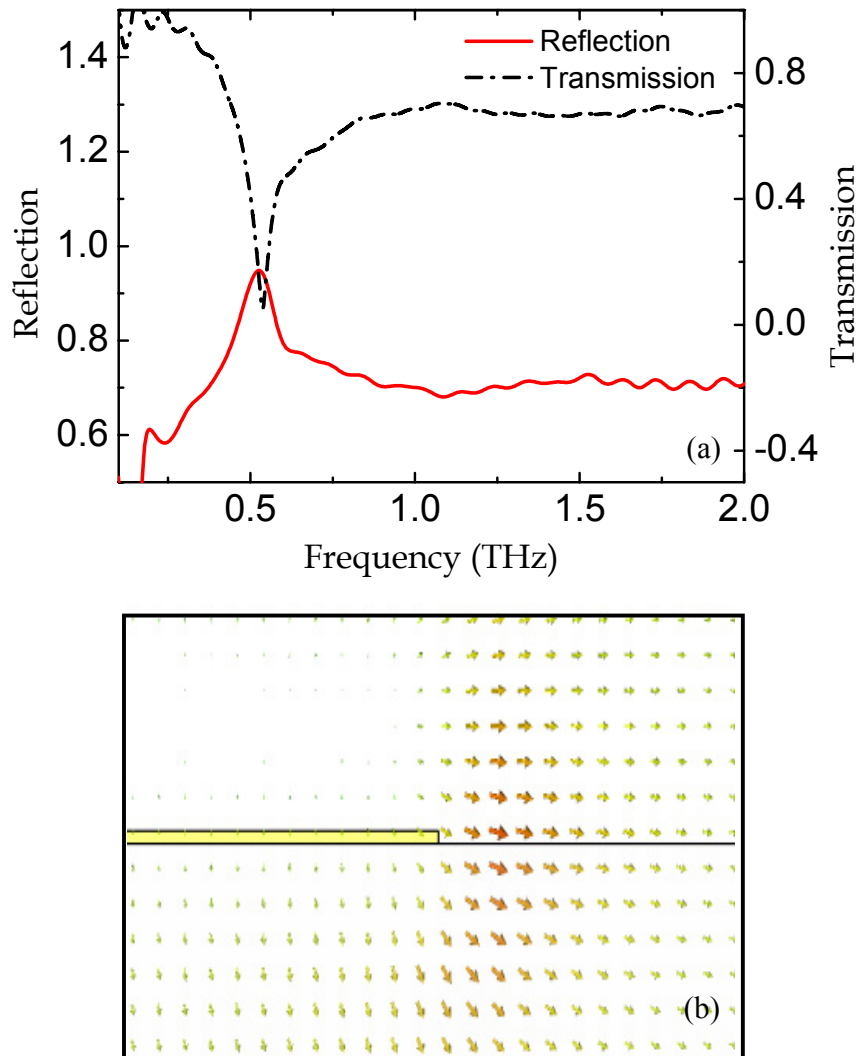
Figure 3-9 (a) Measured frequency-dependent reflection (solid curve) and transmission (dash dotted curve) of the $100 \times 80 \ \mu m^2$ Al rectangles patterned on silicon with a periodicity of 160 μm, and $E \parallel y$. (b) Schematic of electric field distribution caused by "edge effect". The arrows denote electric fluxlines.

3.3.6 Dependence of transmission on incident polarization and angle of terahertz wave

Measured transmission of Al rectangles with TM polarization incidence wave is shown in Figure 3-10(a). No frequency shift is observed when the incident angle is changed, which manifests the dipole properties of the particle resonance. The diminished transmission minimum with varying incident angle is due to the decreasing of effective dipole moment parallel to incident electric field caused by angle rotation. The TE polarization incidence transmission in Figure 3-10(b) also shows similar characteristics but much less difference in resonant transmission due to unaltered dipole moment with different angles.
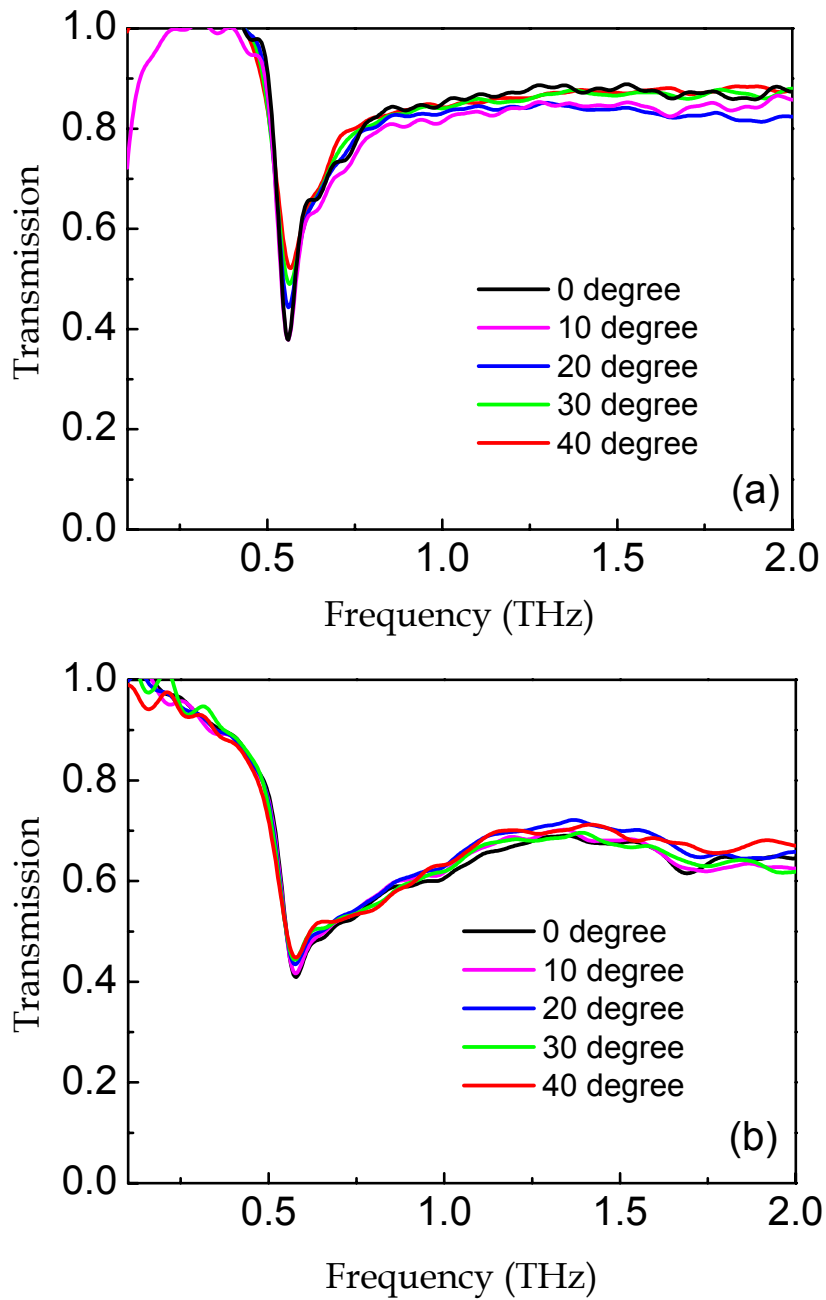
Figure 3-10 angle-independent transmission of (a) $80 \times 40\ \mu m^2$ rectangles array $E \parallel y$, TM polarization, and (b) $100 \times 80\ \mu m^2$ rectangles array $E \parallel x$, TE polarization, both with periodicity 160 μm.

3.4 Resonant properties of ring particle arrays

Compared to the disk counterparts, the ring shape particles deliver larger electromagnetic field enhancement, narrower linewidth, and improved tunability at the plasmonic resonance. Such characteristics make the ring particles preferable in diverse applications such as sensors, waveguides, and frequency selective surfaces [45-48]. In particular, close-ring resonators have also been used as a functional element in metamaterials towards negative index of refraction in the visible spectral regime [49].

3.4.1 Dependence of transmission on periodicity and shape of the rings

The effect of periodicity and shape of metal ring particles is studied by THz-TDS transmission measurements. The transmission of ring arrays of Φ_{ID} = 75 μm, Φ_{OD} = 100 μm with various periodicities from 120 to 240 μm is shown in Figure 3-11. Both the measured transmission and resonance frequency exhibit similar characteristic evolution with that of rectangular particle array studied in Section 3.3.3. The transmission minima increase with increasing periodicity due to the degraded interaction between DLSPs of the adjacent rings, corresponding to the decreased resonance intensity. Also, periodicity dependent resonance is observed, showing red-shifted resonance frequency with increasing periodicity. However, when the periodicity is increased beyond 200 μm, the resonance frequency reveals a slightly blue-shift, which is believed as a result of frequency identification error. In addition, the resonant transmission is found to depend on the ring shapes, as shown in Figure 3-12. Clearly, the subwavelength square rings (inner length = 50 μm, outer length = 100 μm) present much enhanced resonance

behavior compared to that of the circular rings of $\Phi_{ID} = 50$ μm and $\Phi_{OD} = 100$ μm. The stronger resonance of the square rings is due to higher charge density around sharper edges compared to the circular rings.
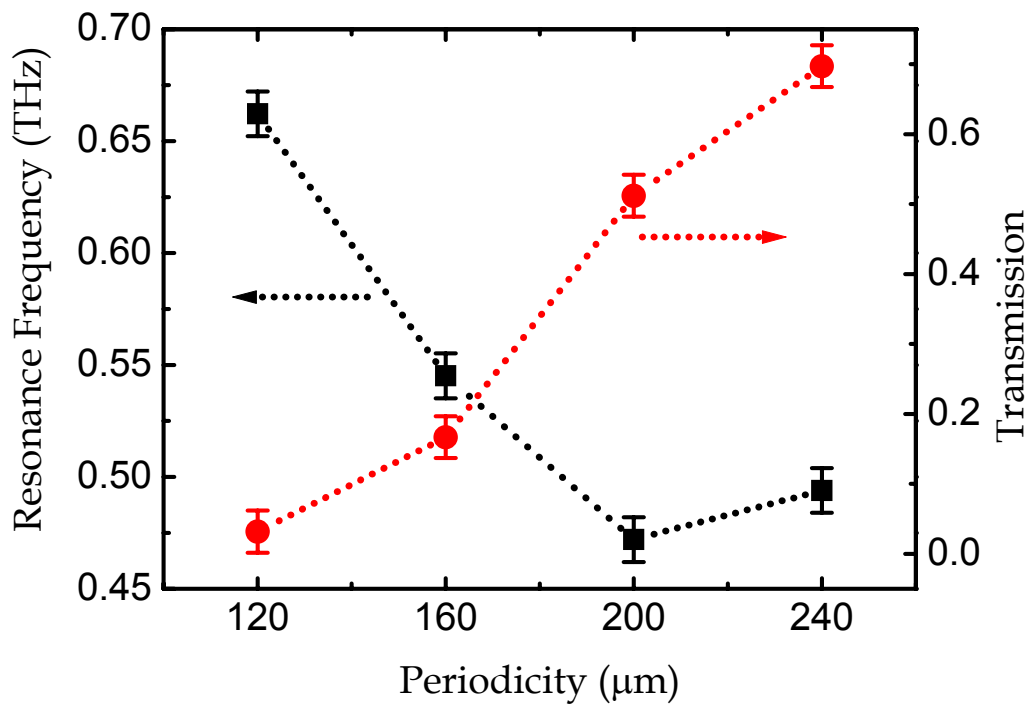
Figure 3-11 Dependence of resonance frequencies and peak reflection on periodicity. The dimensions of the rings are $\Phi_{ID} = 75$ μm and $\Phi_{OD} = 100$ μm.
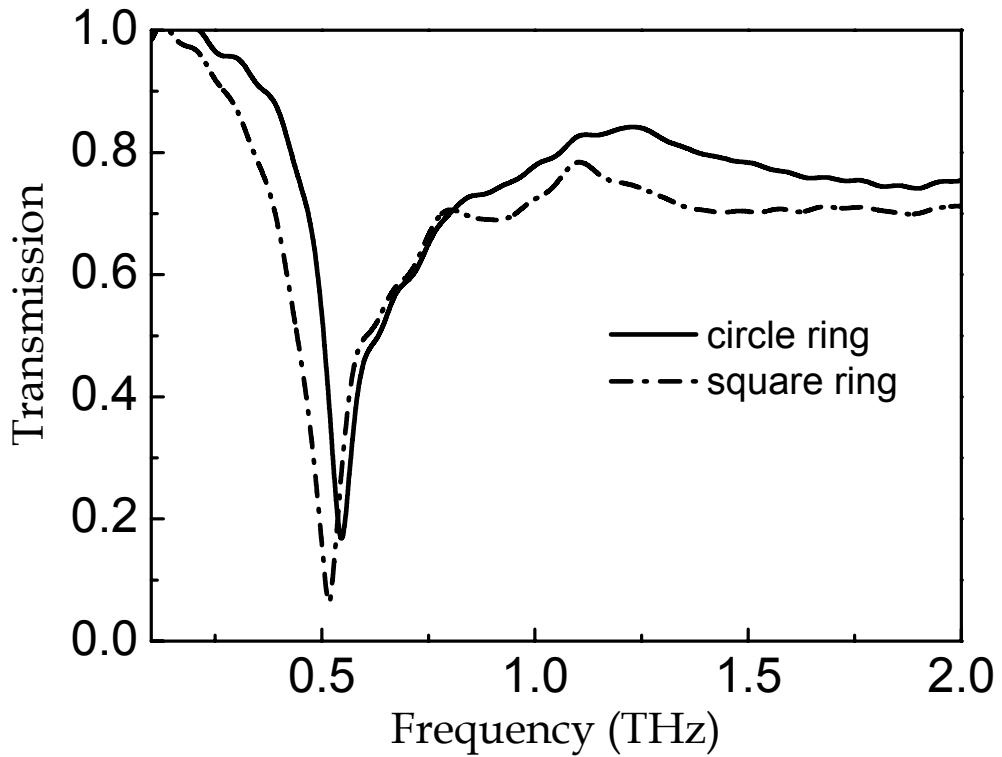
Figure 3-12 Comparison of measured transmission of the ring arrays with different shapes. Circular ring: Φ_{ID} = 50 μm, Φ_{OD} = 100 μm (solid curve), square ring: inner length = 50 μm, outer length = 100 μm (dash-dotted curve). The metal structures are patterned on silicon with the same periodicity of 160 μm.

3.4.2 Effect of the inner diameter of the rings

Transmission resonance with different inner diameters of the ring particles is shown in Figure 3-13(a) [50]. With a fixed Φ_{OD} as 100 μm, the increase of Φ_{ID} from 0 to 75 μm enables the transmission minimum to be monotonously strengthened from 0.287 to 0.107. However, it becomes weaker when Φ_{ID} increases further up to 90 μm. Meanwhile, the resonance shifts from 0.56 to 0.45 THz with increasing Φ_{ID}, as summarized in Figure 3-13(b). Since the strength of DLSPs is closely related to the particle dipole moment, which is determined by the amount of induced charges and the separation between the charges of opposite signs. When Φ_{ID} increases from 25 to 75 μm, the dipole moment resulted from the charges and the mean separation of the charges increases, thus enhancing the DLSP resonance. When Φ_{ID} is greater than 75 μm, the induced charges that decrease with diminished areas of the ring walls are no longer strong enough to compensate the increased separation between the charges. Therefore, the degraded dipole moment results in decreased peak resonance at Φ_{ID} = 90 μm. As a whole, there exists an optimum ring wall thickness at which the strongest resonance is approached.

As mentioned above, the increased Φ_{ID} enlarges the separation between the charges at the opposite sides of the rings, thus degrading the force between the intraring charges and consequently leading to a red-shift in resonance. In addition, the resonance linewidth is observed to narrow down with increasing Φ_{ID} due to reduced damping of the DLSPs resulted from less radiative decay as the particle volume decreases [51,52]. There is no

obvious resonance difference as Φ_{ID} increases from 0 to 25 μm due to negligible

variation of charges and the separation between them.
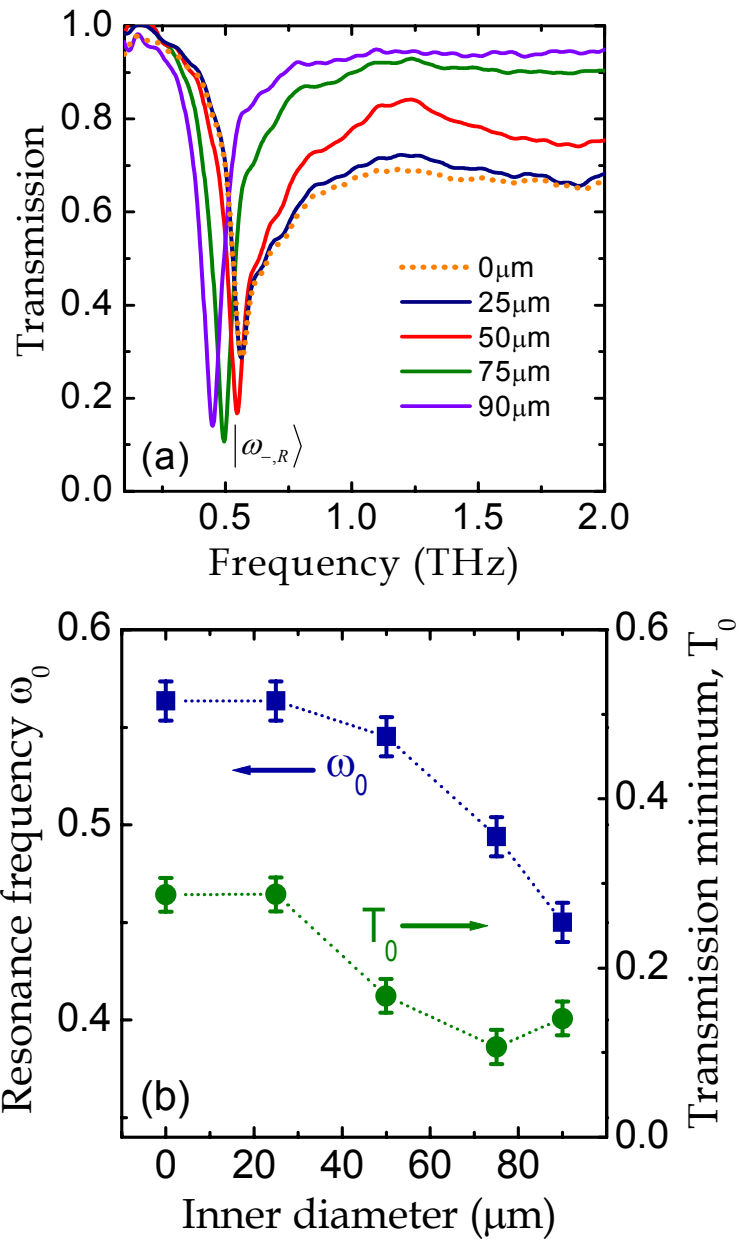
Figure 3-13 (a) Measured frequency-dependent amplitude transmission of the rings with various Φ_{ID}, as shown in the legend. (b) Resonance frequencies (squares) and transmission minima (circles) as functions of Φ_{ID}.

At visible frequencies, although two resonances, the symmetric and antisymmetric modes, were theoretically characterized in the rings, only the symmetric mode was yet observed [47]. Here, besides the strong and sharp symmetric mode, $\left|\omega_{-,R}\right\rangle$ that induces same signs of charges at the inner and outer ring walls, a weak and broad asymmetric mode, $\left|\omega_{+,R}\right\rangle$ around 1.8 THz is also experimentally observed with Φ_{ID} = 50 μm. Different from the symmetric mode, the charge distribution of the asymmetric branches corresponds to the patterns of opposite signs along both ring walls. Schematic charge distribution of the symmetric and antisymmetric modes of the rings is illustrated in Figure 3-15(b). When the inner diameter is in the range from 0 to 25 μm, it appears so small that the resonance reveals only minor difference. When the inner diameter is further increased, however, intensified oscillation occurs between the inner and outer walls, thus leading to resonance blue-shift. With Φ_{ID} > 75 μm, the asymmetric resonance shifts further to higher frequencies.

3.4.3 Numerical simulations

The electric field of the symmetric mode resonance for two different inner diameters Φ_{ID} = 25 and 75 μm is further examined by using CST Microwave Studio simulation. It reveals in Figures 3-14(a) and (b) that the electric field distribution at the surface of the rings is clearly enhanced at the resonance frequencies as Φ_{ID} increases from 25 (0.55 THz) to 75 (0.50 THz) μm. This can be further confirmed by the electric field distribution at the cross section cutting along the ring axis, as illustrated in Figures 3-14(c) and (d). With Φ_{ID} = 75 μm, it shows stronger coupling of DLSPs along the thinner ring wall as

compared to that of the $\Phi_{ID} = 25$ μm rings, which only bear DLSPs along the outer edge of the ring. Figures 3-14(e) and (f) illustrate the current density distribution of these rings. Being consistent with the electric filed distribution, the ring of $\Phi_{ID} = 75$ μm exhibits stronger current density than that of the ring of $\Phi_{ID} = 25$ μm. This indicates that the induced charge density is higher along the thinner ring wall.
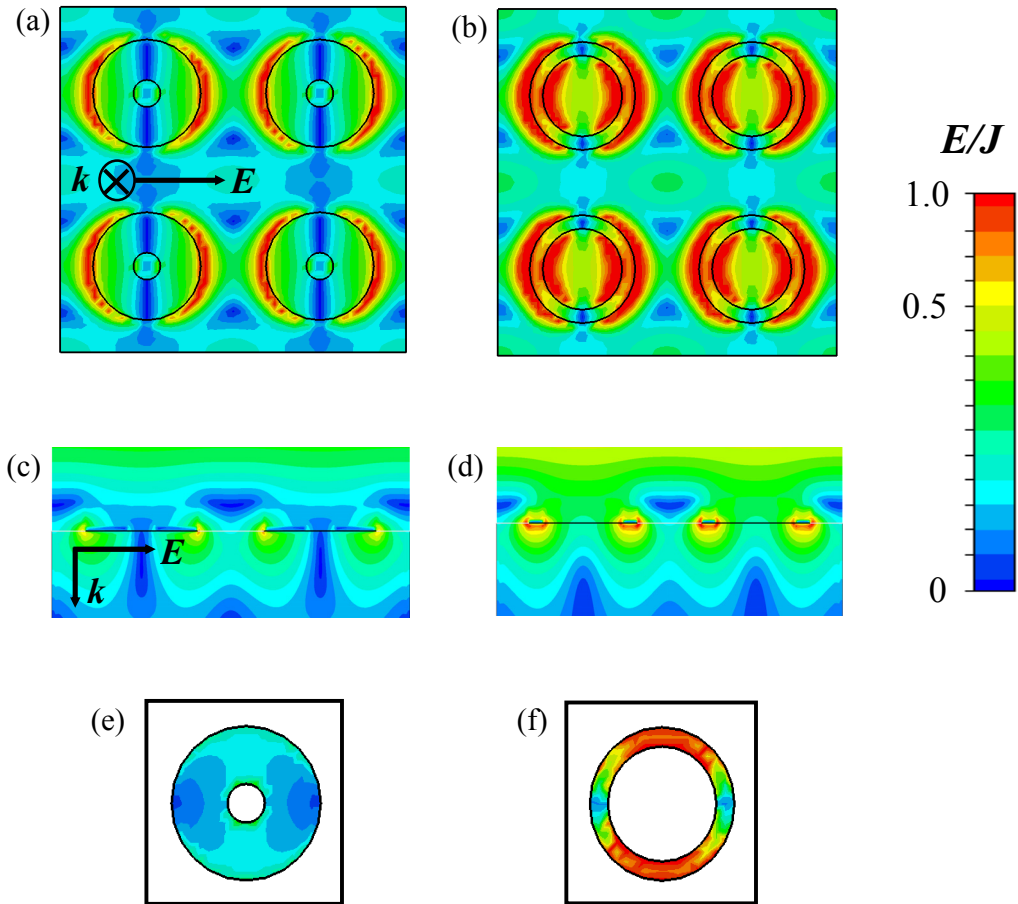
Figure 3-14 Simulation results: (a), (b) electric field distributions on the surface of the rings; (c), (d) electric field distributions at cross section cutting along the ring axis; (e), (f) current density. Two ring arrays of fixed $\Phi_{OD} = 100$ μm and (a), (c), (e) $\Phi_{ID} = 25$ μm, resonating at 0.55 THz; (b), (d), (f) $\Phi_{ID} = 75$ μm, resonating at 0.50 THz.

3.5 Resonant properties of coaxial particles

For comparison purpose, resonant properties of subwavelength coaxial structures composed of a ring and an inner disk are also investigated. The coaxial particles deliver even larger electromagnetic field enhancement, and narrower linewidth at the plasmonic resonance compared to the rings. Also, according to the plasmon hybridization theory [53], based on the gap between ring and inner disk as well as the energy difference between their plasmon modes, the intensity of interaction between the ring and inner disk can be adjusted, which bears flexible design to coaxial particle structures.

3.5.1 Plasmon hybridization theory

The definition of hybridization was first originated from chemistry, which described that the mixing of atomic orbitals forms new orbitals suitable for stable bonding [54]. Hybridization is analogous to coupling, but possesses its own properties: the number of participant atomic orbitals does not change, but the stretching direction and shape of atomic orbitals change after hybridization. E. Prodan and his co-workers introduce the chemistry term into plasmon hybridization theory to describe the plasmon resonance behavior of composite metallic nanostructures of greater geometrical complexity [53]. This is an unique model that provides in-depth understanding and guidance in the design of metallic nanostructures and predict their resonant properties.

Here, the plasmon hybridization theory is used to analyze the resonant behaviors of the coaxial particle structures [50]. As shown in Figure 3-15(a), a coaxial structure can be regarded as a combination of ring and inner disk particles. Based on the gap between the

ring and inner disk as well as the energy difference between their plasmon modes, the resonance of the coaxial structures can be understood through the plasmon hybridization theory. The energy-level diagram depicting the interaction between the outer ring and inner disk is shown in As the antisymmetric mode, $\left| \omega_{+,R} \right\rangle$ of the outer ring is very weak and is nearly undetected by THz-TDS only the high-frequency bonding, $\left| \omega_{-,C}^{-} \right\rangle$ and low-frequency antibonding, $\left| \omega_{-,C}^{+} \right\rangle$ plasmons in the coaxial structure are resulted in hybridized resonances.
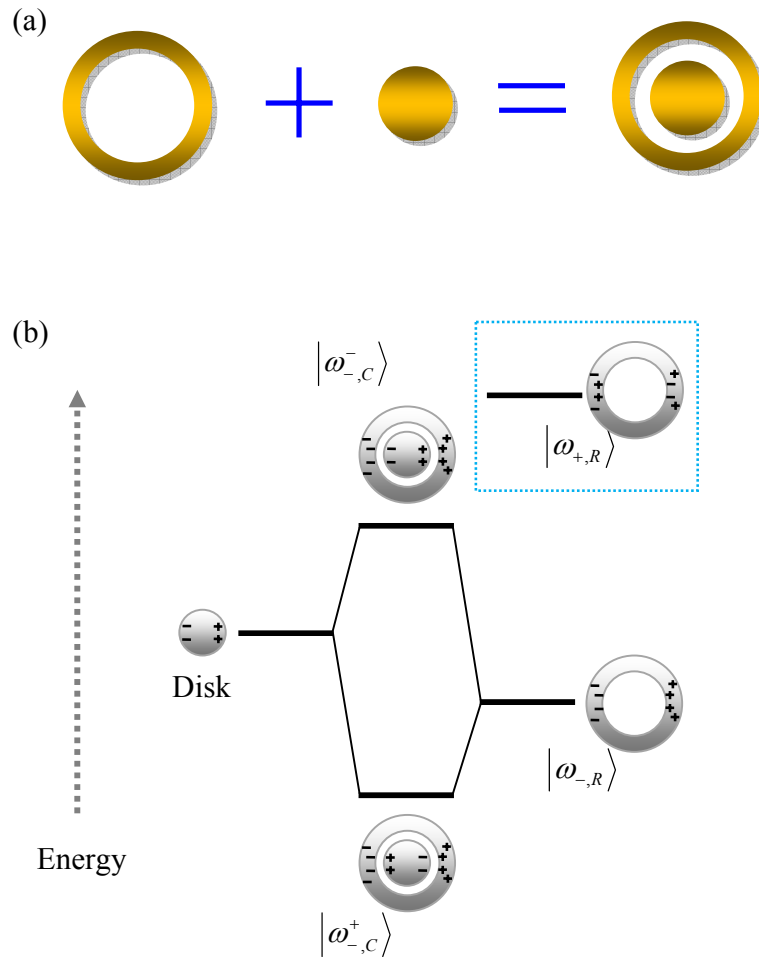
Figure 3-15 (a) Sketch map of plasmon hybridization theory in the coaxial structures. (b) An energy-level diagram depicting the interaction between the outer ring symmetric mode, $|\omega_{-,R}\rangle$ and the inner disk, resulting in hybridized resonances of high-frequency bonding, $|\omega_{-,C}^{-}\rangle$ and low-frequency antibonding, $|\omega_{-,C}^{+}\rangle$ plasmons in the coaxial structure. Inset: the antisymmetric mode, $|\omega_{+,R}\rangle$ of the outer ring. Its contribution is neglected because it is very weak and is nearly undetected by THz-TDS.

3.5.2 Dependence of transmission on the inner disk of the coaxial particles

Figure 3-16(a) illustrates frequency-dependent amplitude transmission of a set of coaxial structures with fixed dimensions in the outer rings and various diameters in the inner disk from 0 to 80 μm. There are two resonances observed, with one being sharp and strong resonance near 0.49 THz, and the other is a broad resonance located at a higher frequency. We choose an outer ring of Φ_{OD} = 100 μm and Φ_{ID} = 90 μm such that it takes no account of the influence of its asymmetric mode, $\left| \omega_{+,R} \right\rangle$ for simplification. According to the plasmon hybridization theory depicted in Section 3.5.1, the interaction between the ring and disk results in two prominent resonances: the low-frequency coaxial antibonding $\left| \omega_{-,C}^{+} \right\rangle$ and the high-frequency coaxial bonding $\left| \omega_{-,C}^{-} \right\rangle$ plasmons. Therefore, the coaxial structure can be approximately described as a simple two-level system. With increasing disk diameter, the strength of the low-frequency resonance becomes weaker and the linewidth being narrower. Meanwhile, the high-frequency resonance is enhanced with a narrower linewidth and both resonances are red-shifted. Also, the high-frequency non-resonant background decreases with increasing metal filling factor as the dimension of the disk increases [14].

Figures 3-16(b) and (c) illustrate the simulated electric field distribution of the coaxial structure with Φ_{D} = 70 μm at both resonances, respectively. The electric field at the low-frequency mode, as shown in Figure 3-16(b), exhibits strong coupling in the gap between the ring and disk and between the adjacent rings. The near-field local electric field in the gap is nearly two times of that in the ring-only array. As for the electric field at the high-

frequency resonance shown in Figure 3-16(c), contributions are mainly drawn from the

DLSPs of the disk and their coupling between the adjacent structures.
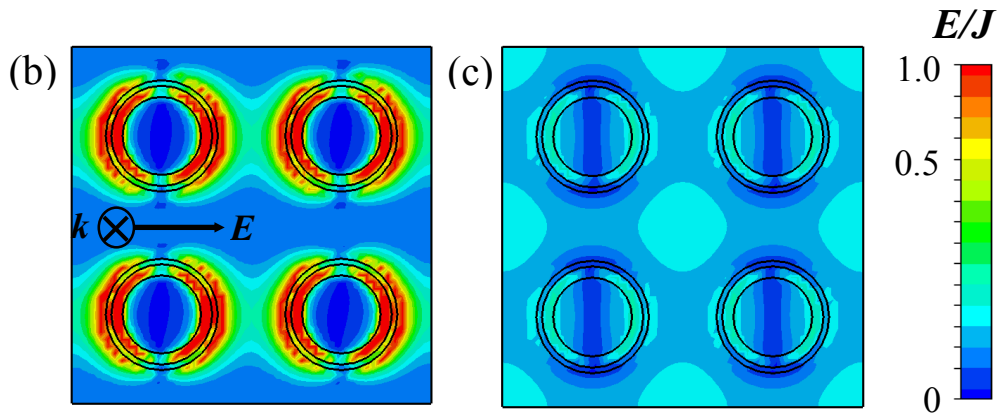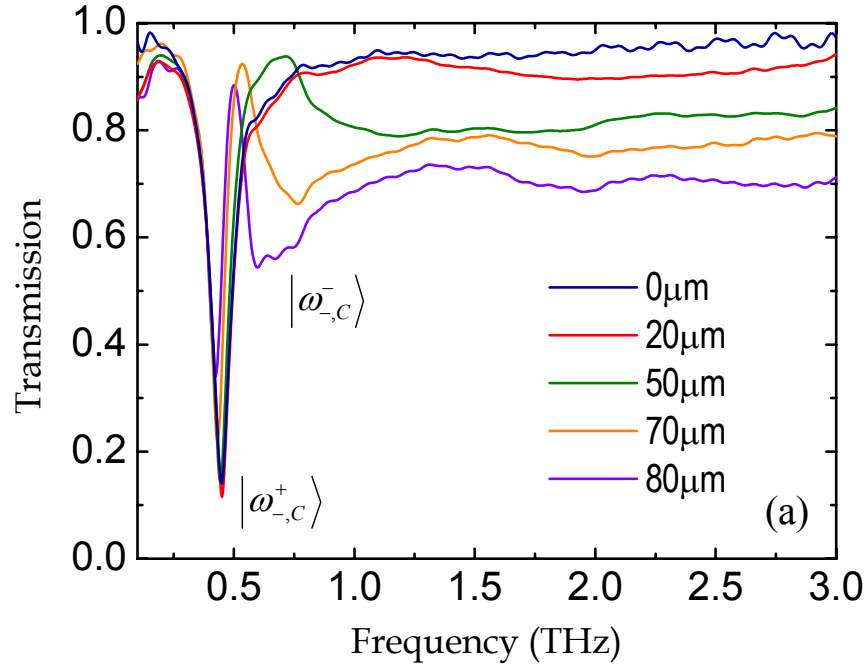
Figure 3-16 (a) Measured frequency-dependent amplitude transmission of the coaxial structures with fixed $\Phi_{OD} = 100$ μm, $\Phi_{ID} = 90$ μm, and various Φ_D. Simulated electric field distributions of (b) low-frequency antibonding resonance at 0.41 THz, and (c) high-frequency bonding resonance at 0.76 THz of the coaxial structure of $\Phi_{OD} = 100$ μm, $\Phi_{ID} = 90$ μm, and $\Phi_D = 70$ μm.

3.5.3 Interactions between the inner disk and outer ring

Based on the gap dimensions between the ring and disk as well as the energy difference between their plasmon modes, such resonant properties are a result of three interaction modes, including strong, weak, and anomalous interactions, as illustrated in Figures 3-17(a)-(c). The strong interaction occurs when the coaxial resonator has a gap size in the range of 3-20 μm. As shown in Figure 3-17(a), with the gap being 5 μm, the energy difference between the coupled resonances is indeed increased compared to that in the ring and disk-only structures. This is consistent with the basic two-level system theory that the coupling increases the separation between the two levels [53]. The inset of Figure 3-17(d) illustrates the measured increase in resonance separation compared to that of the ring and disk-only structures. Clearly, the resonance tunability is not as prominent as that in the visible regime due to relatively weak coupling at terahertz frequencies. When the gap increases to greater than 20 μm, we observe the week interaction where the resonances are getting less to non-affected. In Figure 3-17(b), with a 35 μm gap, the resonances appear nearly identical to the ring and disk-only structures. It is noted that the raised transmission around 2.0 THz is due to spectrum superposition of the ring and the high-frequency resonance of the disk and is not an indication of resonance red-shift.

The resonance coupling strength between the ring and disk is evaluated by use of the Hamiltonian Matrices as depicted in Section 2.5.3 [50]. Considering the uncoupled ring and disk as two unperturbed states with corresponding eigenvalues, E_1 and E_2, respectively, the Hamiltonian can be defined as $\hat{H}_0$. For the hybridized coaxial

resonances with two eigenvalues E_a and E_b, their Hamiltonian can be written as $\hat{H} = \hat{H}_0 + \hat{V}$, where $\hat{V}$ stands for the coupling term. Thus,

$$\hat{H} = \begin{pmatrix} E_a & 0 \\ 0 & E_b \end{pmatrix} = \begin{pmatrix} E_1 & \kappa \\ \kappa^* & E_2 \end{pmatrix} \tag{3-2}$$

where κ and κ^* are the coupling coefficients between E_1 and E_2 and conjugate with each other. The calculated coupling coefficients, $|\kappa|^2$ based on the experimental data are shown in Figure 3-17(d). With the gap between the ring and disk increased greater than 20 μm, a significant reduction in the $|\kappa|^2$ value is revealed, further indicating the occurrence of weak interaction.

The anomalous interaction occurs when the gap between the ring and disk is further reduced to less than 3 μm. With such a small dimension, the charges aggregated along the gap interact so strong that tunnel the gap through and shorted the ring and disk. As shown in Figure 3-17(c), with a gap being 2.5 μm, only one resonance is observed that nearly overlaps with the DLSP resonance of the disk having same Φ_{OD} of the outer ring. This interesting anomalous interaction has not been reported in the visible regime [53,55].
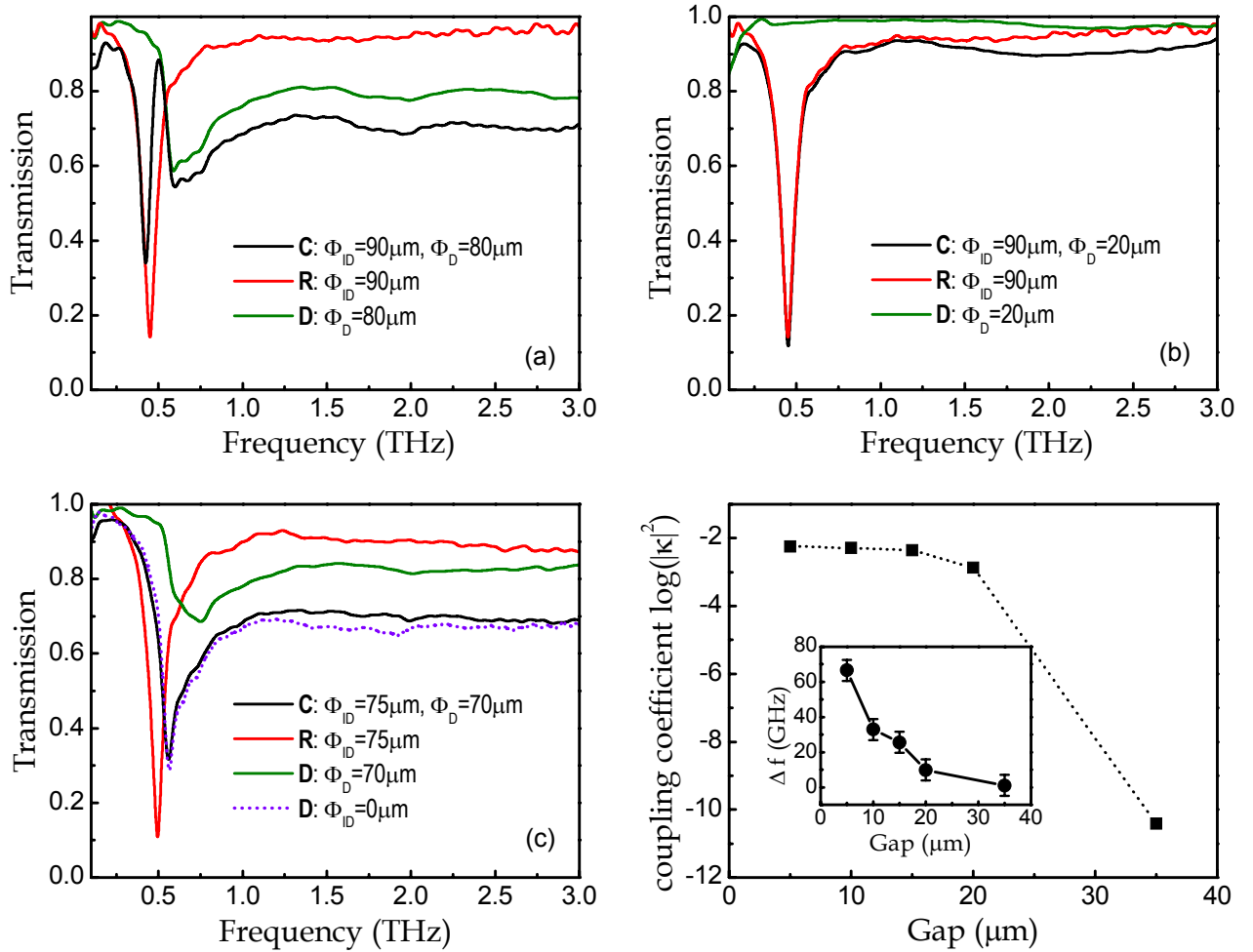
Figure 3-17. Measured transmission of the ring only (R, red), disk only (D, green), and coaxial (C, black) resonators, respectively, with fixed $\Phi_{OD} = 100$ µm for (a) strong interaction, (b) weak interaction, and (c) anomalous interaction. (d) Calculated resonance coupling strength, $\log(|\kappa|^2)$ at various gaps between the ring and disk. Inset: measured increase in resonance separation in the coaxials compared to that of the ring and disk-only structures.

3.6 Conclusion

In conclusion, we present THz-TDS studies of reflection/transmission properties of periodic subwavelength metallic particles. The surrounding substrate, shape, and periodicity are proven to influence the resonance characteristics of the metallic particle arrays. Also, an optimum ring wall dimension is observed with which the symmetric resonance approaches a maximum strength at the ring particle resonance. In the coaxial structures, strong, weak, and anomalous resonance interactions are experimentally observed. The strong and weak interactions are well characterized by the plasmon hybridization theory based on a simple two-level system. The anomalous interaction, however, occurs when the gap between the ring and disk is less than 3 μm and exhibits resonant properties similar to those of a disk of same outer diameter. Such subwavelength structures manifest less frequency tunability and plasmonic coupling strength compared to the nanostructured counterparts at visible frequencies due to significant increase in the values of dielectric function of metals in the terahertz regime. The resonant properties of plasmonic structures are promising in subwavelength terahertz spectroscopy and terahertz biomedical sensing.

CHAPTER IV

COUPLING BETWEEN SUBWAVELENGTH METALLIC HOLES AND

PARTICLES IN COAXIAL STRUCTURES

Based on the enhanced transmission through the periodic hole array, it has been reported that further enhancement can be achieved by employing complex plasmonic structures, such as corrugating metallic periodic grooves surrounding a single hole [56], placing metamaterial structures at the near field of the hole [57,58], or using circular coaxial structures [38,59-65]. In these complex structures, stronger resonant process coupling with incident radiation leads to improved transmission enhancement compared to that in the hole-only array.

4.1 Enhanced transmission through rectangular coaxial hole array

Here, we study the transmission properties of hybrid structures made from rectangular hole-particle coaxial composites. Significant transmission enhancement is observed when compared to the hole-only array counterpart due to coupling between metallic holes and particles in the composite structure. By changing the polarization of incident radiation, isotropically enhanced transmission is also obtained. Based on numerical fitting by the Fano model and angle-resolved transmission measurement, the coupling mechanism for

different structure orientations is analyzed. The high enhanced transmission and frequency shift are the result of coupling between DLSPs of the inner particle, SPs and LSPs of the holes, and the direct scattering.

4.1.1 Effect of the inner particle in coaxial structures

The coaxial hole array, as shown in Figure 4-1, was fabricated using the process described in Section 2.1.
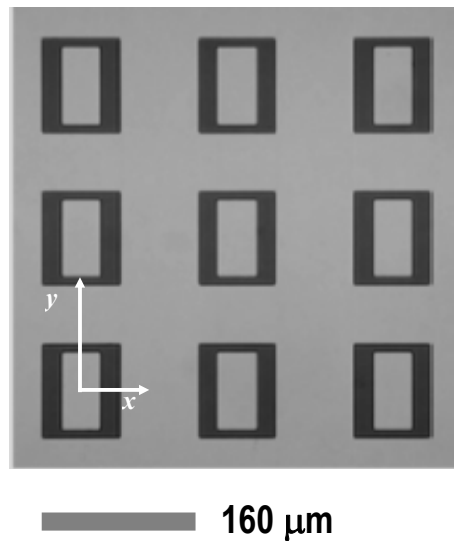
Figure 4-1 Microscopy image of a coaxial hole array with hole dimension of 100×80 μm^2, inner particle dimension of 80×40 μm^2, and a periodicity 160 μm.

In Figure 4-2(a), the amplitude transmission of the coaxial hole arrays with different particle lengths at $E \parallel y$ is measured by THz-TDS. With inner particle length along y axis increased from 60 to 80 μm, the amplitude transmission of the Si-Al SP [±1,0] mode is enhanced from 0.82 to 0.92, and the resonance frequency is red-shifted from 0.55 to 0.46 THz as shown in Figure 4-2(b). Compared to the resonance of the coaxial Si-Al SP [±1,0] modes, the hole-only Si-Al SP [±1,0] mode showed only a 0.47 peak transmission resonating at 0.55 THz. The normalized amplitude transmission, which is defined as the peak transmission normalized by the area of the hole is about 1.5. With the inner particle 80×60 μm^2 integrated in the hole, the normalized amplitude transmission is increased from 1.5 to 6.72, showing more than four times increase than that of the hole-only array. As for the particle-only array, the increased dimension along the electric field leads to a strengthened resonance and frequency red-shift [14]. By increasing the inner particle length along y axis in the composite structure, the coupling between DLSPs of the inner particle, SPs and LSPs of the outer hole becomes stronger, resulting in more enhanced transmission and resonance red-shift compared to the hole-only array.
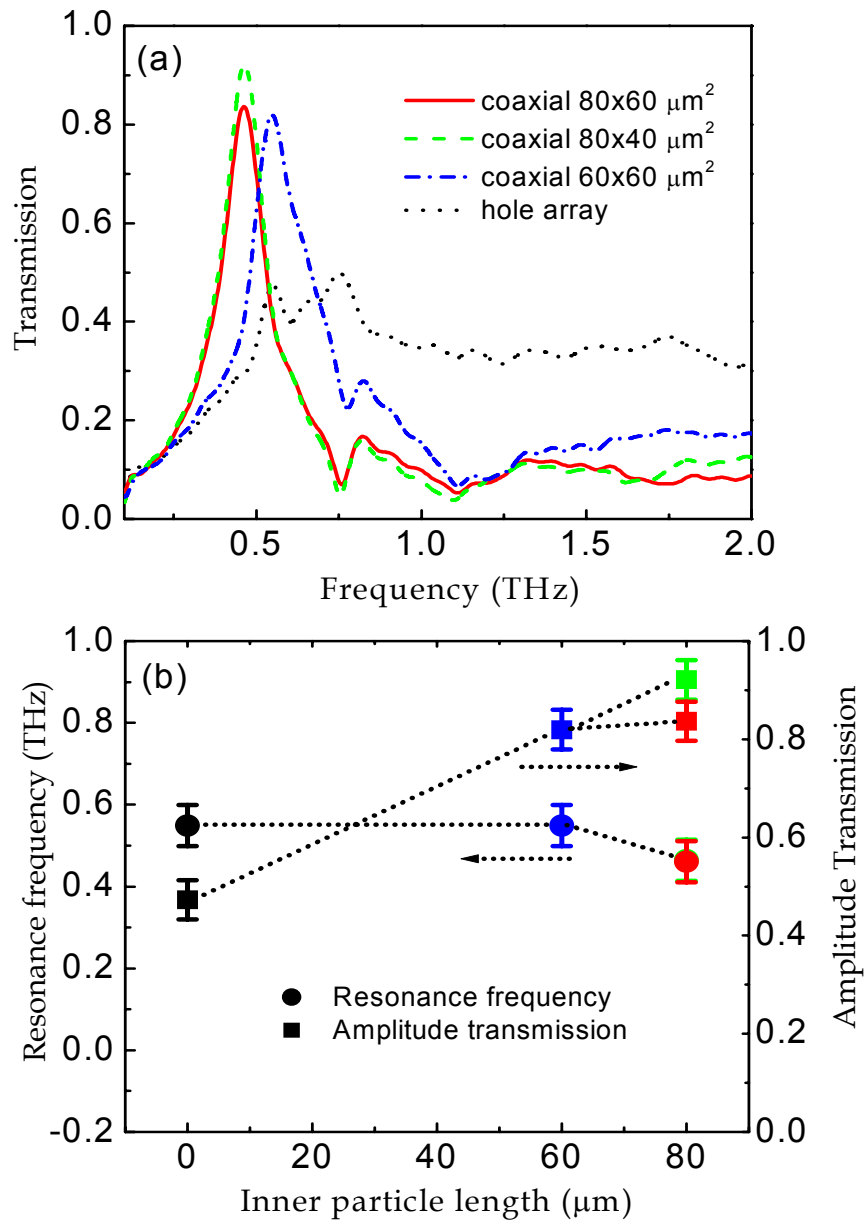
Figure 4-2 (a) Measured frequency-dependent amplitude transmission of hole array (dot curve) and coaxial array with different inner particle dimension of $80 \times 60 \ \mu m^2$ (solid curve), $80 \times 40 \ \mu m^2$ (dash curve), $60 \times 60 \ \mu m^2$ (dash-dotted curve) with $E \parallel y$. The dimension of the holes is fixed as $100 \times 80 \ \mu m^2$, with a periodicity 160 μm. (b) Resonance frequency (circles) and amplitude transmission (squares) as a function of inner particle length. The color corresponds to different inner particle dimensions in fig. 4-2(a). The dotted lines are to guide the eye.

When the inner particle length along the y axis is fixed, the length along the x axis also influences the transmission, while the frequency shift is not observed. The change of length along x axis modifies the direct transmission, and alters the coupling between SPs, LSPs and direct transmission. As a result, the enhanced transmission of the coaxial array is attributed to the coupling between DLSPs of the inner particles, SPs, LSPs of the outer holes, and direct scattering. In addition, the non-resonant background at higher frequencies of the coaxial array is much lower than that of the hole-only array, leading to the increase in resonance contrast. Moreover, a weaker resonance is observed around 0.82 THz in the coaxial arrays, which is induced by coupling with the Si-Al SP [±1,±1] mode.

4.1.2 Effect of the structure orientation

Figure 4-3(a) shows the enhanced transmission spectra at $E \parallel x$, with various lengths of the shorter side of the inner particle from 40 to 60 μm. For the hole-only array, we observe a higher amplitude transmission 0.85 at $E \parallel x$ than that of $E \parallel y$. For the coaxials, when the shorter length of the particle is 40 μm, the DLSPs of the particle is too weak to induce a strong coupling with SPs. Thus, the transmission spectrum of the coaxial array is similar to that of the hole-only array. With increasing shorter length to 60 μm, however, the enhanced DLSPs of the inner particle couple with SPs, leading to an extraordinary enhanced transmission of 0.99, as shown in Figure 4-3(b). As for the coaxial array with inner particle 80×60 μm^2, the normalized amplitude transmission approaches 7.04 at 0.47 THz, which is almost three times higher than that of the hole-only array of 2.72 resonating at 0.51 THz.
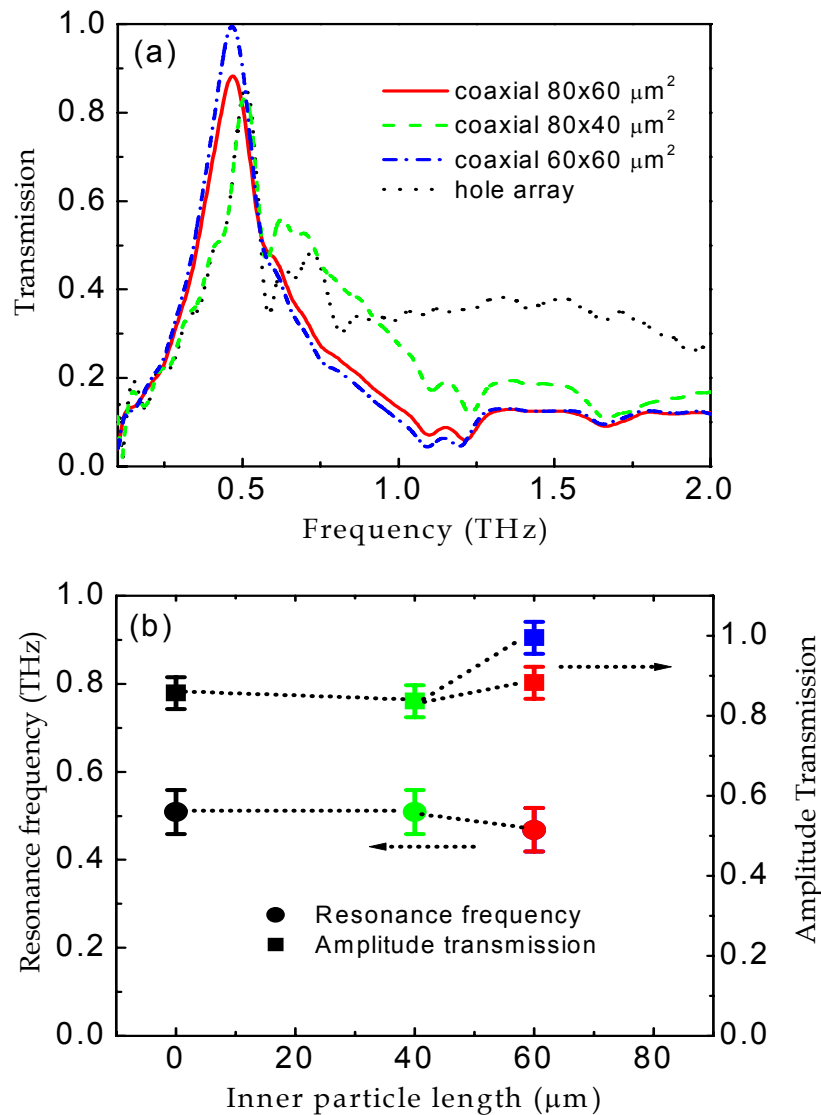
Figure 4-3 (a) Measured frequency-dependent amplitude transmission of hole array (dot curve) and coaxial array with different inner particle dimension of $80 \times 60 \ \mu m^2$ (solid curve), $80 \times 40 \ \mu m^2$ (dash curve), $60 \times 60 \ \mu m^2$ (dash-dotted curve) with $E \parallel x$. Dimension of holes is fixed as $100 \times 80 \ \mu m^2$, periodicity is 160 μm. (b) Resonance frequency (circles) and amplitude transmission (squares) as a function of the inner particle length. The color corresponds to different inner particle dimensions in (a). The dotted lines are to guide the eye.

When the dimension of the inner particle is 60×60 μm^2, the orientation of the electric field will not influence the DLSPs of the particle, the SPs excited by the 100×80 μm^2 outer holes, however, altered the transmission properties a lot. If one compares between Figures 4-2 and 4-3 with the sample orientation switched from $E \parallel y$ to $E \parallel x$, it is seen that the amplitude transmission increases from 0.82 to 0.99 and the resonant frequency red-shifts simultaneously, which manifest that SPs of the holes also influence the transmission characteristics of the coaxial array.

4.1.3 Dependence on incident angle

Angle-resolved transmission spectra of the coaxial structure with an 80×40 μm^2 inner particle at $E \parallel y$, are measured under TM polarization. As shown in Figure 4-4, two resonance modes are observed in the spectra. By changing the incident angle, a strong Si-Al SP [±1,0] mode at 0.46 THz exhibits angle-independent behavior. A weak Si-Al SP [±1,±1] mode near 0.8 THz, however, experiences frequency shift as well as mode splitting when the incident angle is greater than 10 degrees. Due to the electric dipole characteristics, the DLSP resonance couples with the Si-Al SP [±1,0] mode stronger than that with the Si-Al SP [±1,±1] mode; this results in the angle-independent enhanced transmission centered at 0.46 THz.
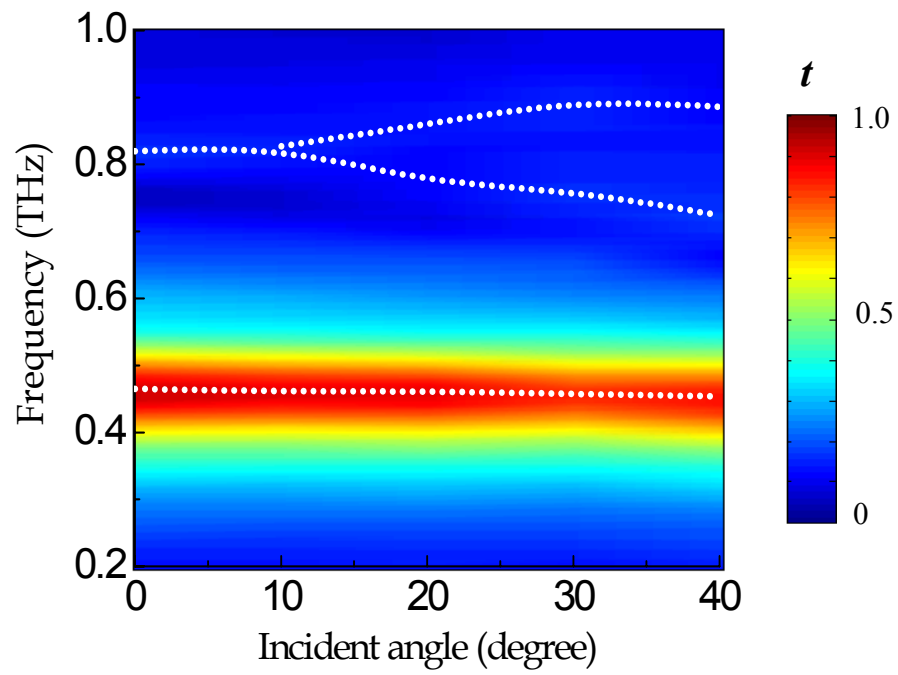
Figure 4-4 Measured angle-resolved transmission for coaxial array with inner particle 80 × 40 μm², periodicity 160 μm and $E \parallel y$ for TM polarization. The dots manifest resonance modes.

4.1.4 The Fano model

Due to the asymmetric line shape of the resonance profiles of the coaxial structures, the measured transmittance can be analyzed by the Fano model, which describes the interactions between direct scattering and discrete states coupled by DLSPs, SPs, as well as LSPs of the holes. The Fano line shape, which includes the higher order SP modes, is expressed as [38]

$$T_{Fano} = T_a + T_b \left(1 + \sum_v \frac{q_v}{\Delta\varepsilon_v}\right)^2 \bigg/ \left[1 + \left(\sum_v \frac{1}{\Delta\varepsilon_v}\right)^2\right] \qquad (4\text{-}1)$$

where $\Delta\varepsilon_v = (\omega - \omega_v)/(\Gamma_v/2)$, T_a is a slowly varing transmittance, T_b is the non-resonant transmission coefficient that couples with discrete resonance states, $\omega_v/2\pi$ is the resonance state frequency, $\Gamma_v/2\pi$ is the linewidth, and q_v is the Breit-Wigner-Fano coupling coefficient for the vth discrete state [13,37,38]. As shown in Figure 4-5, the Fano model shows an excellent fit to the measure resonance spectrum of the coaxial array with an $80 \times 40 \ \mu m^2$ inner particle at $E \parallel y$.
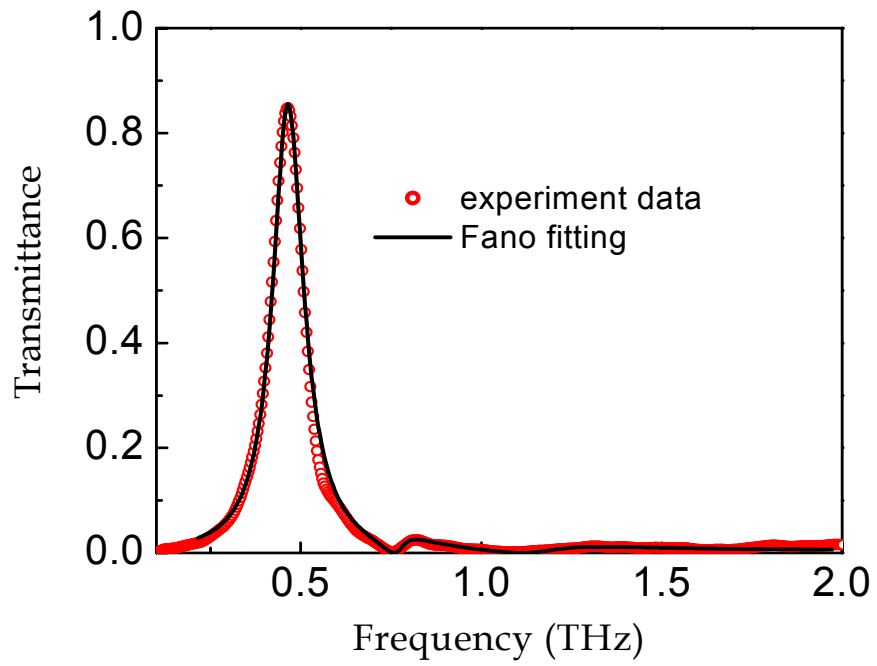
Figure 4-5 (a) Measured (circles) and Fano fitted (solid curve) transmittance of the coaxial array with an inner particle $80 \times 40~\mu m^2$, periodicity 160 μm and $E \parallel y$. The fitting parameters are $T_a = 0$; $T_b = 0.0013$; $q_1 = 24.5$; $\Gamma_1/2\pi = 0.11$; $\omega_1/2\pi = 0.4485$; $q_2 = 1.35$; $\Gamma_2/2\pi = 0.07$; $\omega_2/2\pi = 0.7680$; $q_3 = 1.8323$; $\Gamma_3/2\pi = 0.25$; and $\omega_3/2\pi = 1.1852$.

4.1.5 Coupling coefficient

In order to understand the coupling mechanism of the coaxial arrays, a complex Hamiltonian [38], $\hat{H} = \hat{H}_1 + \hat{H}_2 + \hat{H}_3 + \hat{V}$, is defined. The eigenmodes of $\hat{H}_1$ corresponds to the resonant state, i.e. DLSPs of the inner particle, $\hat{H}_2$ stands for the Al-Si SP $[\pm 1,0]$ mode of the outer hole, $\hat{H}_3$ is the LSPs of the hole and the direct scattering. The three channels are coupled via the coupling term $\hat{V}$. Thus, the effective eigenmode matrix can be written as

$$
\begin{pmatrix} \omega_a & 0 & 0 \\ 0 & \omega_b & 0 \\ 0 & 0 & \omega_c \end{pmatrix} = diag \begin{pmatrix} \omega_1 & \kappa_{12} & \kappa_{13} \\ \kappa^*_{12} & \omega_2 & \kappa_{23} \\ \kappa^*_{13} & \kappa^*_{23} & \omega_3 \end{pmatrix} \tag{4-2}
$$

where $\omega_{a,b,c}$ are the measured resonant states of the coaxial structures, $\omega_1/2\pi$ is the DLSP mode, which can be calculated by $\omega_1/2\pi = (c/2L)\varepsilon_d^{-1/2}$ with L being the length of the particle parallel to the polarization of the incident electric field, ε_d is the dielectric constant of the substrate [14]. $\omega_2/2\pi$ is the SPs mode of hole array, which can be given approximately at terahertz frequencies as [38].

$$
\sqrt{\left(\frac{(\omega_2/2\pi)\sin\theta}{c} + \frac{m}{P}\right)^2 + \left(\frac{n}{P}\right)^2} = \frac{(\omega_2/2\pi)\varepsilon_d^{1/2}}{c} \tag{4-3}
$$

where m, n are integer mode indices, P is periodicity, and θ is incident angle. $\omega_3/2\pi$ is the LSP mode of the hole and the direct scattering as well, κ_{12}, κ_{13} and κ_{23} are coupling coefficients among the three resonant states. $\kappa_{12}*$, $\kappa_{13}*$, and $\kappa_{23}*$ are the conjugates of κ_{12}, κ_{13}, and κ_{23}.

117

For each incident angle, we have

$$(\omega - \omega_1)(\omega - \omega_2)(\omega - \omega_3) + \kappa_{12}\kappa_{23}\kappa_{13}* + \kappa_{12}*\kappa_{23}*\kappa_{13}$$
$$- |\kappa_{13}|^2(\omega - \omega_2) - |\kappa_{23}|^2(\omega - \omega_1) - |\kappa_{12}|^2(\omega - \omega_3) = 0, \qquad (4\text{-}4)$$

where ω corresponds to $\omega_{a,b,c}$, as the coupled state of SP, LSP, and DLSP degenerate to one state, $\omega_a = \omega_b = \omega_c$. The variables, i.e. ω_3, κ_{12}, κ_{13}, and κ_{23} are obtained by Equation (4-4) using the angle-resolved transmission data in Fig. 4-4.

Based on the angle-dependent transmission of the coaxial array with an 80×40 µm² inner particle and periodicity 160 µm, the coupling coefficient is calculated. At $E \parallel x$, the calculated results are $|\kappa_{12}| = 8.03 \times 10^{-3}$, $|\kappa_{13}| = 0.103$, and $|\kappa_{23}| = 9.70 \times 10^{-3}$, indicating that the coupling between DLSPs and LSPs primarily contributes to the field enhancement, which further explains the angel-independent behavior of the Al-Si [±1,0] mode observed in Fig. 4-4. This behavior is also evidenced from the computed electric field distribution of the coaxials, as illustrated in Fig. 4-6(a), where strong field enhancement is observed in the particle and the open area of the coaxial. At $E \parallel y$, the calculated coefficients are $|\kappa_{12}| = 0.151$, $|\kappa_{13}| = 5.00 \times 10^{-4}$, and $|\kappa_{23}| = 2.35 \times 10^{-2}$, manifesting the dominant role of the coupling between DLSPs and SPs. This is also consistent with the electric field distribution shown in Fig. 4-6(c), in particular, the electric field along the surface of metal in the vicinity of the coaxials is much enhanced than that at $E \parallel x$.

4.1.6 Electric field simulation

As shown in Figure 4-6, the electric field distributions of the coaxial array with an inner particle 80×40 μm^2 and periodicity 160 μm and hole-only array is simulated by CST Microwave Studio Software, respectively. With $E \parallel y$, as shown in Figures 4-6(a) and (b), a strong coupling between LSPs and SPs is revealed in the hole-only array. In the coaxial array, however, intensified electric field is distributed at the gap between the inner particle and the hole along the incident electric field due to coupling between DLSPs and LSPs. Also, weak electric field is shown along the surface of the coaxial array which manifests a weak coupling between SPs and LSPs. Figures 4-6(c) and (d) illustrate the electric field distributions of the coaxial and hole-only arrays with $E \parallel x$. Coupling between LSPs and SPs in the hole-only arrays is similar to that of $E \parallel y$ except that stronger LSPs resonance is presented at the edge of the holes due to the change of hole orientation. As a result, stronger coupling between LSPs and SPs is induced. Similarly, strong coupling between SPs and LSPs is shown along the surface of the coaxial array, confirming their dominant contribution to the transmission resonance.
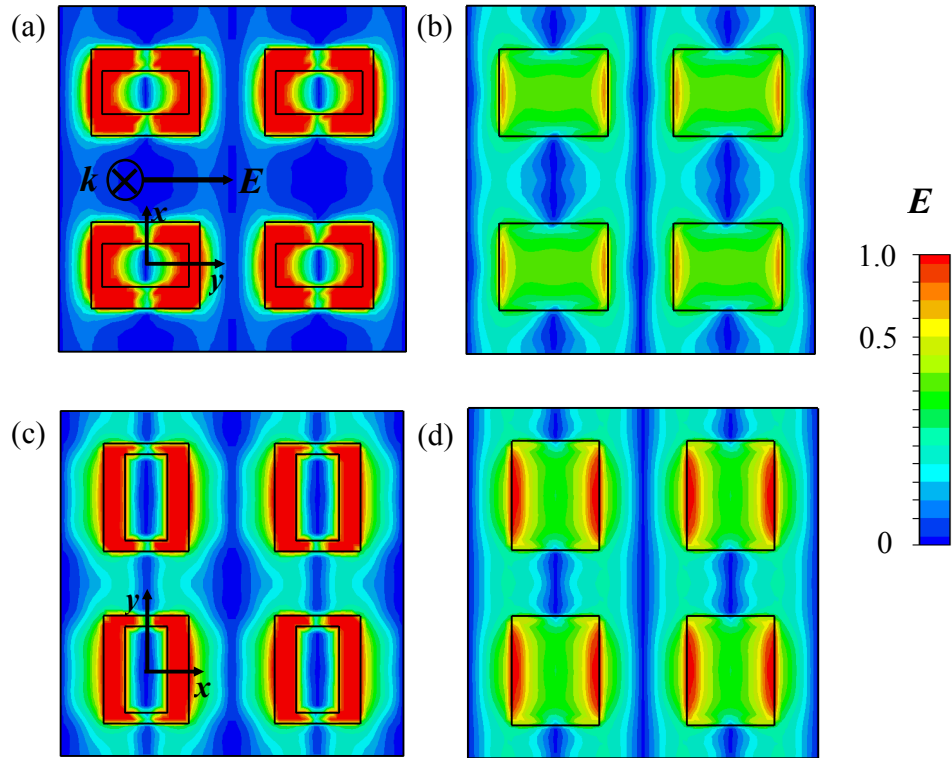
Figure 4-6 Simulated electric field distributions of the coaxial array with an $80 \times 40 \ \mu m^2$ inner particle and periodicity 160 μm, (a) $E \parallel y$, resonating at 0.48 THz, (c) $E \parallel x$, resonating at 0.51 THz, and hole-only array (b) $E \parallel y$, resonating at 0.54 THz, (d) $E \parallel x$, resonating at 0.51 THz. The dimension of holes is fixed as $100 \times 80 \ \mu m^2$ and periodicity 160 μm.

4.2 Enhanced transmission through array of rectangular holes hybridized with ring shape particle

It was proved that the hybridized structures of holes and solid particles array can produce more enhanced transmission than that of the hole-only array [39,51,62,63,65]. Also, compared to the solid particles, the ring shape particles exhibit larger frequency tunability and stronger electric field enhancement [15]. It thus is intriguing to investigate the resonant properties of the hybridized structures of hole and ring particles.

The hybridized coaxial structures are fabricated by conventional lithography and metallization processes on a silicon substrate (0.64 mm thick, n-type resistivity ρ = 12 Ω cm), as shown in Figure 4-7.
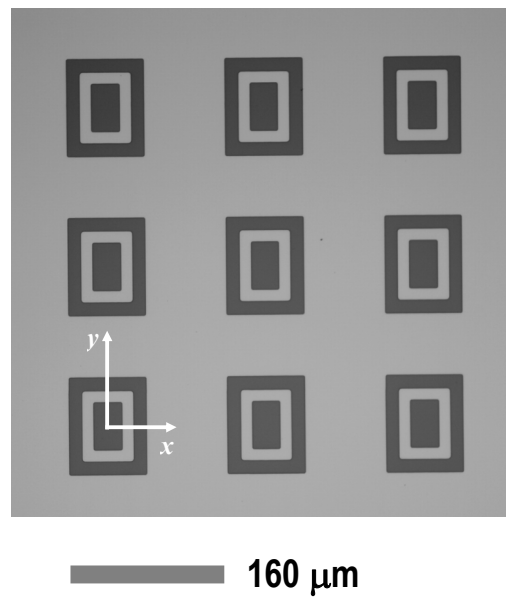
Figure 4-7 Microscopy image of a hole-ring coaxial array with hole dimension of 100 × 80 μm², inner ring dimension of 80 × 60 / 60 × 40 μm², and a periodicity 160 μm.

4.2.1 Transmission comparison between the hybridized coaxial and the hole-only array

Figure 4-8(a) shows the frequency-dependent amplitude transmissions of the hole arrays hybridized either with solid particles or ring particles, and the counterpart hole-only array as well. Compared to the hole-only array, the hole-rectangle coaxials manifest nearly two times of amplitude transmission as well as more than four times of normalized amplitude transmission, as shown in Figure 4-8(b). As discussed in Chap. 4.1.5, such significant increase is due to the coupling between the resonance of holes and DLSPs of the particles [15]. Although the ring particle exhibits stronger DLSP resonance than the solid particle array because of the additional DLSP resonance of inner edge [15], the hole-ring coaxials, however, show the diminished amplitude transmission of 0.76 compared to 0.84 of the hole-rectangle coaxials. The outer edge of ring particle couples with the holes, leading to enhanced transmission. The inner edge, however, retains the transmission minimum of DLSP resonance, thus diminishing the enhanced transmission. Also, by coupling with the hole array, the hole-ring coaxials show a further red-shifted resonance frequency. As a result, the transmission of hole-ring coaxials is determined by both coupling effects between hole and ring particle outer edge and DLSP resonance of the inner edge.
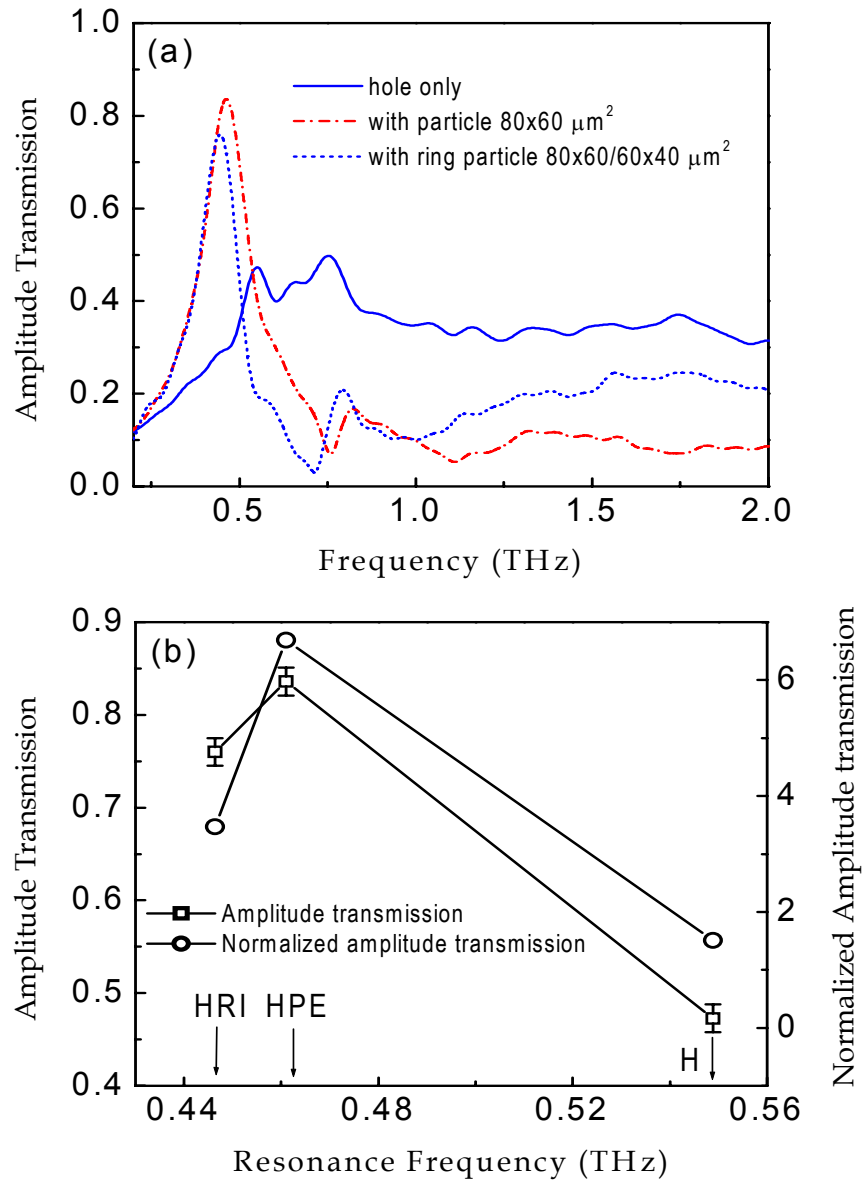
Figure 4-8 (a) Measured frequency-dependent spectra of hybridized structures with 80 × 60 μm² solid particles (dash-dotted curve), 80 × 60 / 60 × 40 μm² ring particles (dotted curve), and the hole-only counterpart (solid curve), with periodicity 160 μm and $E \parallel y$, the holes are fixed as 100 × 80 μm². (b) Amplitude transmission (squares) and normalized amplitude transmission (circles) of the hole-rectangle coaxials (HRE), hole-ring coaxial (HRI), and the hole-only counterpart (H).

4.2.2 Dependence of transmission properties on dimensions of the inner particles

When the hole dimension is fixed as $80 \times 100 \ \mu m^2$, the dimension of the ring particles is observed to alter the transmission characteristics of hybridized coaxial structures. The inset of Figure 4-9(a) shows the transmission properties of the ring only array by fixing the outer dimension as $80 \times 60 \ \mu m^2$ and inner length as $60 \ \mu m$. With $E \ || \ x$ (short axis) which is shown in Figure 4-7 and the inner width along E field increases from 20 to 40 μm, the transmission minimum decreases and the resonance frequency exhibits a red-shift. The electric dipole moment of the ring particle is modified by the inner width along E field, leading to the alteration of the DLSP resonance. Figure 4-9(a) shows the transmission properties of the coaxial structure with the same ring particles integrated in the holes with $E \ || \ x$. When the inner width along E field increases from 20 to 40 μm, the amplitude transmission decreases from 0.85 to 0.82, and the resonance frequency experiences a little red-shift. The similar resonance properties between the ring-only structure and their coaxial conterpart manifest that the resonance difference with changing inner width of the rings mainly due to the electric DLSP resonance of rings.
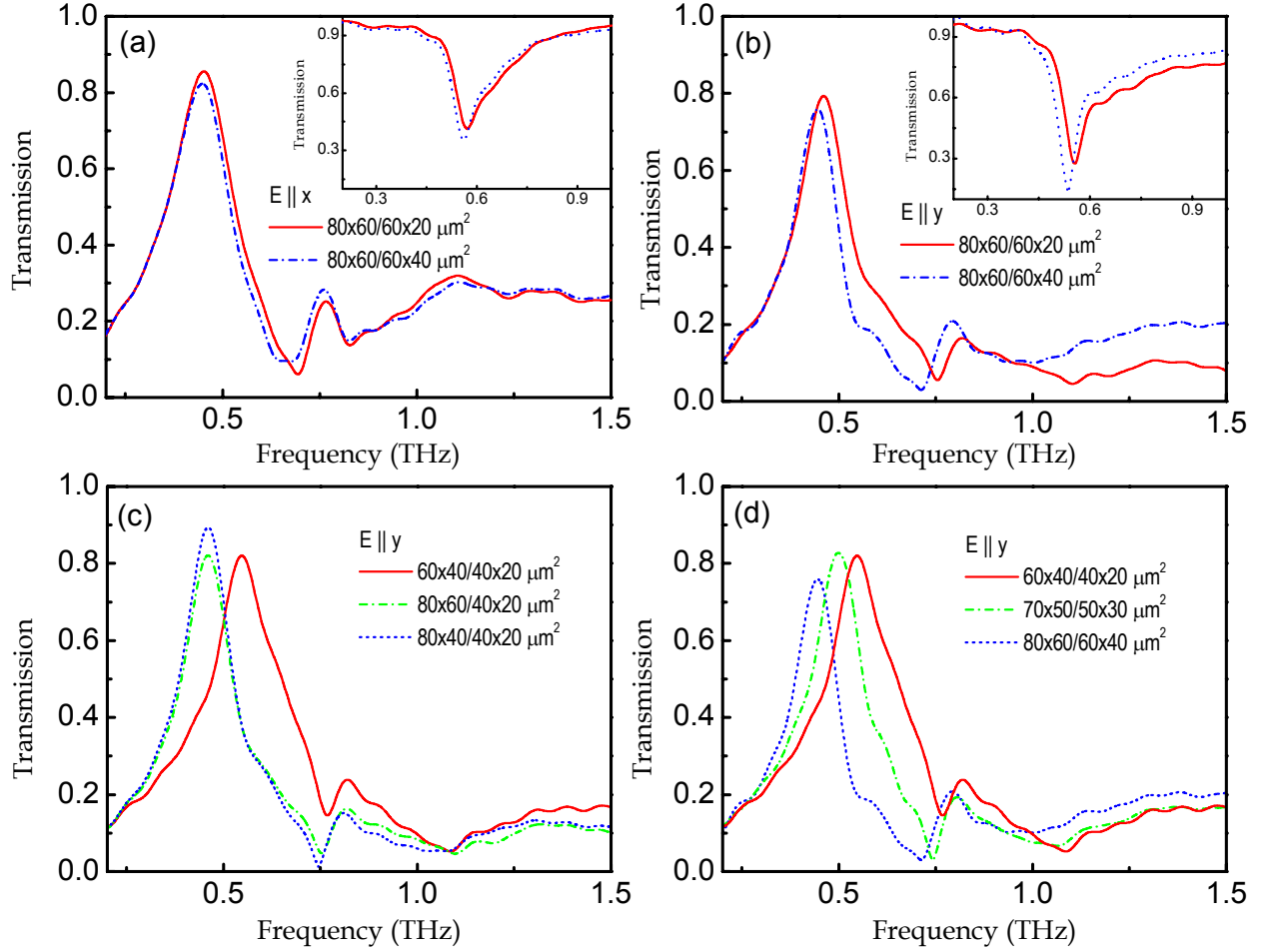
Figure 4-9 Peak amplitude transmission as a function of the dimension of ring particle, the holes are fixed as $100 \times 80 \ \mu m^2$ with periodicity 160 μm. Fix the outer dimension as $80 \times 60 \ \mu m^2$, inner dimension is 60×20 (solid curve) and $60 \times 40 \ \mu m^2$ (dash dotted curve), respectively. (a) $E \parallel x$. (b) $E \parallel y$. Inset: peak amplitude transmission of ring particles only array. (c) Fix the inner dimension as $40 \times 20 \ \mu m^2$, outer dimensions are 60×40 (solid curve), 80×60 (dash dotted curve), and $80 \times 40 \ \mu m^2$ (dotted curve) respectively, with $E \parallel y$. (d) Fix the ring width as 10 μm, the dimension of ring particles are $60 \times 40 / 40 \times 20 \ \mu m^2$ (solid curve), $70 \times 50 / 50 \times 30 \ \mu m^2$ (dash dotted curve), and $80 \times 60 / 60 \times 40 \ \mu m^2$ (dotted curve), respectively, with $E \parallel y$.

With $E \parallel y$, when the inner dimension perpendicular to E field is altered from 20 to 40 μm, the resonance possesses a decreased amplitude transmission and red-shifted frequency, showing similar phenomena as those of inner dimension parallel to E field, as shown in Figure 4-9(b). Beneath the similar phenomena, different resonance principle is revealed with alteration of the inner dimension perpendicular to E field. Even the single hole, which eliminates the SP resonance has enhanced transmission, due to its LSP [29-31]. The LSP resonance is referred to the magnetic dipole moment resonance which is related to the dimension perpendicular to the E field. In the inset of Figure 4-9(b), when the inner dimension of the ring-only array is increased from 20 to 40 μm perpendicular to E field, it enhances the magnetic dipole moment and therefore strengthens DLSP resonance of the ring particle, leading to an increased transmission minimum and red-shifted frequency. By altering the inner dimension of the ring perpendicular to E field, the transmission is found to be attributed to the magnetic resonance of the inner edge of the ring particle.

By fixing the inner edge, the outer dimension of the rings also modify the resonance of the coaxial structures. In Figure 4-9(c), the inner dimension of ring particle is fixed as 40 × 20 μm^2, the outer dimension along E field increase from 60 to 80 μm, the resonance frequency experiences red-shift from 0.55 to 0.46 THz. The frequency shift manifests the change of coupling strength due to the alteration of the gap between the ring and the hole. One the other hand, with the outer edge along E field fixed to 80 μm, the dimension perpendicular to E field set to 60 and 40 μm, respectively, the amplitude transmission increases from 0.82 to 0.89, and no resonance frequency shift is observed. This indicates

that the coupling between the hole and ring particles is invariable, the change of direct scattering makes the variety of the amplitude transmission [51].

Then, changing both the inner and outer edge of the ring particle so that it has a width of 10 μm, the transmission spectra of the resulted coaxials 80 × 60 / 60 × 40 μm^2, 70 × 50 / 50 × 30 μm^2, and 60 × 40 / 40 × 20 μm^2 (outer / inner dimension) are shown in Figure 4-9(d). The resonance frequencies exhibit red-shift with increased overall ring dimensions. The maximum amplitude transmission 0.83, however, is observed with a ring sized 70 × 50 / 50 × 30 μm^2. The resonance frequency is dominated by the coupling effect between the hole and ring particles. The gap between hole and ring is smaller, the coupling between them is stronger. Besides, the DLSP resonance of ring inner edge shows a negative effect on the amplitude transmission, i.e. it diminishes. As a result, the optimum amplitude transmission is due to the contribution from both the coupling between the hole and ring particles and the DLSP resonance of ring inner edge.

4.2.3 Coupling coefficient

In order to understand the coupling mechanism of the hole and ring particles, we introduce the Hamiltonian, $\hat{H} = \hat{H}_1 + \hat{H}_2 + \hat{V}$, where the eigenstates $\hat{H}_1$ and $\hat{H}_2$ stand for the DLSP resonance of the ring particles and the lowest order resonance of the periodic hole array, respectively, and $\hat{V}$ is the coupling term between these eigenstates represented by coupling coefficients κ_{12}. The corresponding eigen frequencies, $\omega_1/2\pi$ and $\omega_2/2\pi$ are the frequencies of the ring DLSPs and lowest order resonance of the hole

array, respectively, given by their measured data. The coupling coefficient κ_{12} can be obtained by solving the Hamiltonian Matrix. The calculated κ_{12} with various ring dimensions is shown in Fig. 4-10. The gap between the hole and ring dominates the direct coupling between them. By changing the outer dimension of the ring particle, the coupling strength changes a lot. The inner dimension of the ring particle, however, also influences the coupling strength but with a small quantity due to the alteration of induced charges distributed along the outer edge of the ring.
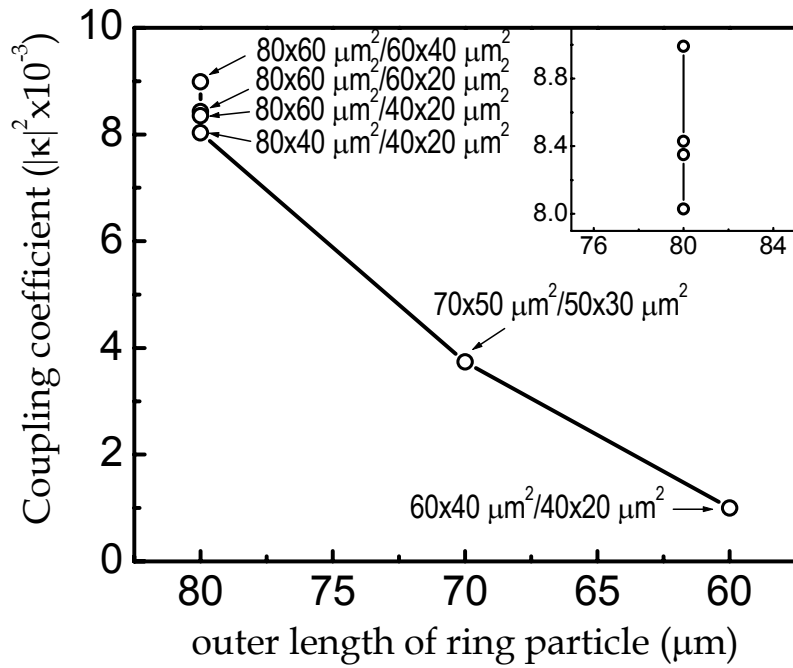
Figure 4-10 Calculated coupling coefficient as a function of different ring particle dimension, $E \parallel y$. Inset: the zoom out of the coupling coefficient with a fixed outer length of ring particle at 80 μm.

4.2.4 Electric field simulation

The field distribution of the hole-ring coaxials is simulated, as shown in Figure 4-11. By setting the ring particle dimensions as $80 \times 60 / 60 \times 40 \ \mu m^2$ and $60 \times 40 / 40 \times 20 \ \mu m^2$, the ring width is fixed at 10 μm. Both the electric and magnetic field distributions of the coaxial structures are illustrated. The electric field is mainly distributed within the gap along the E field, as shown in Figures 4-11(a) and (b). The larger gap possesses stronger electric field due to the coupling effect between resonance and direct scattering [14]. The magnetic field indicated in Figures 4-11(c) and (d) manifests that the magnetic response is distributed within the inner hole of the ring as well as along the gap perpendicular to E field. With larger dimension of inner hole perpendicular to E field, the magnetic field is strengthened within the inner hole area. Meanwhile, stronger magnetic field is distributed along corresponding smaller gap due to the intensified coupling effect. As a result, both the electric and magnetic responses dominate the coupling between the hole and ring particles.
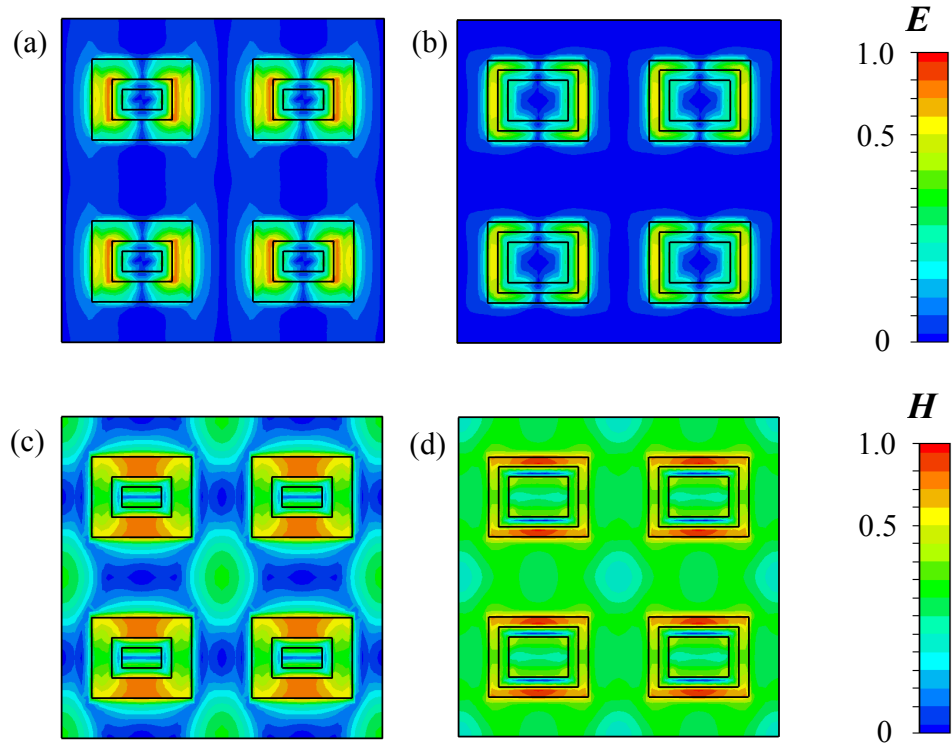
Figure 4-11 Simulated electric and magnetic field distributions of the coaxial structures with different ring particles. The holes are fixed at 100×80 μm^2 with periodicity 160 μm and $E \parallel y$. (a) Electric field distribution, (c) magnetic field distribution of the rings with $60 \times 40 / 40 \times 20$ μm^2 resonating at 0.54 THz. (b) Electric field distribution, (d) magnetic field distribution of the rings with $80 \times 60 / 60 \times 40$ μm^2 resonating at 0.45 THz.

4.3 Conclusion

The enhanced terahertz transmission through the array of various rectangular coaxial structures is investigated. Being hybridized with solid particles, the normalized peak amplitude transmission of the hole-rectangle coaxial structures approaches more than four times higher than that in the hole-only array counterpart. Meanwhile, the resonance can be adjusted by the gap between the solid particle and hole. Being hybridized with the ring shape particles, the resonance of the hole-ring coaxial structures also can be modified by the dimension of the rings. Such transmission resonance is characterized by the coupling between DLSPs, SPs, LSPs and direct scattering. This is confirmed by numerical analysis using the Fano model and electric field simulation. The enhanced transmission of the coaxial structures is promising in subwavelength terahertz spectroscopy and biomedical sensing.

CHAPTER V

MULTILAYER PLASMONIC STRUCTURES

We have studied the enhanced transmission through single layer perforated periodic metallic subwavelength hole array in details. The multilayer subwavelength metallic structures can also introduce the resonance and bring both of the enhanced local field and the enhanced transmission which can be applied in sensors and absorbers. Researchers have shown that the unpatterned planar metallic film with closely coupled periodic subwavelength structures that have a surface modulation to the planar metallic film can excites SP-like resonance [66-68]. Meanwhile, two layers of coupled periodic subwavelength structures can introduce extraordinary transmission. Two types of coupled layer structures are investigated: one is the structures with two layers of the same structures which is due to the coupling between the same patterns [69]; the other structure is composed by two layers of complementary patterns, whose resonance is explained as Fabry-Pérot resonance [70]. In this Chapter, we will focus on the multilayer structures with complementary patterns. Compared to the structures characterized in Section IV, which is comprised of holes and inner particles in one plane regarded as in-plane coupling between SPs, LSPs and DLSPs, the multilayer structure that separate two complementary pattern, i.e. holes and particles, by a dielectric spacer is designed and the out-plane coupling between SPs, LSPs and DLSPs is investigated.

5.1 Sample fabrication

The schematic structure of the multilayer sample is shown in Figure 5-1. At first, one layer of 200 nm thickness aluminum hole array is fabricated on the Si substrate by traditional photolithography. Then, 4 μm thickness dielectric particles (positive photoresist PRA-4000) functioned as dielectric spacer between complementary structures are coated on the hole area by using the alignment technique. After evaporating another layer of 200 nm aluminum on the rugged surface, the multilayer complementary sample is obtained. The dimension of hole array is $100 \times 80 \ \mu m^2$ with 160 μm periodicity.
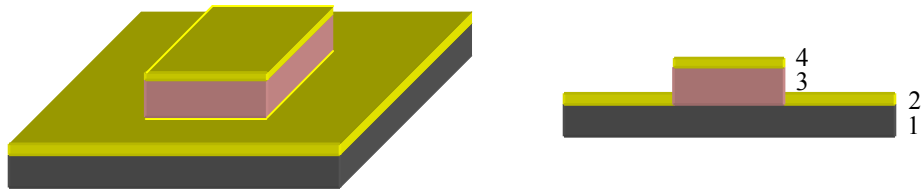
Figure 5-1 Schematic view of multilayer complementary structure. 1. Si substrate; 2. Aluminum hole array; 3. Dielectric spacer; 4. Aluminum particle.

5.2 Dependence of orientation on complementary structure

The measured transmission spectra of the complementary structure are shown in Figure 5-2. Theoretically, very little direct scattering can penetrate the 3D complementary structure unless the light diffracting through the sample from the side faces of the 3D structure. Surprisingly, Enhanced amplitude transmission is observed. With $E \parallel y$, the amplitude transmission approaches 0.71 resonating at 0.54 THz. With $E \parallel x$, the amplitude transmission increase to 0.76 with resonant frequency red-shift to 0.48 THz. Meanwhile, the secondary resonances located at 0.6 THz with $E \parallel x$ and 0.82 THz with $E \parallel y$ manifest the influence by SP [± 1, ± 1] mode. Low background transmission around 0.1 exhibits the low value of direct scattering through the structure. Compared to the large transmission discrepancy of hole-only array, the complementary structure manifests similar amplitude transmission without dependence on the structure orientation.
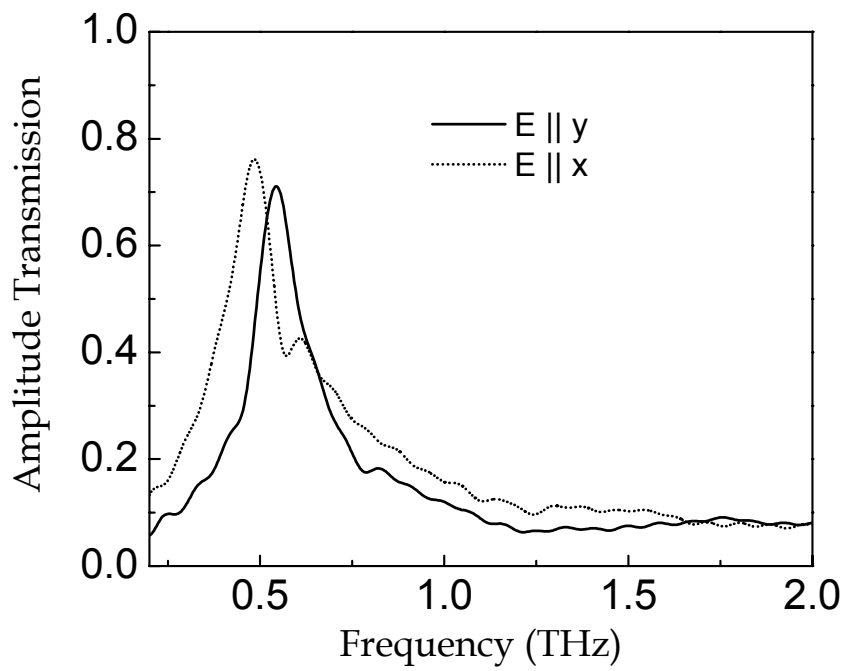
Figure 5-2 Measured transmission spectra of complementary structure with $E \parallel x$ (dotted curve) and $E \parallel y$ (solid curve), respectively.

5.3 Dependence on incident polarization and angle of the complementary structure

In order to investigate the resonance properties of the complementary structure, we measured the angle-dependent transmission spectra with TM and TE incidence polarization, respectively, as shown in Figure 5-3. With TM polarization incidence, $E \parallel y$, an angle-independent resonance at 0.54 THz is observed with incident angle varying from 0 to 40 degree. With $E \parallel x$, the transmission spectra split to two modes when the incident angle increases up to 10 degree. The different behaviors with different orientations are due to coupling between the DLSP resonance of top layer particles and the SP, LSP resonances of hole array at the bottom layer. With $E \parallel y$, the resonance is mainly due to coupling between the DLSP resonance of particles and the LSP resonance of the hole array, which manifests the angle-independent behavior. With $E \parallel x$, however, the coupling between SP and DLSP resonances are contribute to the resonance, and the resonance splits into two modes.
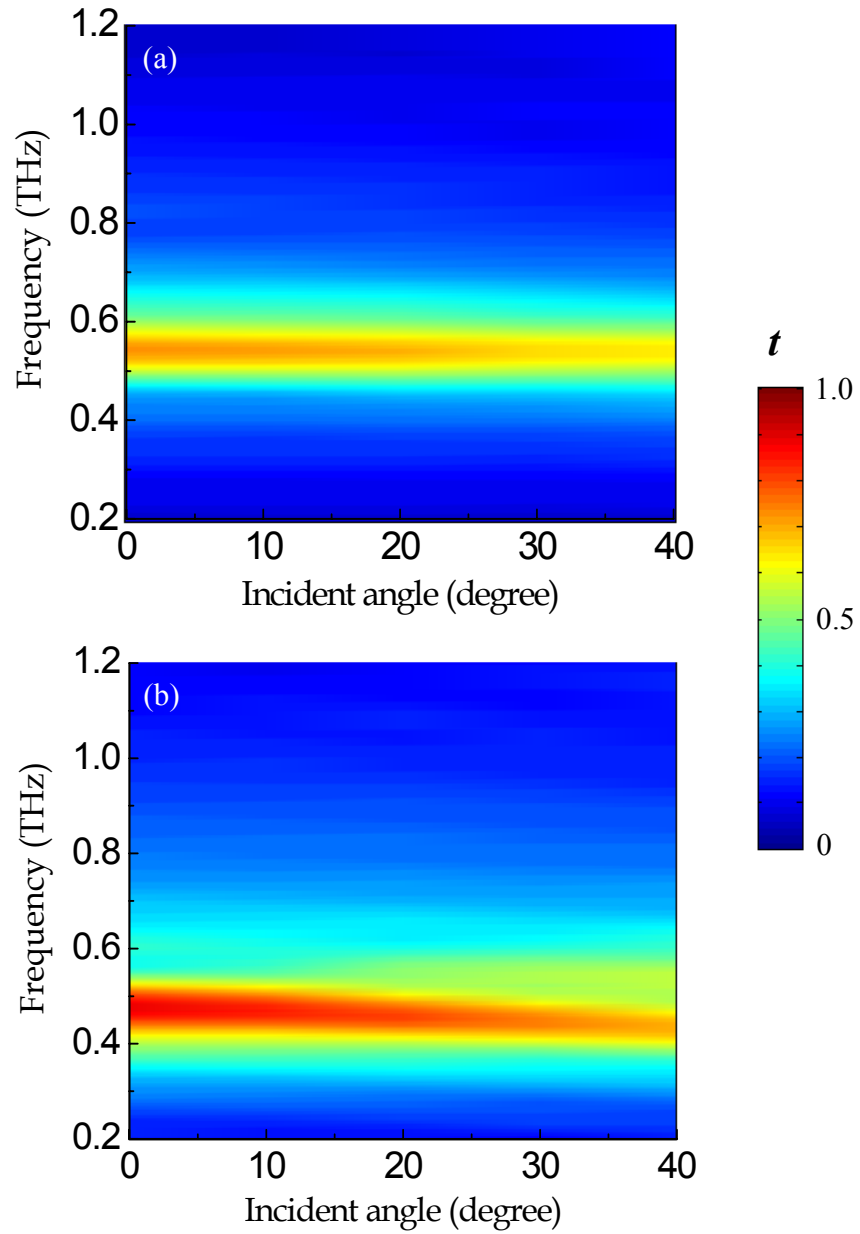
Figure 5-3 Measured angle-resolved transmission with TM polarization incidence for complementary structure with hole and Aluminum particle separated by dielectric particle array, the hole and particle dimension is $100 \times 80 \ \mu m^2$, periodicity is $160 \ \mu m$, (a) $E \parallel y$, (b) $E \parallel x$.

In Figure 5-4, when the incidence wave switches to TE polarization, with $E \parallel x$, the resonance is located at 0.54 THz, and shifts to 0.48 THz with $E \parallel y$. Both of the orientations possess angle-independent transmission spectra. As mentioned in Chapter 2.5.5, with TE polarization incidence, the incident angle will not influence the resonance frequency of the SP [±1,0] mode, because the wave vector has no projection on the direction of SP propagating. When the SP [±1,0] mode couples with the DLSP resonance of particles, the resonance exhibits angle-independent behavior.
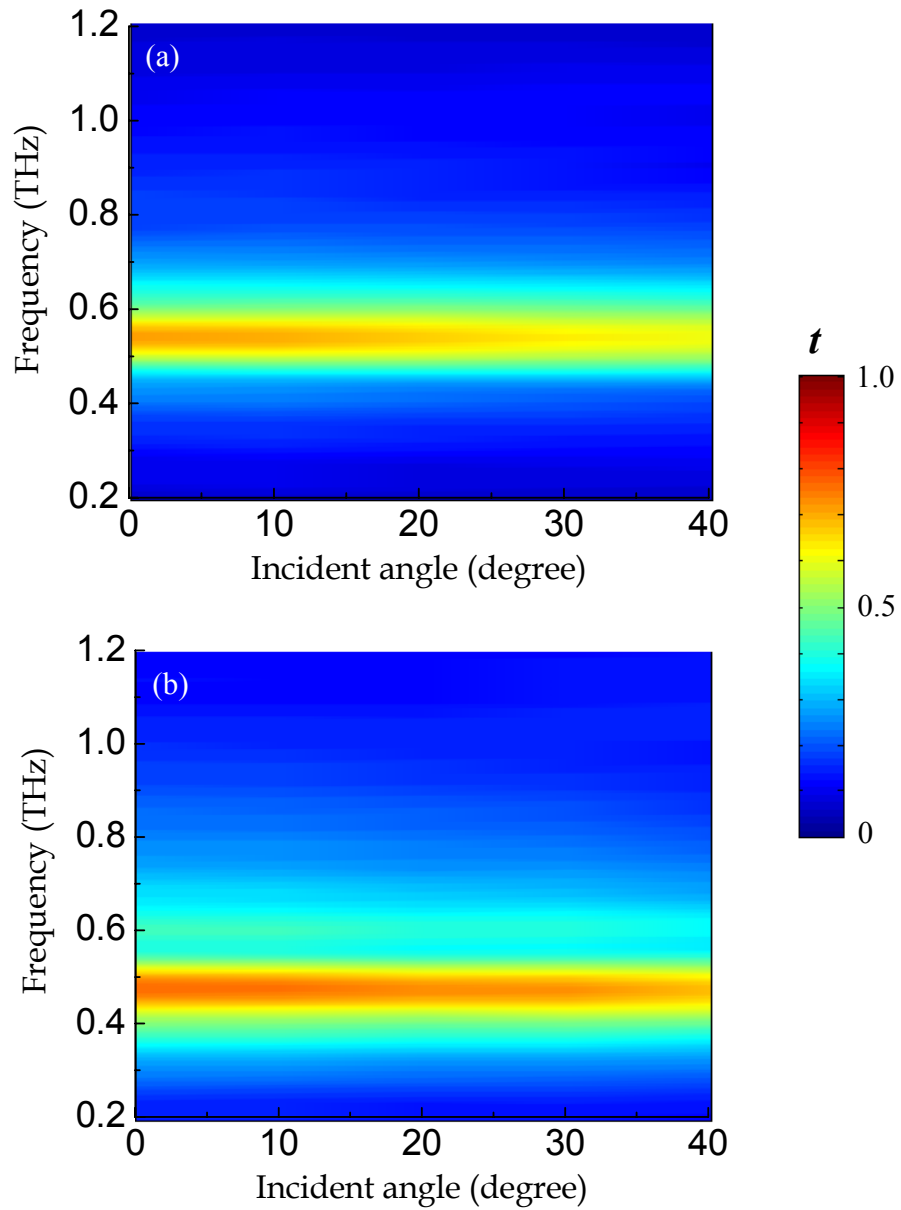
Figure 5-4 Measured angle-resolved transmission with TE polarization for complementary array with hole at bottom layer and Aluminum particle on top layer separated by dielectric particle, the hole and particle dimension is $100 \times 80 \ \mu m^2$, periodicity is 160 μm, (a) $E \parallel y$, (b) $E \parallel x$.

5.4 Coupling coefficient

In order to understand the coupling mechanism between the DLSP resonance of particles and the SP, LSP resonances of the hole array, the coupled problem can be defined as Hamiltonian [38], $\hat{H} = \hat{H}_1 + \hat{H}_2 + \hat{H}_3 + \hat{V}$, as mentioned in Chapter 4.1.5. The eigenstate of $\hat{H}_1$ corresponds to the resonant state in DLSPs of the particles on the top layer, $\hat{H}_2$ is the state in Al-Si SP $[\pm 1,0]$ mode of the hole array at the bottom layer, $\hat{H}_3$ is the LSPs of the holes including the direct scattering. The three channels are coupled via the coupling term $\hat{V}$. The effective eigenmode matrix can be written as

$$\begin{pmatrix} \omega_a & 0 & 0 \\ 0 & \omega_b & 0 \\ 0 & 0 & \omega_c \end{pmatrix} = diag \begin{pmatrix} \omega_1 & \kappa_{12} & \kappa_{13} \\ \kappa^*_{12} & \omega_2 & \kappa_{23} \\ \kappa^*_{13} & \kappa^*_{23} & \omega_3 \end{pmatrix} \qquad (5\text{-}1)$$

where $\omega_{a,b,c}$ are the resonant states of complementary structures, $\omega_1/2\pi$ is the DLSPs mode, which can be calculated by $\omega_1/2\pi = (c/2L)\varepsilon_d^{-1/2}$, where L is the length of the particle parallel to the polarization of the incident electric field, ε_d is the dielectric constant of the dielectric spacer [15]. $\omega_2/2\pi$ is the SPs mode of hole array, which can be given approximately in terahertz frequency as [38].

$$\sqrt{\left(\frac{(\omega_2/2\pi)\sin\theta}{c} + \frac{m}{P}\right)^2 + \left(\frac{n}{P}\right)^2} = \frac{(\omega_2/2\pi)\varepsilon_d^{1/2}}{c} \qquad (5\text{-}2)$$

where m, n are integer mode indices, P is periodicity, and θ is incident angle. $\omega_3/2\pi$ is the LSPs in the hole as well as the direct scattering, κ_{12}, κ_{13} and κ_{23} are coupling

coefficients among the three resonant states. The variables, i.e. ω_3, κ_{12}, κ_{13}, and κ_{23} are obtained by diagonalizing $\hat{H}$ using the angle-resolved transmission data.

Based on the angle-dependent transmission of the complementary structure the coupling coefficient is calculated. With TM polarization incidence, at $E \parallel y$, the calculated coefficients are $|\kappa_{12}| = 1.5 \times 10^{-3}$, $|\kappa_{13}| = 0.107$, and $|\kappa_{23}| = 4.3 \times 10^{-3}$, indicating that the coupling between DLSPs and LSPs primarily contributes to the field enhancement, which further explains the angel-independent behavior observed in Fig. 5-3 (a). At $E \parallel x$, the calculated coefficients are $|\kappa_{12}| = 0.192$, $|\kappa_{13}| = 7.00 \times 10^{-4}$, and $|\kappa_{23}| = 3 \times 10^{-4}$, manifesting the dominant role of the coupling between DLSPs and SPs, which due to the angle-dependent resonance. With TE polarization, at $E \parallel y$, the calculated coefficients are $|\kappa_{12}| = 0.109$, $|\kappa_{13}| = 0.106$, and $|\kappa_{23}| = 8.48 \times 10^{-2}$. At $E \parallel x$, the calculated coefficients are $|\kappa_{12}| = 0.108$, $|\kappa_{13}| = 0.103$, and $|\kappa_{23}| = 4.5 \times 10^{-2}$. Both of the coefficients manifest the strong coupling between DLSP and LSP as well as DLSP and SPP.

5.5 Electric field simulation

The electric field distribution of the complementary structure under normal wave incidence is simulated, as shown in Figure 5-5. With $E \parallel y$, as shown in Figures 5-5(a), intensified electric field is distributed at the edge of the particle along the direction of E field as a dipole resonance. Different from the DLSP resonance of particles, the electric field of the complementary structure also distributed along the SP propagating direction on metallic surface, indicating that there exit a coupling between the SP resonance of the

hole array and the DLSP resonance of particles. Figure 5-5(b) illustrates the electric field distribution with $E \parallel x$. The DLSP resonance of particles is similar to that of $E \parallel y$ except that stronger SP resonance is presented at the metal surface due to the variation in hole orientation. As a result, stronger coupling between DLSPs and SPs is induced. This is also consistent with the coupling coefficient calculated shown in Chap. 5.1.4, in particular, the electric field along the surface of metal in the vicinity of the complementary structure is enhanced than that of $E \parallel x$.
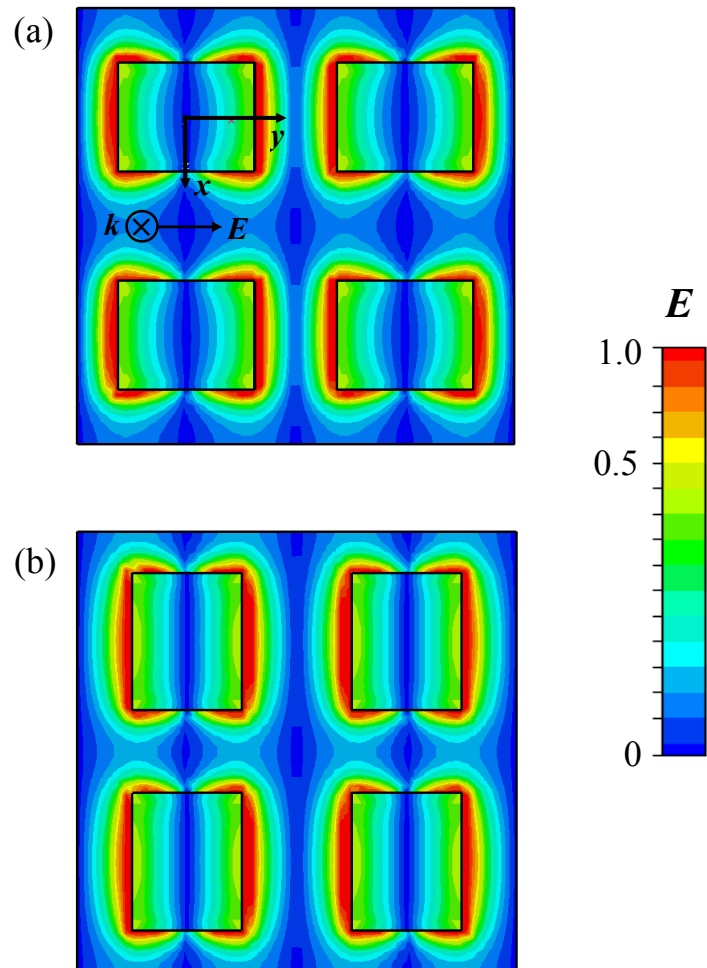
Figure 5-5 Simulated electric field distributions of the complementary array with 100 × 80 μm² hole, 100 × 80 μm² Aluminum particle, as well as 100 × 80 μm² dielectric spacer, periodicity 160 μm, (a) $E \parallel y$, resonant at 0.58 THz, (b) $E \parallel x$, resonant at 0.51 THz.

As introduced in Section 1.1.3, in the visible regime, SPs exhibit large field confinement at the interface and have a small propagation length. In the terahertz regime, however, SPs reveals small localization and larger propagation length which is not fitted to the waveguide application. With the hole array patterned on metal surface, the artificial plasmons along the interface result in better confinement of surface waves in the terahertz regime. Figure 5-6 exhibits the simulated electric field distribution at the cross section cutting along the y axis of the complementary and hole-only array, respectively. The localization of electric field at the metal surface of the hole-only array is several orders of magnitude higher than that of the complementary array. It is not easy to measure the localization of electric field, but we have the evidence from the simulation to believe that the complementary structure can improve the electric field localization, which can be applied in waveguide and communications.
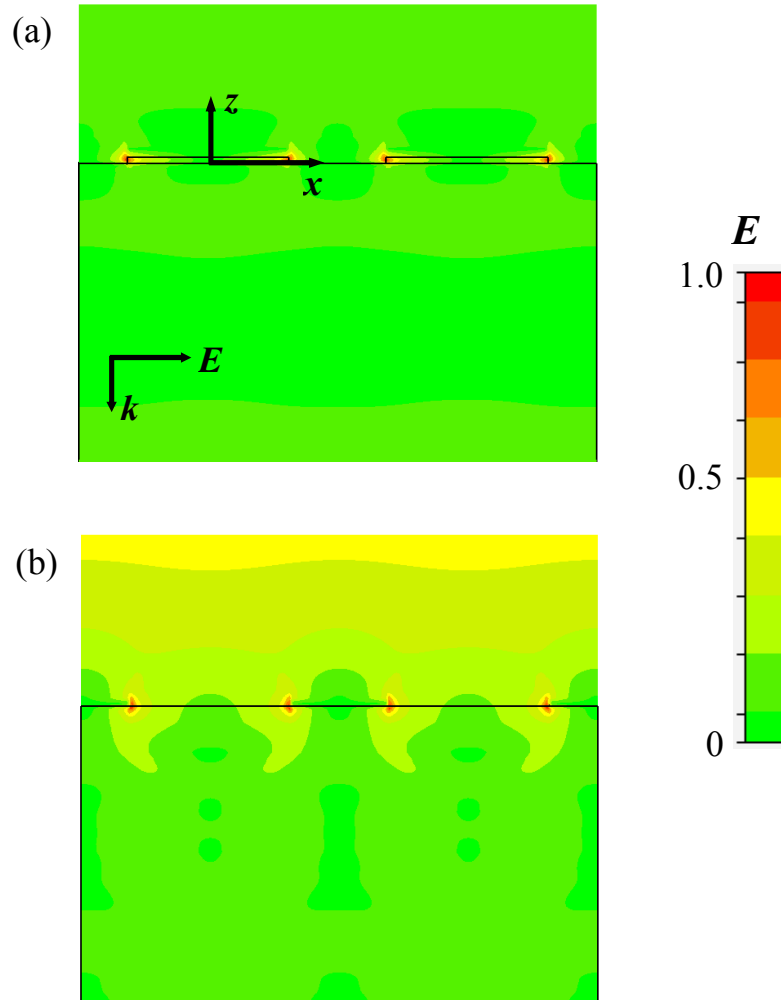
Figure 5-6 Simulated electric field distributions at the cross section cutting along y axis of the complementary array with 100×80 μm^2 holes, 100×80 μm^2 Aluminum particles, as well as a 100×80 μm^2 dielectric spacer, periodicity 160 μm, and the corresponding hole-only array (a) complementary array resonanting at 0.58 THz, (b) hole-only array resonanting at 0.51 THz,

5.6 Conclusion

Enhanced transmission through multilayer complementary structures is investigated. By measuring the angle-resolved spectra, the coupling mechanism showing the interaction between resonance of particles and holes is manifested. Although the direct scattering is very low, the enhanced transmission is due to the out-plane coupling between DLSP resonance of particles on top layer and the resonance of SPs and LSPs of the holes at the bottom layer. Meanwhile, the numerical simulation shows good agreement with the measurements. The resonance of the multilayer structures is promising in biomedical sensing.

CHAPTER VI

CONCLUSION

In conclusion, the resonant properties of subwavelength plasmonic structures are investigated in the terahertz regime. The coupling between SPs and LSPs is proven to contribute substantially to the enhanced transmission in the subwavelength hole array. The DLSPs are demonstrated to induce the resonance in the metallic particle array. Also, the enhanced transmission through the rectangular coaxial array is investigated experimentally and theoretically, which is originated from the coupling between SPs, LSPs and DLSPs. The resonance of multilayer complementary structure is explored, which is due to the out-plane couling between SPs, LSPs and DLSPs. At last, the plasmonic cavity with nearly perfect absorption is investigated as the resonance of F-P cavity.

We present THz-TDS studies of transmission properties of random and periodic subwavelength hole arrays. Even in subwavelength random hole array, extraordinary transmission can be observed through the coupling between LSPs and direct transmission. The polarization and angle-dependent transmission through the periodic hole array reveal the physical origin of the enhanced transmission, i.e. the coupling between SPs, LSPs and direct scattering. The theoretical analysis by the Fano model,

coupling coefficient calculation, electric field simulation provides a good agreement with the experimental results.

Also, terahertz properties of periodic arrays of subwavelength metallic particles are investigated. The factors, such as particles shape, surrounding substrate, and periodicity are found to influence the resonance of DLSPs. The ring particle resonance, which provides larger electromagnetic field enhancement and improved tunability, is analyzed by varying the width of the ring wall. The plasmon hybridization theory is employed to explain the resonance behavior of the coaxial particle arrays. The electric field of different particle shapes is modeled by CST Microwave Studio simulations in order to reveal the insight of resonant properties of DLSPs.

Improved transmission enhancement in the rectangular coaxial array is observed in the THz-TDS measurement when compared with the hole-only array. By changing the dimension of solid particles or ring particles, it is indicated that both DLSPs of the particles, SPs and LSPs of the holes influence the resonance of the coaxial structures. The coupling between SPs, LSPs, and DLSPs is demonstrated to introduce the enhanced transmission by using the Fano model fitting, coupling coefficient calculation, and electric field distribution simulation.

At last, the multilayer complementary structure is investigated by measurement and numerical simulation. The enhanced transmission is due to the out-plane coupling between DLSP resonance of particle on top layer and the resonance of SP and LSP of the

holes at the bottom layer. Such multilayer complementary structures can be potentially applied in terahertz sensing, and spectroscopy.

The extraordinary enhanced transmission of hybridized structures due to either in-plane or out-of-plane coupling between SPs, LSPs and DLSPs demonstrated in this dissertation provides an improvement to the sensors and frequency selective filters by having narrower linewidth and larger frequency tunability. Such plasmonic structures can have further explored by optimizing the structures and stacking more layers to strengthen the coupling resonance.

REFERENCES

1. H. A. Bethe, "*Theory of Diffraction by Small Holes*", Phys. Rev. **66**, 163 (1944).

2. T. W. Ebbesen, H. J. Lezec, H. F. Ghaemi, T. Thio, and P. A. Wolff, "*Extraordinary optical transmission through sub-wavelength hole arrays*", Nature 391, 667 (1998).

3. M. Lahav, A. Vaskevich, and I. Rubinstein, "*Biological Sensing Using Transmission Surface Plasmon Resonance Spectroscopy*", Langmuir 20, 7365 (2004).

4. M. Specht, J. D. Pedarnig, W. M. Heckl, and T. W. Hänsch, "*Scanning plasmon near-field microscope*". Phys. Rev. Lett. 68, 476. (1992).

5. W. L. Barnes, A. Dereux and T. W. Ebbesen, "*Surface plasmon subwavelength optics*", Nature 424, 6950 (2003).

6. K. R. Catchpole and A. Polman, "*Plasmonic solar cells*", Opt. Express 16, 26 (2008).

7. Y. Wang, "*Voltage-induced color-selective absorption with surface plasmons*", Appl. Phys. Lett. 67, 19 (1995).

8. S. Enoch, R. Quidant, and G. Badenes, "*Optical sensing based on plasmon coupling in nanoparticle arrays*", Opt. Express 12, 3422 (2004).

9. C. G. Blatchford, J. R. Campbell, and J. A. Creighton, "*Plasma resonance -- enhanced raman scattering by absorbates on gold colloids: The effects of aggregation*", Surface Science 120, 435 (1982).

153

10. D. Qu, D. Grischkowsky, and W. Zhang, "*Terahertz transmission properties of thin, subwavelength metallic holearrays*", Opt. Lett. 29, 896 (2004).

11. A. K. Azad and W. Zhang, "*Resonant terahertz transmission in subwavelength metallic hole arrays of sub-skin-depth thickness*", Opt. Lett. **30**, 2945 (2005).

12. A. K. Azad, Y. Zhao, and W. Zhang, "*Transmission properties of terahertz pulses through an ultrathin subwavelength silicon hole array*", Appl. Phys. Lett. 86, 141102 (2005).

13. J. Han, A. K. Azad, Mufei Gong, X. Lu and W. Zhang, "*Coupling between surface plasmons and nonresonant transmission in subwavelength holes at terahertz frequencies*", Appl. Phys. Lett. 91, 071122 (2007).

14. X. Lu, J. Han, and W. Zhang, "*Resonant terahertz reflection of periodic arrays of subwavelength metallic rectangles*", Appl. Phys. Lett. 92, 121103 (2008).

15. N. C. J. van der Valk and P. C. M. Planken, "*Electro-optic detection of subwavelength terahertz spot sizes in the near field of a metal tip*", Appl. Phys. Lett. 81, 1558 (2002).

16. F. Miyamaru, S. Hayashi, C. Otani, K. Kawase, Y. Ogawa, H. Yoshida, and E. Kato, "*Terahertz surface-wave resonant sensor with a metal hole array*", Opt. Lett. 31, 1118 (2006).

17. S. A. Maier, *Plasmonics: Fundamentals and applications* (Springer, 1998).

18. R. H. Ritchie, "*Plasma Losses by Fast Electrons in Thin Films*", Phys. Rev. 106, 874 (1957).

19. H. Raether, *Surface plasmons on smooth and rough surfaces and on gratings* (Springer-Verlag, Berlin, 1998).

20. G. Goubau, "*Surface Waves and Their Application to Transmission Lines*", J. Appl. Phys. 21, 1119 (1950).

21. H. Liu and P. Lalanne, "*Microscopic theory of the extraordinary optical transmission*", Nature 452, 728 (2008).

22. W. L. Barnes, W. A. Murray, J. Dintinger, E.Devaux, and T. W. Ebbesen, "*Surface Plasmon Polaritons and Their Role in the Enhanced Transmission of Light through Periodic Arrays of Subwavelength Holes in a Metal Film*", Phys. Rev. Lett. 92, 107401 (2004).

23. C. R. Williams, S. R. Andrews, S. A. Maier, A. I. Fernandez-Dominguez, L. Martin Moreno, and F. J. Garcia-Vidal, "*Highly confined guiding of terahertz surface plasmon polaritons on structured metal surfaces*", Nat. Photon. 2, 175 (2008).

24. H. C. van de Hulst, *Light scattering by small particles* (Dover, New York, 1981).

25. R. J. Mailloux, "*Phased array theory and technology*", Proceedings of the IEEE 70, 246 (1982).

26. K. L. van der Molen, K. J. Klein Koerkamp, S. Enoch, F. B. Segerink, N. F. Van Hulst, and L. Kuipers, "*Role of shape and localized resonances in extraordinary transmission through periodic arrays of subwavelength holes: Experiment and theory*", Phys. Rev. B 72, 045421 (2005).

27. Zhichao Ruan and Min Qiu, "*Enhanced Transmission through Periodic Arrays of Subwavelength Holes: The Role of Localized Waveguide Resonances*", Phys. Rev. Lett. 96, 233901 (2006).

28. F. J. García-Vidal, E. Moreno, J. A. Porto, and L. Martín-Moreno, "*Transmission of Light through a Single Rectangular Hole*", Phys. Rev. Lett. 95, 103901 (2005).

29. J. W. Lee, M. A. Seo, D. H. Kang, K. S. Khim, S.C. Jeoung, and D. S. Kim, "*Terahertz Electromagnetic Wave Transmission through Random Arrays of Single Rectangular Holes and Slits in Thin Metallic Sheets*", Phys. Rev. Lett. 99, 137401 (2007).

30. A. Degiron, H. J. Lezec, N. Yamamoto, and T. W. Ebbesen, "*Optical transmission properties of a single subwavelength hole in a real metal*", Opt. Commun. 239, 61 (2004).

31. A. Roberts, "*Electromagnetic theory of diffraction by a circular hole in a thick, perfectly conducting screen*", J. Opt. Soc. Am. A 4, 1970 (1987).

32. J. Parsons, E. Hendry, C. P. Burrows, B. Auguie, J. R. Sambles, and W. L. Barnes, "*Localized surface-plasmon resonances in periodic nondiffracting metallic nanoparticle and nanohole arrays*", Phys. Rev. B 79, 073412 (2009).

33. A. K. Azad, *Resonant terahertz transmission of plasmonic subwavelength hole arrays*, Ph. D. Thesis, May (2006).

34. D. Grischkowsky, S. Keiding, M. Van Exter, and Ch. Fattinger, "*Far-Infrared Time-Domain Spectroscopy with Terahertz Beams of Dielectrics and Semiconductors*", J. Opt. Soc. Am. B 7, 2006 (1990).

35. J. Han, X. Lu, and W. Zhang, "*Terahertz transmission in subwavelength holes of asymmetric metal-dielectric interfaces: The effect of a dielectric layer*", J. Appl. Phys. 103, 033108 (2008)

36. U. Fano, "*Effects of Configuration Interaction on Intensities and Phase Shifts*", Phys. Rev. 124, 1866 (1961).

37. C. Genet, M. P. van Exter, and J. P. Woerdman, "*Fano-type interpretation of red shifts and red tails in hole array transmission spectra*", Opt. Commun. 225, 331 (2003).

38. W. Fan, S. Zhang, B. Minhas, J. M. Kevin, and S. R. J. Brueck, "*Enhanced Infrared Transmission through Subwavelength Coaxial Metallic Arrays*", Phys. Rev. Lett. 94, 033902 (2005).

39. www.cst.com

40. C. L. Haynes, A. D. Mcfarland, L. Zhao, R. P. Van Duyne, G. C. Schatz, L. Gunnarsson, J. Prikulis, B. Kasemo, and M. Käll, "Nanoparticle Optics: The Importance of Radiative Dipole Coupling in Two-Dimensional Nanoparticle Arrays", J. Phys. Chem. B **107**, 7337 (2003).

41. K. B. Crozier, A. Sundaramurthy, G. S. Kino, and C. F. Quate, "*Optical antennas: Resonators for local field enhancement*", J. Appl. Phys. 94, 4632 (2003).

42. J. Aizpurua, G. W. Bryant, L. J. Richter, F. J. García de Abajo, B. K. Kelley, and T. Mallouk, "*Optical properties of coupled metallic nanorods for field-enhanced spectroscopy*", Phys. Rev. B 71, 235420 (2005).

43. N. Laman and D. Grischkowsky, "*Reduced conductivity in the terahertz skin-depth layer of metals*", Appl. Phys. Lett. 90, 122115 (2007).

44. M. Walther, D. G. Cooke, C. Sherstan, M. Hajar, M. R. Freeman, and F. A. Hegmann, "*Terahertz conductivity of thin gold films at the metal-insulator percolation transition*", Phys. Rev. B 76, 125408 (2007).

45. E. A. Parker and S. M. A. Hamdy, "*Rings as elements for frequency selective surfaces*", Electro. Lett. **17**, 612 (1981).

46. B. Lamprecht, G. Schider, R. T. Lechner, H. Ditlbacher, J. R. Krenn, A. Leitner, and F. R. Aussenegg, "*Metal Nanoparticle Gratings: Influence of Dipolar Particle Interaction on the Plasmon Resonance*", Phys. Rev. Lett. 84, 4721 (2000).

47. J. Aizpurua, P. Hanarp, D. S. Sutherland, M. Käll, G. W. Bryant and F. J. García de Abajo, "*Optical Properties of Gold Nanorings*", Phys. Rev. Lett. 90, 057401 (2003).

48. J. Kyung-Young, F. L. Teixeira, and R. M. Reano, "*Au/SiO$_2$ Nanoring Plasmon Waveguides at Optical Communication Band*", J. Lightwave Tech. 25, 2757 (2007).

49. Z. Hao, M. C. Martin, B. Harteneck, S. Cabrini, and E. H. Anderson, "*Negative index of refraction observed in a single layer of closed ring magnetic dipole resonators*", Appl. Phys. Lett. 91, 253119 (2007).

50. X. Lu, and W. Zhang, "*Terahertz localized plasmonic properties of subwavelength ring and coaxial structures*", Appl. Phys. Lett. 94, 181106 (2009).

51. C. Dahmen and G. von Plessen, "*Optical Effects of Metallic Nanoparticles*", Aust. J. Chem. 60, 447 (2007).

52. A. Wokaun, J. P. Gordon, and P. F. Liao, "*Radiation Damping in Surface-Enhanced Raman Scattering*", Phys. Rev. Lett. 48, 957 (1982).

53. E. Prodan, C. Radloff, N. J. Halas, and P. Nordlander, "*A Hybridization Model for the Plasmon Response of Complex Nanostructures*", Science 302, 419 (2003).

54. T. A. Albright, J. K. Burdett, and M. H. Whangbo, *Orbital interactions in chemistry*, (John Wiley & Sons, 1985).

55. F. Hao, P. Nordlander, M. T. Burnett, and S. A. Maier, "*Enhanced tunability and linewidth sharpening of plasmon resonances in hybridized metallic ring/disk nanocavities*", Phys. Rev. B 76, 245417 (2007).

56. H. J. Lezec, A. Degiron, E. Devaux, R. A. Linke, L. Martín-Moreno, F. J. García-Vidal, and T. W. Ebbesen, "*Beaming Light from a Subwavelength Hole*", Science 297, 820 (2002).

57. A. Alu, F. Bilotti, E. Nader, and L. Vegni, "*Metamaterial covers over a small hole*", IEEE Trans. Antenn. Propag. 54, 1632 (2006).

58. K. Aydin, A. O. Cakmak, L. Sahin, Z. Li, F. Bilotti, L. Vegni, and E. Ozbay, "*Split-Ring-Resonator-Coupled Enhanced Transmission through a Single Subwavelength Hole*", Phys. Rev. Lett. 102, 013904 (2009).

59. A. Moreau, G. Granet, F. Baida, and D. Van Labeke, "*Light transmission by subwavelength square coaxial hole arrays in metallic films*", Opt. Express 11, 1131 (2003).

60. W. Jia and X. Liu, "*Mechanism of the superenhanced light transmission through 2D subwavelength coaxial hole arrays*", Phys. Lett. A 344, 451 (2005).

61. Y. Poujet, J. Salvi, and F.I. Baida, "*90% extraordinary optical transmission in the visible range through annular hole metallic arrays*", Opt. Lett. 32 , 2942 (2007).

62. S. M. Orbons, M. I. Haftel, C. Schlockermann, D. Freeman, M. Milicevic, T. J. Davis, B. Luther-Davies, D. N. Jamieson, and A. Roberts, "*Dual resonance*

mechanisms facilitating enhanced optical transmission in coaxial waveguide arrays", Opt. Lett. 33, 821 (2008).

63. S. Wu, Q. Wang, X. Yin, J. Li, D. Zhu, S. Liu, and Y. Zhu, *"Enhanced optical transmission: Role of the localized surface plasmon"*, Appl. Phys. Lett. 93, 101113 (2008).

64. A. A. Yanik, X. Wang, S. Erramilli, M. K. Hong, and H. Altug, *"Extraordinary midinfrared transmission of rectangular coaxial nanohole arrays"*, Appl. Phys. Lett. 93, 081104 (2008).

65. M.J. Kofke, D. H. Waldeck, Z.Fakhraai, S. Ip, and G. C. Walker, *"The effect of periodicity on the extraordinary optical transmission of annular hole arrays"*, Appl. Phys. Lett. 94, 023104 (2009).

66. L. Lin, R. J. Reeves and R. J. Blaikie, *"Surface-plasmon-enhanced light transmission through planar metallic films"*, Phys. Rev. B 74, 15 (2006).

67. A. Ghoshal, I. Divliansky and P. G. Kik, *"Experimental observation of mode-selective anticrossing in surface-plasmon-coupled metal nanoparticle arrays"*, Appl. Phys. Lett. 94, 17 (2009).

68. T. Z. A. Christ, S. G. Tikhodeev, N. A. Gippius, O. J. F. Martin, J. Kuhl, and H. Giessen, *"Interaction between localized and delocalized surface plasmon polariton modes in a metallic photonic crystal"*, phys. stat. sol. (b) 243, 10 (2006).

69. M.D. He, L.L. Wang, J.Q. Liu, X. Zhai, Q. Wan, X. Chen and B. S. Zou, *"Controllable light transmission through cascaded metal films perforated with periodic hole arrays"*, Appl. Phys. Lett. 93, 22 (2008).

70. A. Artar, A. A. Yanik and H. Altug, "*Fabry-Pérot nanocavities in multilayered plasmonic crystals for enhanced biosensing*", Appl. Phys. Lett. 95, 5 (2009).

VITA

Xinchao Lu

Candidate for the Degree of

Doctor of Philosophy

Dissertation: STUDIES OF SURFACE PLASMONS AND LOCALIZED SURFACE
PLASMONS AT TERAHERTZ FREQUENCIES

Major Field: Electrical Enginnering

Biographical:

Education:

Received the Bachelor of Science degree in Optoelectronics from
Tianjin University, China, in July 2000; and received Master of Science
degree in Physics electronics from Tianjin University, China, in
February 2003. Completed the requirements for the Doctor of
Philosophy of Science degree in Electrical Engineering at Oklahoma
State University, Stillwater, Oklahoma, in December, 2009.

Experience:

Employed by Chinese Electronic-Technology Eleventh Research
Institute, China, as an Engineer, 2003 to 2006; employed by Oklahoma
State University, Department of Electrical Engineering as a teaching and
research assistant, 2006 to present.

Name: Xinchao Lu   Date of Degree: December, 2009

Institution: Oklahoma State University   Location: Stillwater, Oklahoma

Title of Study: STUDIES OF SURFACE PLASMONS AND LOCALIZED SURFACE
        PLASMONS AT TERAHERTZ FREQUENCIES

Pages in Study: 161   Candidate for the Degree of Doctor of Philosophy

Major Field: Electrical Engineering

Scope and Method of Study: The goal of this study is to investigate the physical
        mechanism of field enhancement in plasmonic subwavelength structures in the
        terahertz regime. Such plasmonic structures were fabricated by using
        microelectronic lithography technique. By using terahertz time-domain
        spectroscopy, the transmission or reflection properties of the plasmonic structures
        were systematically investigated. Numerical simulations were carried out to
        further verify the experimental studies.

Findings and Conclusions: We demonstrated that the resonance enhancement through
        subwavelength plasmonic structures at terahertz frequencies is due to either
        surface plasmons excited along the interface of dielectric and metal or dipolar
        localized surface plasmons introduced by dipole oscillation of metallic particles.
        Compared to subwavelength hole structures, the coaxial and multilayer
        complementary structures can approach even higher enhanced transmission,
        which is due to the coupling between dipole localized surface plasmon of the
        particles, surface plamons and localized surface plasmons of the holes. Such
        plasmonic crystals can be potentially applied in sensors, frequency selective
        elements, and near-field spectroscopy.

ADVISER'S APPROVAL: Weili Zhang